UNIVERSITÀ DEGLI STUDI DI PADOVA

Dipartimento di Scienze del Farmaco

SCUOLA DI DOTTORATO DI RICERCA IN SCIENZE MOLECOLARI

INDIRIZZO SCIENZE FARMACEUTICHE

CICLO XXVIII

MODIFICA DELLE PROPRIETA' SUPERFICIALI DI NANOPARTICELLE D'ORO PER IL TRATTAMENTO MULTIMODALE AL TUMORE

Direttore della Scuola: Chiar.mo Prof. Antonino Polimeno

Coordinatore d'indirizzo: Chiar.mo Prof. Alessandro Dolmella

Supervisore: Chiar.mo Prof. Stefano Salmaso

Dottoranda: Chiara Brazzale

UNIVERSITÀ
DEGLI STUDI
DI PADOVA

UNIVERSITY OF PADOVA

Department of Pharmaceutical and Pharmacological Sciences

DOCTORAL SCHOOL IN MOLECULAR SCIENCES

PHARMACEUTICAL SCIENCES CURRICULUM

XXVIII CYCLE

GOLD NANOPARTICLE SURFACE TUNING FOR MULTIMODAL TREATMENT OF CANCER

School Director: Chiar.mo Prof. Antonino Polimeno

Curriculum Coordinator: Chiar.mo Prof. Alessandro Dolmella

Supervisor: Chiar.mo Prof. Stefano Salmaso

PhD student: Chiara Brazzale

“La cosa più bella che possiamo sperimentare è il mistero.
E’ questa la fonte di ogni vera arte e scienza. Colui al quale questa emozione è estranea, che non riesce più a sorprendersi e rimanere in soggezione, è praticamente morto, i suoi occhi sono chiusi”.

"The most beautiful thing we can experience is the mysterious. It is the source of all true art and all science. He to whom this emotion is a stranger, who can no longer pause to wonder and stand rapt in awe, is as good as dead: his eyes are closed."

Albert Einstein

TABLE OF CONTENTS

1. ABBREVIATIONS

AIBN	Azobisisobutyronitrile
BCA	Bicinchoninic acid
$CDCl_3$	Deuterated chloroform
CO_2	Carbon dioxide
DCC	Dicyclohexylcarbodiimide
DCM	Dichloromethane
DCU	Dicyclohexylurea
DDS	Drug delivery system
DLS	Dynamic Light Scattering
DMAP	4-Dimethylaminopyridine
DMF	Dimethylformamide
DMSO	Dimethyl sulfoxide
DP	Degree of Polymerization
DTNB	5,5'-dithiobis-(2-nitrobenzoic acid)
EDTA	Ethylenediaminetetraacetic acid
EPR	Enhanced permeability and retention
Et_2O	Diethyl ether
EtOAc	Ethyl acetate
FBS	Fetal Bovine Serum
FFDMEM	Folic free Dulbecco's Modified Eagle Medium
FR	Folate Receptor
GMA	Glycerol Methacrylate
GNPs	Gold nanoparticles
GPC	Gel permeation chromatography
$HAuCl_4$	Tetrachloroauric (III) acid
HCl	Hydrochloric acid
HNO_3	Nitric acid
HPMA	N-(2-Hydroxypropyl) methacrylamide
H_2SO_4	Sulfuric acid

KB cells	Human cervical carcinoma cell line
KCl	Potassium chloride
macro CTA	Macro Transfer Agent
MCF-7 cells	Human breast adenocarcinoma cell line
MCH	(methacryloyloxy)ethyl-3-chloro-4-hydroxybenzoate
MeOH	Methanol
$MgCl_2$	Magnesium chloride
$MgSO_4$	Magnesium sulfate
MTT	3-(4,5-dimethylthiazol-2-yl)-2,5-diphenyltetrazolium bromide
MW	Molecular Weight
MWCO	Molecular weight cut-off
N_2	Nitrogen
NaOH	Sodium hydroxide
NaCl	Sodium Chloride
NHS	N-Hydroxysuccinimide
NIR	Near infrared
PBS	Phosphate Saline Buffer
PDI	Polydispersity Index
PEG	Polyethylene glycol
pKa	Acid dissociation constant
PLGA	Poly(lactic-co-glycolic acid)
RAFT	Reversible addition fragmentation chain transfer polymerization
RES	Reticuloendothelial System
ROS	Reactive oxygen species
RP-HPLC	Reverse Phase High Pressure Liquid Chromatography
SPR	Surface Plasmon resonance
TAC	Computer assisted tomography
TEA	Triethylamine
TFA	Trifluoroacetic acid
TEM	Transmission electron microscopy
THF	Tetrahydrofuran

TLC	Thin Layer Chromatography
UV	Ultraviolet
Vis	Visible
VEGF	Vascular endothelial growth factor

2. RIASSUNTO

Il presente progetto di ricerca prevede lo studio e lo sviluppo di sistemi nanoparticellari intelligenti per uso farmaceutico e terapeutico, capaci di rispondere in modo adeguato a variazioni fisiopatologiche al fine di migliorare l'efficienza del direzionamento selettivo e di ridurre la distribuzione aspecifica nei tessuti sani minimizzando così gli effetti collaterali e abbassando la dose efficace.

Numerosi studi riportati in letteratura hanno sottolineato come determinate patologie siano associate a peculiari condizioni micro-ambientali a livello dei tessuti. In particolare i tessuti tumorali sono in genere caratterizzati da un corredo enzimatico amplificato, un'alterazione del potenziale ossido-riduttivo, un incremento della temperatura tissutale, un abbassamento del pH e alterazioni morfo-funzionali a carico della vascolarizzazione e del sistema linfatico.

Sulla base di tali variazioni è stato possibile disegnare un sistema intelligente in grado di rispondere con alterazioni fisico-morfologiche alle mutate caratteristiche ambientali tipiche dei tessuti tumorali. Tra i vari sistemi colloidali di dimensione nanometrica disponibili in ambito farmaceutico, nanoparticelle d'oro (GNPs) sono state selezionate come carrier in virtù dei numerosi vantaggi quali l'elevata biocompatibilità, semplice chimica di modifica superficiale, elevato rapporto superficie/massa atto a permettere un'ampia funzionalizzazione e dimensioni adeguate per by-passare le barriere fisiologiche e raggiungere quantitativamente il sito d'azione sfruttando l'effetto EPR. Nanoparticelle d'oro sono state sintetizzate secondo la procedura riportata da Turkevich mediante riduzione di acido cloroaurico da parte di sodio citrato, ottenendo particelle dal diametro medio di 15 nm e contenuta polidispersività. La decorazione superficiale di particelle d'oro con un agente di targeting (Folato-PEG) ha inoltre permesso di sfruttare un direzionamento attivo del sistema e di traghettare selettivamente il farmaco a cellule tumorali sovraesprimenti il recettore per l'acido folico. In particolare, uno degli scopi del progetto è stato quello di valutare se vi fosse un'influenza della densità dell'agente direzionante nel determinare l'efficienza d'internalizzazione del sistema. A tal proposito sono stati compiuti studi approfonditi per valutare quale fosse la densità ottimale di Folato-PEG in grado di garantire la massima internalizzazione del nanocarrier. Nanoparticelle d'oro decorate con quantità crescenti di acido folico sono

state testate sulla linea di cellule tumorali KB, sovraesprimente il recettore per il folato. Dagli studi è emerso come 50 catene di Folato-PEG per particella garantiscano la massima efficienza di uptake. Inoltre la presenza di acido folico libero nel terreno di coltura ha inibito la penetrazione delle GNPs confermando come il meccanismo di uptake sia effettivamente mediato dall'agente di targeting Folato-PEG. Ulteriore prova della specificità di internalizzazione è stata fornita incubando GNPs decorate con Folato-PEG con la linea cellulare MCF-7, non esprimente il recettore per il folato. Cellule MCF-7 hanno infatti dimostrato l'uptake di un numero trascurabile di GNPs.
Studi in letteratura evidenziano inoltre come sistemi multi-direzionati possano subire diversi meccanismi d'internalizzazione rispetto a ligandi monovalenti. Al fine di valutare il delivery lisosomiale di nanoparticelle multi-direzionate e confrontarlo con quello del ligando Folato, nanoparticelle d'oro modificate con diverse densità di Folato-PEG (50 e 10 catene per particella) sono state marcate con Rodamina in modo da consentire studi di trafficking intracellulare mediante microscopia confocale. Allo stesso modo, acido folico è stato marcato con Rodamina utilizzando cadaverina come spacer. Dall'analisi quantitativa delle immagini di microscopia confocale si nota come particelle con elevata densità di Folato-PEG (50 catene/particella) raggiungano i compartimenti lisosomiali più rapidamente e in quantità significativamente superiore rispetto a particelle con bassa densità di Folato-PEG (10 catene/particella), che hanno invece dimostrato un profilo di uptake comparabile a quello del monoconiugato Folato-Cadaverina-Rodamina. Si ritiene che un meccanismo di clustering recettoriale indotto dalla presenza di particelle multivalenti possa essere responsabile di un tale effetto. Infatti, in linea con molti studi presenti in letteratura, sistemi multi-direzionati aumentano l'affinità per il binding recettoriale. In seguito sono stati compiuti studi di inibizione del meccanismo di internalizzazione al fine di chiarire quale processo di endocitosi fosse coinvolto. Tali studi hanno evidenziato come GNPs decorate con Folato-PEG, come anche il coniugato Folato-Cadaverina-Rodamina vengano internalizzati mediante endocitosi clatrina-indipendente. Questo risultato è in accordo con quanto emerso dalle immagini di microscopia elettronica di cellule KB incubate con GNPs funzionalizzate con Folato-PEG. Dalle immagini TEM è infatti possibile notare la presenza di invaginazioni della membrane plasmatica dalla forma e dimensioni compatibili con quelle che caratterizzano le caveole. L'endocitosi caveole-mediata è uno dei meccanismi clatrina-indipendente.

Nanoparticelle d'oro presentano inoltre proprietà chimico-fisiche uniche, fortemente dipendenti da dimensione e forma, correlate ad una serie di altre capacità "multifunzionali" che forniscono l'opportunità di combinare diagnostica con un trattamento terapeutico (farmacologico o fisico) mirato. Un ulteriore sviluppo del progetto ha perciò riguardato lo sfruttamento di GNPs direzionate come sensibilizzanti della terapia sonodinamica che prevede l'utilizzo di ultrasuoni per causare la morte cellulare. Dai risultati degli studi cellulari si nota come il trattamento con ultrasuoni in seguito all'internalizzazione di GNPs direzionate determini una consistente morte cellulare. Al contrario, nessun effetto citotossico è stato rilevato dal solo trattamento con ultrasuoni o nanoparticelle. Il test di competizione ha inoltre ribadito la selettività dell'uptake recettore-mediato.

Il concetto di targeting multi-modale è stato successivamente ampliato per lo sviluppo di nanoparticelle d'oro pH responsive, utilizzando un polimero responsivo agli stimoli micro-ambientali, in grado di mascherare le unità direzionanti nel torrente sanguigno ed esporle a livello tumorale. In particolare, è stato sintetizzato il copolimero pH sensibile poli(MCH-co-GMA) mediante tecnica di polimerizzazione RAFT. In condizioni fisiologiche il polimero si trova nella conformazione estesa, esercitando un'azione schermante nei confronti dell'agente di targeting; al contrario nel tessuto tumorale, grazie all'alterazione del pH rispetto al tessuto sano, si verifica il collasso della struttura con acquisizione di una conformazione idrofobica globulare. Ciò determina l'esposizione del direzionante, promuovendo l'endocitosi cellulare.

Particelle d'oro sono state decorate con Folato-PEG (50 catene/particella, densità in grado di garantire una buona internalizzazione, come stabilito dagli studi descritti in precedenza), saturando poi la superficie con il copolimero poli(MCH-co-GMA). Test di uptake sulla linea cellulare KB, eseguiti in terreno privo di acido folico a pH 7.4 e 6.5, hanno evidenziato l'effettiva possibilità di ottenere un targeting selettivo determinato da variazioni microambientali di pH. L'internalizzazione del nanocarrier è stata quantificata sia mediante analisi di spettroscopia atomica che citofluorimetria, confermando come a pH fisiologico il polimero si trovi in conformazione estesa mascherante l'agente direzionante. A pH 6.5, caratteristico dell'interstizio tumorale, si verifica il collasso del polimero, l'esposizione del ligando che viene riconosciuto dallo specifico recettore che ne media l'endocitosi.

Un successivo sviluppo del sistema prevede la funzionalizzazione superficiale delle nanoparticelle con un polimero dotato di gruppi idrazinici a cui coniugare Doxorubicina mediante legame idrazonico. In virtù della sensibilità al pH del legame idrazonico, la Doxorubicina sarà rilasciata esclusivamente nei comparti endosomiali/lisosomiali, in seguito all'uptake cellulare mediato dal recettore FR per l'acido folico.

3. ABSTRACT

The present research project was aimed at developing smart nanosystems able to selectively respond with morphological alterations to external physio-pathologic stimuli. These systems are intended for diagnostic or therapeutic applications in anticancer treatment. The responsiveness of these devices is intended to improve the site-selective targeting efficiency and reduce uncontrolled distribution in healthy tissues thus minimizing the severe side effects and the required dose.

Several studies reported in literature highlighted that certain diseases are associated with specific tissue micro-environmental condition such as temperature, pH and redox alterations. Based on these changes it is possible to design smart nanosystems able to selectively respond to physio-pathologic stimuli through physical and morphological alterations. Among the many colloidal systems available for pharmaceutical applications, gold nanoparticles (GNPs) were selected as carriers because of their several advantages, such as the good biocompatibility, ease of synthesis and functionalization, the high surface-to-volume ratio and dimension that allow to take advantage of the EPR effect. Gold nanoparticles were produced following the Turkevich method by reduction of tetrachloroauric acid by sodium citrate. 15 nm gold nanosphere were obtained with a narrow polydispersity. Afterwards, GNP surface was decorated with a targeting molecule (Folate-PEG) to combine an active and a passive targeting aiming to enhance the selective accumulation within the tumour site. Notably, one of the aims of the project was the evaluation of the influence that the targeting agent density on the particle surface could have on the internalization of the system. For this purpose, deep cell studies have been done to assess whether an optimum targeting agent density exists. Gold nanoparticle surface was decorated with increasing Folate-PEG/GNP ratios and then GNPs were incubated with KB overexpressing Folate receptor cell line. As shown by the results, 50 chains of Folate per particle assure the maximum particle internalization. Moreover, the cell competition assay showed the breakdown of the particle internalization due to the presence of free folate which competes with the GNPs for the binding to the receptor, confirming the endocytosis selectively mediated by the Folate receptor. Folate decorated GNPs were tested also with MCF-7 cells,

which are not provided of the Folate receptor, revealing a negligible uptake, further confirmation of the selectivity of the internalization.

As reported by many research studies, multivalent systems can undergo different internalization route with respect to monotargeted ligand. Aiming to further clarify the uptake mechanism and investigate the lysosomal delivery, two representative multivalent particles modified with different degrees of Folate-PEG (50 and 10 chains/GNP) and the monovalent ligand Folate were fluorescently labelled with Rhodamine to allow the particle detection by confocal microscopy. In particular, Folate was conjugate to Rhodamine using Cadaverine as spacer. Quantitative analysis of confocal images showed that high Folate-PEG density particles (50 chains/GNP) traffic faster and more efficiently to lysosomes with respect to the other particle formulation (10 Folate-PEG chains/GNP) and the monoconjugate Folate-Cadaverine-Rhodamine. One of the hypotheses that justify this result is the different ability of the two GNP formulations to induce the Folate receptor clustering and subsequent delivery to lysosomes. A multivalent network may increase the GNP avidity for FRs, in line with numerous studies. Afterwards pathway inhibition assay was performed aiming to elucidate the internalization mechanism. The results showed that Folate targeted GNPs are taken up by clathrin independent pathway, in agreement with the transmission electron microscopy images in which vesicles compatible with the caveolae were detected. Caveolae-mediated endocytosis is one of the clathrin-independent pathways.

Furthermore, gold nanoparticles possess distinct physico-chemical attributes that make them a versatile platform, suitable for the transport of drugs but also of many other functional molecules offering the great opportunity to combine a diagnostic to a specific therapeutic treatment (pharmacological or physical). A further development of the project concerns the exploitation of GNPs as sensitizers in the sonodynamic therapy. This is a non-invasive approach which uses ultrasound to trigger the cell death as direct consequence of ROS production. Sonodynamic cell study highlighted that the combination of the ultrasound exposure and the pre-incubation of cells with Folate targeted particles induced a significant cell death. On the contrary the incubation of cells with either the sole ultrasound or GNPs showed no cytotoxic effect. The competition assay further confirmed the uptake selectively mediate by the Folate receptor.

The concept of multimodal targeting was extended to the development of pH responsive gold nanoparticles, using a responsive polymer able to respond with morphological alterations to environmental pH changes. The pH responsive polymer poly(MCH-co-GMA) was obtained by RAFT polymerization. At physiological pH (blood stream), the copolymer is in the extended and hydrophilic conformation shielding the targeting agent; once reached the tumour compartment it becomes hydrophobic, collapses and exposes the targeting ligand that promote the endocytosis.

Gold nanoparticles have been decorated with Folate-PEG (50 chains/GNP, which guarantee a good internalization as reported above) and then the particle surface was saturated with the pH responsive polymer poly(MCH-co-GMA).

We had clear evidences that the gold nanoparticle cell uptake can be controlled by the environmental pH. Significant increase of the particle uptake was detected by either atomic adsorption spectroscopy or flow cytometry analysis, when KB cells were incubated with pH responsive Folate targeted gold nanoparticles at pH 6.5 mimicking the tumour interstitium with respect to pH 7.4.

The nanosystem is intended for drug delivery to the tumour. For this purpose a third polymer bearing hydrazidic pendant groups will be synthetized. Then, Doxorubicin will be conjugated to the hydrazidic polymer via hydrazone bond, which once reached the endosomal/lysosomal compartments will by hydrolysed, allowing the drug release.

4. INTRODUCTION

During the last few decades, much effort has been dedicated to biopharmaceutical research and great results have been achieved. However, many issues are still to be solved. The development of a new drug molecule is an expensive and time consuming process. Drugs must reach the target site avoiding uncontrolled distribution through the body and so limiting undesired side effects. This selectivity has been shown by very few molecules. The current methods of drug delivery exhibit specific drawbacks that scientists are attempting to address. Even if a drug is very potent, its therapeutic effect might be reduced by low aqueous solubility, unfavorable pharmacokinetics, poor biodistribution, premature drug degradation before reaching the desired target and lack of selectivity for target tissue. For this reason, novel technologies for drug administration and a step change in the drug delivery science are required in the biopharmaceutical area.

Drug Delivery Systems (DDS) are non-conventional systems exploited to realize a controlled and site specific drug release. The traditional drug formulations show much limitation that can be overcome by the use of these delivery systems. Among the several advantages offered by DDSs, there is the improvement of the drug pharmacokinetic profile, the enhancement of therapeutic efficacy, less side effects and a better patient compliance.

In the past decades manipulation of materials has been changing deeply with a focus on nanometric scale processes. This size range became of major interest in many scientific fields, from physics to chemistry to pharmaceutical and biomedical science. Nano-sized materials exhibit unique physico-chemical properties which are significantly different from their conventional bulk counterpart. With novel capacity to compose multifunctional systems, biomedical research started to aim at designing nanocarriers, such as micelles, liposomes, polymersomes, dendrimers, metal nanoparticles etc., which can be employed in treatment of relevant diseases such as cancer, and in the diagnosis field.

Nanoparticles can be assembled according to a bottom-up process with natural components, such as phospholipids or with synthetic polymers[1]. The nanocarriers properties derive from the functional component features and the assembling

strategies. Aiming to an in vivo administration of these drug vehicles, nanocarriers must exhibit defined characteristics, and many parameters have to be taken in account: size, shape, surface charge, hydrophilic/hydrophobic balance, biocompatibility, complement activation, bioelimination, drug release profile etc. Drug delivery nanovehicles protect the drug from the external environment and possess adequate size to extravasate through the fenestrae of cancer capillaries, while being too bulky to be subject to kidney glomerular filtration. This results in long circulation time and enhanced accumulation within the tumour. Furthermore, their prolonged lifetime and the ability to extravasate to disease sites largely improves the safety and tolerability of the therapy, best shown by reduced cardiotoxicity of liposomal doxorubicin (Doxil) compared to the free drug[2]. This evidence led to the approval of Doxil for the treatment of Kaposi's sarcoma by the US Food and Drug Administration (FDA) in 1995. Despite all these advantages, the drug loaded carriers have to face a complex series of biological barriers that limit the site-specific accumulation. Among all the obstacles, we have to take in account the opsonization process and the sequestration by phagocyte system (MPS), pressure gradients, endosomal and lysosomal escape and drug efflux pumps[3].

Nanoparticles, due to their size, can undergo internalization pathways (mainly endocytosis) that do not occur for small molecules[4]. Nanocarriers loaded with macromolecules, such as proteins and oligonucleotides, can be internalized by endocytosis and then traffic to lysosomes, where the release and the degradation of the loaded drugs occurs[5]. A vast amount of resources are continuously invested in the design of innovative multifunctional nanocarriers to proper overcome the biological barriers and avoid the rapid sequestration by macrophages. The chemical manipulation of the surface properties of nanovehicles with multiple functionalities enables specific distribution. A targeting agent is a ligand that binds a specific receptor in the body. Conventionally, targeted nanocarriers are directed towards tissues that overexpress a specific receptor which can ameliorate the therapeutic efficacy of treatment. Regrettably the protein corona around the nanoparticles, as direct consequence of the aforementionedopsonization process, might mask targeting ligands, resulting in decreased specific accumulation. The opsonisation is dependent on the particle size, surface charge, hydrophobicity and surface decoration. In particular, many studies highlighted that neutral hydrophilic particles undergo less

opsonisation as compared to hydrophobic charged ones[6-8]. In the light of this, the widely surface decoration with hydrophilic polymers, such as polyethylene glycol (PEG), is a powerful strategy to limit undesired protein adsorption. Notably a hydrophilic PEG polymer on a nanoparticle surface creates an elastic shell able to counterbalance the attraction forces between opsonins and the particle surface[9]. Nevertheless, nanocarriers may aggregate in biological systems due to the high ionic content of the plasma.

Recently, sophisticated systems for better control over drug distribution and release have been generated. Stimuli-responsive carriers represent a promising approach for targeted drug delivery, since the drug release is triggered by external stimuli, that might be physical, chemical or biological (e.g. pH, temperature, ultrasound, enzymes etc.).

Among the many different drug delivery systems developed in the last decades, gold nanoparticles (GNPs) have emerged for their unique combination of properties which allow them to act as a multifunctional platform: they can serve in the imaging and diagnosis fields[10], in the delivery of therapeutic agents to disease sites[11] but also as transfection agents for selective gene therapy or to monitor and guide surgical procedures[12-14]. Furthermore, as a result of their physico-chemical composition these metal nanovectors can be exploited as sensitizers in physical approaches such as the thermal ablation[15] and radiotherapy[16], and the emerging sonodynamic treatment [17].

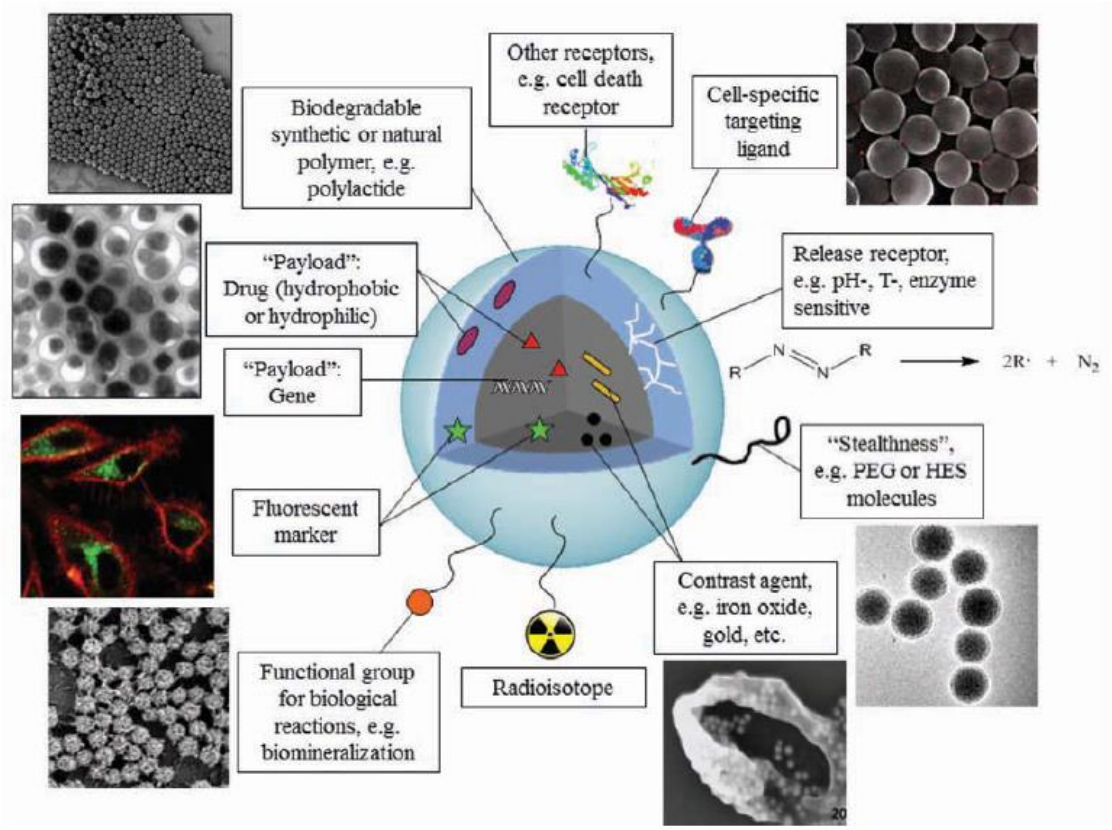

Figure 1. Graphical representation of some of the common approaches currently used to develop multifunctional nanocarriers and its bio-applications[18].

4.1. CANCER AND THERAPY

Cancer is currently one of the leading cause of death worldwide and is responsible for approximately one quarter of all deaths in the USA and UK[13]. About 70% of all cancer deaths occurred in low- and middle-income countries and a further rapid rise is pending soon (over 13.1 million deaths in 2030[19]).

4.1.1. Carcinogenesis

Cancer begins with a cell, or a group of cells, that starts to replicate in an uncontrolled way. Cancers which gains the ability to invade other tissues are called maligns, while benign tumours are not invasive and remain in the origin tissues without irreversibly compromising organ functionality. Cancer cells can spread from the tissue where they first generate to others through a fast growing blood and lymph systems able to avoid the recognition by the immune system. There are more than 100 different types of cancer, and most cancers are named by the organ or type of cell where they start (e.g.

lymphoma, melanoma). Physiologically, cell proliferation is controlled by a delicate equilibrium between pro-proliferation and anti-proliferation biochemical mediators and the replication cycle is carefully regulated[20]. This equilibrium ensures cell replication and growth when it is needed (i.e. during child growth, tissue repair after an injury and tissue regeneration) and contributes to the homeostasis of tissues and organs sizes during life. In addition to fast replication, cancer cells develop angiogenic ability and drug resistance which contribute to the peculiar features of tumour tissues.

The cancer genesis is due to DNA damages or alterations. Over time, DNA accumulates changes that the DNA maintenance mechanisms, such as nucleotide- and base-excision repair, homologous recombination, end joining, mismatch repair and telomere metabolism, are unable to solve. This leads to activation of proto-oncogenes and inactivation of tumour-suppressor genes[21]. Proto-oncogenes encode proteins that activate mitosis. As a consequence of mutations, they become oncogenes provoking overexpression of cell division signals and leading to uncontrolled mitosis. Tumour-suppressor genes encode proteins that stop cell division in order to repair genetic damages.

The causes of these alterations are associated with environmental agents such as the ultraviolet (UV) component of sunlight, ionizing radiation and numerous genotoxic chemicals, but also viral and hormonal factors.

The carcinogenesis process can be divided in 4 main stages:

- **Initiation:** permanent DNA damages caused by exogenous and endogenous factors. Irreversible step which proceeds very rapidly.
- **Promotion:** increased DNA synthesis to face the fast proliferation of the transformed cells. Changes induced by promotors are reversible and promotors do not transform cells that are not initiated.
- **Malignant conversion:** Carcinogenesis requires the conversion of benign hyperplastic cells to a malignant state, and invasion and metastasis are manifestations of further genetic and epigenetic changes.
- **Progression:** appearance of malignant neoplasms accompanied by genetic alterations which lead to karyotype change. In addition, a continuing evolution

of chromosomal abnormalities within the cell providing new "independent characteristics" such as the ability of invasion, metastatic growth, anaplasia.

During its multistep development, cancer acquires different capabilities identified as the six hallmarks of cancer which enable tumor growth and metastatic dissemination:

• *Inducing and Sustaining proliferative signaling:* Cancer cells deregulate the production and release of growth-promoting signals, even stimulating neighbor normal cells to supply various growth factors. Moreover cancer cells overexpress some specific receptor on the cell membrane rendering such cells hyper-responsive to otherwise-limiting amounts of growth factors. The activation of additional downstream pathways can result in somatic mutation. Then, the disruptions of negative-feedback mechanisms that ensure homeostatic regulation lead to the enhancement of proliferative signaling.

• *Evading Growth Suppressor and Promotion of Malignancy:* Cancer cells defect in tumor suppressor (such as RB and TP53 proteins) allowing persistent proliferation. Furthermore Contact Inhibition mechanisms, that in normal tissues operate to counterbalance proliferative signals, are abolished. Although TGF-β is a well-known anti-proliferative agent, recent studies has found TGF-β to activate in many late-stage tumors the epithelial-to-mesenchymal transition (EMT) program, which confers high-grade malignancy to cancer cells.

• *Resisting Cell Death:* The death process is divided in 3 main mechanisms: apoptosis, autophagy and necrosis. Apoptotic cells contract into small corpses which are consumed by neighbors. This process is activated in response to various physiologic stresses, such as high levels of oncogene signaling, DNA damages etc., and it is controlled by counterbalancing pro- and antiapoptotic regulatory proteins (Bcl-2 family). An imbalance toward the overexpression of antiapoptotic agents or downregulation of proapoptotic factors results in the attenuation of apoptosis, often associated to tumors with high-grade malignancy state. Autophagy, like apoptosis, operates at the basal levels in normal cells but can be induced in situations of strong cellular stress. Induction of autophagy can prevent tumorigenesis, either in association or not with apoptosis. Nonetheless, in analogy to TGF-β, autophagy mechanism seems to have conflicting effects on cancer cells and tumor progression.

Necrosis leads to the explosion of cells, with the release of the contents, and proinflammatory signals in the surrounding microenvironment which attract inflammatory cells of the immune system. These cells can be actively tumor promoting.

- *Enabling Replicative Immortality:* Contrary to cancer cells which show uncontrolled replication, normal cells can pass through a limited number of growth-and-division cycles. This limitation is due to senescence and crisis steps. Senescence is an irreversible non proliferative but viable state. Those cells which circumvent this barrier fall into the crisis phase and die. Rarely, some cells emerge from the crisis statement developing immortality, the capability of unlimited replicative potential. Many studies have highlighted that telomere shortening represents a clock device which controls cell proliferation. Telomerase is the DNA polymerase involved in the elongation of telomeres, the protecting ends of chromosomes. This is the reason why telomerase activation is correlated to the resistance to senescence and cell death, promoting uncontrolled replication of the cell. On the other hand, lack of telomerase can provoke the generation of tumor promoting mutation, whereas subsequent telomerase activation stabilizes the mutant genome and allows unlimited proliferation.

- *Inducing angiogenesis:* In adults angiogenesis is in a quiescent state and is turned on only transiently. Tumor progression leads to an “angiogenic switch” following the early stages of neoplasia, causing the continued growth of new vessels to sustain the expansion.

- *Activating Invasion and Metastasis:* The invasion and metastasis cascade begins with a local invasion, then the intravasation by tumor cells in the blood stream and lymphatic system, the extravasation into the parenchyma in distant tissues forming micrometastatic lesions, which finally develop macroscopic tumors. Cancer cells acquire a combination of attributes that enable invasiveness and apoptosis resistance, leading to metastasis.

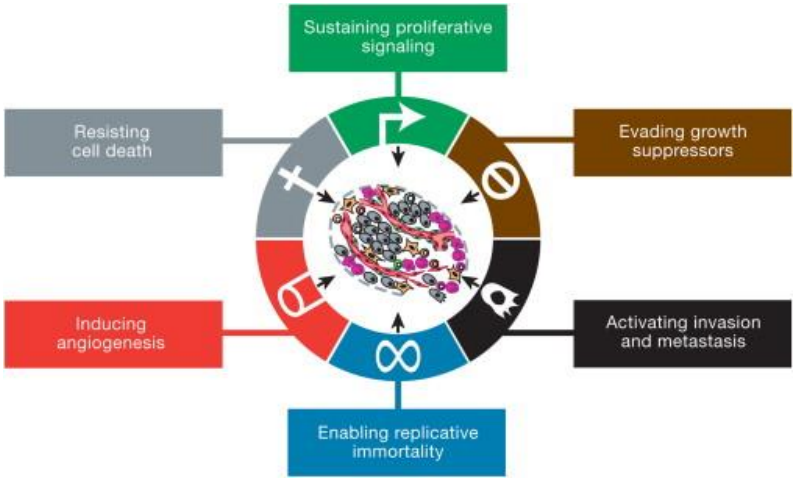

Figure 2. Representation of the six hallmark capabilities of cancer[22].

4.1.2. Anticancer therapies

Cancer is still one of the leading causes of death worldwide and the goal of a cancer therapy is to achieve efficient and selective treatments with less damage to healthy tissues. Many approaches are available; the choice of the therapy depends upon the localization, the stage of the disease and the performance status of the patient. The most common treatments for solid tumours are:

- *Surgical resection* including cryosurgery, hyperthermia and Photodynamic Therapy (local treatment).
- *Radiation therapy:* high doses of radiation are exploited to kill cancer cells and shrink tumours.
- *Chemotherapy:* a pharmacological systemic treatment.
- *Immunotherapy (cancer vaccines):* a biological treatment that helps the immune system fight cancer based on antibodies and cytokines.
- *Hormone therapy:* a cancer treatment that slows or stops the growth of cancer whose development is hormone dependent (monoclonal antibody, interferons).
- *Gene therapy:* this strategy aims at the insertion a functional gene into the host cells to correct errors of metabolism or alter or repair a genetic abnormality.
- *Stem Cell Transplant:* stem cells are given to replace those that were destroyed by chemotherapy and radiotherapy.

- *Angiogenesis inhibitors:* this strategy includes the administration of agents that interfere with the angiogenetic process by blocking signaling molecules and receptors.
- *Targeted therapies:* this strategy specifically delivers drugs towards cancer cells avoiding side effects.

Chemotherapy is a major therapeutic approach which may be used alone or combined with other forms of therapy. Classical antitumoural therapy involves the use of chemotherapeutics. These agents are, in general, small molecules that inhibit the replication or induce apoptosis of cells that divide rapidly, one of the specific cancer features.

An important drawback of this treatment is that antitumourals indiscriminately kill cancerous and healthy cells, harming also normal cells which constitutively replicate fast, such as bone marrow cells, cells in the digestive tract, hair follicles. An uncontrolled systemic distributions diminish the drug concentration in the disease site, thus high drug doses are required to be effective against the tumour, leading to intolerable cytotoxic effects such as myelosuppression, gastrointestinal distress and anaemia.

A long term administration of a specific drug at high doses can lead to multidrug resistance (MDR) reducing the therapeutic effects: there's a delicate balance between drug sensitivity and resistance displayed by target tumour cells. MDR is mainly due to overexpression of efflux pumps (e.g. P-glycoprotein) in the cell membrane, which are responsible for transport of drugs out of cells, or upregulation of genes which can overcome the damage of these agents[23]. Often chemotherapy involves the use of different anticancer agents and supportive drugs; this combination can lead to drug interactions which represent a real clinical concern in patient toxicity or therapeutic response[24]. Moreover, most of the anticancer drugs show poor solubility in aqueous solutions requiring solvents that contribute in increasing the formulation toxicity.

Among the anticancer drugs on the market, anthracyclines, cyclophosphamides, taxanes, and fluorouracil are some of the most useful antineoplastic agents, displaying a broad range of clinical activity against several solid and haematological malignancies[24,25]. Their main common problem is that they lack selectivity toward cancerous cells and indiscriminately kill cancerous and healthy cells.

New therapeutic strategies are rapidly progressing in order to overcome all the limitations of conventional anticancer drugs:

- High-volume cellular screening for anticancer agents with combinatorial chemical libraries or by in silico research.
- New target for anticancer drug design such as specific antigens and receptors overexpressed by certain types of tumour, transduction signals, and antiangiogenics factors.
- Gene therapy and antisense oligonucleotides.
- Administration of antitumourals by drug delivery systems (DDS) to enhance the selectivity of the therapy.

Looking at the market, some of the chemotherapeutics are alkylating agents or anti-metabolites that act on DNA and RNA molecules, causing crosslinking and blocking the replicative process. Other examples of drugs currently on the market are anti-microtubule agents, topoisomerase inhibitors and cytotoxic antibiotics which inhibit cell mitosis.

The new frontier of anticancer therapies is a high specific treatment against tumour cells that prevent damage to healthy tissues.

The combination of different treatments can generate new effective strategies such as:

- *Neoadjuvant therapy (pre-surgery treatment):* approached to shrink a tumour allowing surgical resection or radiotherapy.
- *Adjuvant therapy (post-surgery treatment):* after a surgical excision of the tumour mass, chemotherapy and radiotherapy are administered to eliminate any micro metastases and to prevent relapses.

Notably, in November 2014 the Food and Drug Administration (FDA) approved Bevacizumab solution for intravenous infusion (Avastin®, made by Genentech, Inc.), in combination with Paclitaxel, PEGylated liposomal doxorubicin, or Topotecan, for the treatment of patients with platinum-resistant recurrent epithelial ovarian, fallopian tube, or primary peritoneal cancer. The Progression-free survival assessment demonstrated a statistically significant improvement in patients who received Bevacizumab plus chemotherapy compared with those who received chemotherapy alone ($p<0.0001$)[26].

Even the combination of physical approaches to pharmacological treatment, such as thermal, mechanical or biochemical damage, can produce a selective and effective cell killing.

Hence, a multidisciplinary strategy can become the standard approach to avoid an inadequate management of side effects and to improve clinical outcomes and quality of life.

4.1.3. Sonodynamic therapy

Sonodynamic therapy (SDT) is a noninvasive approach which involves the synergistic effect of sonosensitizer and ultrasound on tumor damage. Individually, these components are non-toxic but when combined together generate cytotoxic reactive oxygen species (ROS) [27], responsible of irreversible destruction of tissues. Ultrasound is a kind of mechanical wave able to penetrate into depth through human tissue with weak decade. As a result SDT can be exploited even for the treatment of deep seated malignant tumours[28]. Moreover, ultrasound can be tightly focused in a limited focal zone without affecting healthy tissues. The interaction of ultrasound with aqueous environments results in a unique phenomenon known as cavitation which consists of three stages leading to the release of energy: nucleation, growth and implosive collapse of gas-filled bubbles. The implosion of these bubbles leads to extreme temperatures and pressures responsible for the ROS generation.

With the development of SDT, some adjuvant agents were introduced to enhance its curative effect, like porphyrins, xanthene-based sensitizers etc. Despite their potency in the enhancement of SDT effect, most of sonosensitizers suffer of poor water solubility, chemical instability and uncontrolled distribution causing a decreased ROS production. Moreover, even if ultrasound is generally considered " safe", it can affect tissue through a variety of mechanisms, mainly thermal or non-thermal, depending on various factors such as the intensity of the beam, the duration of exposure and frequency[29].

As a result, there has been increasing interest in using drug delivery systems to allow a preferential accumulation of sonosensitizer. Nanotechnology offers the great possibility to manipulate molecules and supramolecular structures to produce devices with programmed functions. Recent studies showed that gold nanoparticles, owing to their special physical properties, can accelerate the cavitation phenomena,

emerging *per se* as therapeutic nano-sonosensitizers. Notably gold nanoparticles have a good biocompatibility and their surface can be decorated with suitable targeting agents to exert a preferential accumulation in tumors where the local ultrasound exposure contributes to selective elimination of tumors.

4.2. PATHOPHYSIOLOGY OF TUMOUR TISSUE

Overexpressed receptors, mutated proteins and other molecules that interfere with key transduction signalling pathways are some of the major targets for drug development in order to eliminate mutated cancer cells. Although this common strategy can be initially successful, multidrug resistance can lead to a disease relapse. This implies some missing links between the actual underlying carcinogenic mechanisms and current drug development. Recently, tumour microenvironment has been recognized as a key contributor for cancer progression, invasion and metastasis[30]. As proposed by Steven Paget, cancer is not an isolated group of cells, it is a "seed" which needs a fertile "soil" (the microenvironment)[31] to grow. Cancer tissue presents a complex pathophysiology and biological features which differ remarkably from healthy tissue. In light of this, targeted therapies have been developed taking advantage of all these characteristics to enhance the treatment efficacy. The more evident alterations which tumours undergo are at cellular, molecular and metabolic level, as a result of different gene activations.

Hypoxia. Uncontrolled cell division is fundamental for fast growth of the tumour mass; this process requires a considerable quantity of oxygen. Due to poor capillary development, oxygen tension decreases to 0-20 mmHg, while in normal tissues it is in the range of 24-66 mmHg[32], thus causing hypoxic conditions. The association of hypoxia to malignant tumour development has been observed in human tumours, since oxygen depletion can affect the regulation of pathways promoting angiogenesis, and causing necrosis. Oxygen radical production and reoxygenation of the tumour after hypoxia will drive additional oxygen radical formation[33]. Moreover, as firstly reported by Gray L.H. in 1953, hypoxia can produce aggressive phenotypes that are more resistant to radiotherapy and chemotherapy and favouring the tumour progression[34].

Acidic pH. Tumour tissues often exhibit an acidic pH, which is a consequence of high production of acidic metabolites such as lactic acid. The fats replication process needs to be supported by a high amount of energy. Healthy cells get energy from aerobic glycolysis by oxidation of pyruvate, which takes place within the mitochondria. By contrast tumour cells prefer the glycolytic pathway, even if oxygen is abundant.
An insufficient cellular respiration, due to inadequate oxygen supply or mitochondrial damage, can cause an increase of glucose consumption, switching the metabolism to anaerobic glycolysis. This effect was first postulated by Warburg, so called "Warburg effect"[35]. The massive production of lactic acid, mainly due to lactate dehydrogenase activity, and the subsequent activity of proton pumps are the major causes of the low extracellular pH[36]. High levels of lactate can help tumour cells to escape from the immune system, promoting a chronical inflammation[37]. These changes are often supported by mutations which affect the tumour cell metabolism[38], such as genes for membrane-based ion transporters (e.g. the Na^+/H^+ antiport and the Na^+-coupled HCO_3^-/Cl^- transporter). Moreover the CO_2 accumulation can contribute in microenvironment acidification since it is processed into carbonic acid by carbonic anhydrase enzyme.
As a result of the modification of cancer cells' energetic metabolism, the pH value in the extracellular microenvironment of the tumour is around 6.4-6.8 instead of 6.9-7.4 as showed by normal tissue[39,40]. This mutate range of pH can be exploited to design pH responsive materials able to selectively deliver chemotherapeutics to cancerous cells.

Tumour vascular architecture. Cancer originates from a single neoplastic cell. The malignant mass grows up to a mass of 1-2 mm by exploiting the existing vessels which support healthy tissues[41]. A further increase in tumour mass generates a situation of hypoxia in the inner area of the mass itself, due to limited oxygen diffusion.
Thus, in order to guarantee an adequate supply of oxygen, nutrients and the removal of waste products, a tumour rapidly develops its blood supply, leading to a vascular architecture that is significantly different from that of normal tissue. Cancer vascular networks present tortuous vessels, loops, shunts, dramatically variable intervascular distances, and large avascular areas, generally absent in normal vascular

architecture[42]. The new vascular network development is triggered by up-regulation of pro-angiogenic factors and down-regulation of inhibitors of vessel growth[43]. Hypoxic conditions deriving from the increasing distance between the growing tumour cells and the capillaries can induce some angiogenic phenotypes[44]. The balance between pro-angiogenic and anti-angiogenic factors leads to structurally organized vessels, with a complete basal membrane to support the endothelium. In tumour tissue this missing balance produces a vascularization network with incomplete endothelium and ample fenestrations of 100-800 nm[45], compared to 50-60 nm of healthy tissues. As a consequence blood vessels show an enhanced permeability to macromolecular components such as plasma proteins and macromolecular therapeutics. Furthermore, leaky tumour vessels contribute to the generation of interstitial hypertension, which limits the delivery of drugs to tumour[46].

Enhanced Permeability and Retention effect (EPR effect). The peculiar structure of the tumour vasculature led to the discovery of the Enhanced Permeability and Retention (EPR) effect by Matsumura and Maeda who found that molecules with high hydrodynamic size accumulate in tumour more efficiently than in healthy tissues[47].
This phenomenon originates from two main reasons:

- Newly formed tumour microvasculature shows disorganization and lack of conventional hierarchy. Moreover the endothelial surface is fenestrated with gaps between endothelial cells, smooth muscle and a proper basal membrane are often lacking. Blood vessel leakiness enables molecules that cannot permeate healthy tissues to infiltrate deeply in the tumour matrix and reach cancer cells.

- A second important characteristic of tumours is the dysfunctional lymphatic drainage system: small molecules can diffuse back to the blood circulation, while macromolecules, such as colloids, which have a bigger hydrodynamic size, are entrapped into the tumour tissue, where they can easily accumulate.

The EPR effect is further enhanced by many pathophysiological factors such as bradykinin, nitric oxide, prostaglandins, vascular endothelial growth factor VEGF, and tumour necrosis factor.

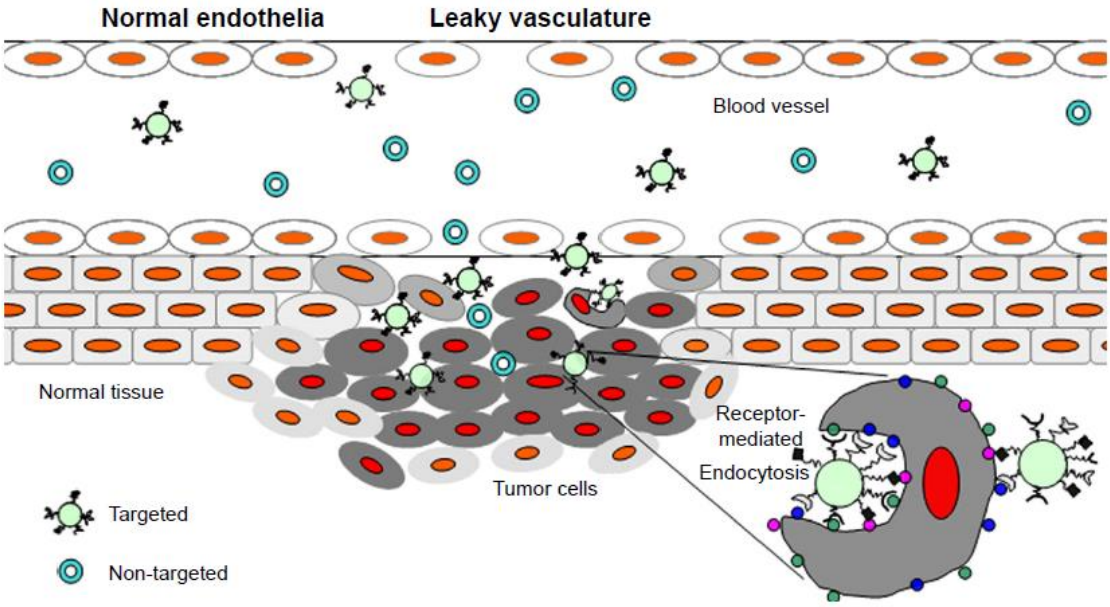

Figure 3. Schematic representations of the EPR effect in a cancer tissue. Nanocarriers can extravasate through the large fenestrations of the tumor capillary, as a consequence of the defective angiogenesis. Targeted nanoparticles can thus recognize a specific receptor expressed on the cell surface, triggering a receptor-mediated endocytosis[48].

Redox equilibrium. Cancer cells produce large quantities of hydrogen peroxide[49] since NADPH-oxidase is regulated by the GTPase Rac1, which is itself downstream of the proto-oncogene Ras. ROS can cause strand breaks, alterations in guanine and thymine bases, and sister chromatid exchanges[33]. This may deregulate the body's cellular defence system and lead to genomic instability[50].

4.3. PRINCIPLES OF NANOCARRIER DESIGN

Despite a century of perpetual discovery and development, nowadays formulations leave drugs incapable of localizing specifically at sites of interest. In this scenario nanotechnology has been increasingly applied to the area of drug development. Nanotherapeutics have emerged as suitable drug vehicles able to increase the solubility of high hydrophobic anticancer agents, overcome pharmacokinetic limitations of conventional drug formulations and realize a site-selective treatment by combining different targeting strategies. With all these worthy characteristics, nanocarriers can realize a potent, less toxic and site-selective treatment like the elusive magic bullet postulated by Paul Ehrlich. However, despite these potential advantages, only a relatively small number of nanoparticle-based medicines have

been approved for clinical use by regulatory authorities[51], with numerous challenges and hurdles at different stages of development. Lack of efficacy and safety are the main reasons of approval failure in later-stage clinical trials[52]. Nonetheless, there are some other concerns to consider. Nanoparticle-based systems are complex three dimensional entities which require a definite design, controlled production and highly reproducible scale-up process to obtain a product with all the desired physicochemical characteristics[52]. Overall, although many efforts have been made to redact nanomedicine's regulatory standards, there is still a lack of guiding considerations in the examination of nanoparticle-based medicines compared with conventional medicines.

Nanotherapeutics have to cross many biological barriers before reaching a successful accumulation within the targeted disease sites. Among the different obstacles which limit the efficacy of the treatment, there is the uncontrolled distribution of the therapeutics which freely diffuse into the body. The direct consequence is an inadequate drug accumulation in the target sites limiting the achievement of efficacious dose. Site-specific delivery represents a formidable challenge if nanocarrier design doesn't take into account the features of biological barriers and microenvironments encountered upon intravenous administration.

Particle extravasation from the blood stream: passive targeting. As described by Maeda and co-workers, tumour vasculature is characterized by incomplete endothelium and ample fenestrations which allow for colloid extravasation from the blood circulation. Moreover, the inefficient lymphatic drainage associated with high interstitial pressure retains these accumulated macromolecules, increasing the permanence in the disease site. The EPR effect depends on several parameters:

- *Size:* Several biological phenomena depend on nanoparticle size, such as circulation half-life, extravasation through leaky vasculature, macrophage recognition, biodistribution and the mechanism of cell uptake. Vascular endothelium of healthy tissue presents junctions of different size, depending on the tissue type. In most tissues pore size is below 2-6 nm, so too small for colloids to penetrate. Noncontiguous endothelia with vascular fenestrations of 40–150 nm are present in the liver and kidney glomerulus leading to

nonspecific accumulation of larger particles[53]. Moreover, spleen endothelium can have openings between 200–500 nm allowing the retention of particles >200 nm. Nanoparticles smaller than 5 nm are rapidly filtered by kidneys and cleared in the urine[54]. Particles with a dimension in the micrometer range (2–5 μm) can be exploited to target metastatic lung cancer since it has been proved to highly accumulate in this district[3]. In light of this, nanoparticles with a dimension range of 80-150 nm can guarantee for an optimal circulation time, consequently increasing the extravasation capacity into the tumour[55]. As size increases beyond 150 nm, more and more nanoparticles are entrapped within the liver and spleen.

- *Shape:* Distinct particle geometries affect dynamics, cellular uptake and in vivo fate[3]. Discoidal particles interact with vessel walls much more than spherical particles, with higher adhesion to the endothelium[56]. Many studies highlighted that high aspect ratio particles have prolonged-circulating lifetimes and so enhanced accumulation within tumours.[57]
- *Surface charge:* Particle surface charge can impact opsonization process, circulation times and interaction with resident macrophages. In particular cationic particles show a higher rate of nonspecific uptake probably as consequence of the interaction with sialic acids, important components of cell membranes. On the other hand, positively charged particles facilitate endosomal release through mechanisms, such as the “proton sponge” effect, preventing degradative effects of the endosomal compartment. Neutral and slightly negatively charged nanoparticles have longer circulation lifetimes thanks to the reduced protein adsorption.
- *Stealth-like behaviour:* Particle surface functionalization with hydrophilic flexible polymers stems the opsonization process and increases the circulation time. Polyethylene glycol (PEG) is the polymer of choice to produce stealth nanocarriers. The long circulation lifetimes and ability to extravasate to disease sites largely improved the safety and tolerability of nanoparticle-formulated drugs. This is the case of Doxil, pegylated liposomal doxorubicin, which showed a high stability and reduced cardiotoxicity compared to free drug.

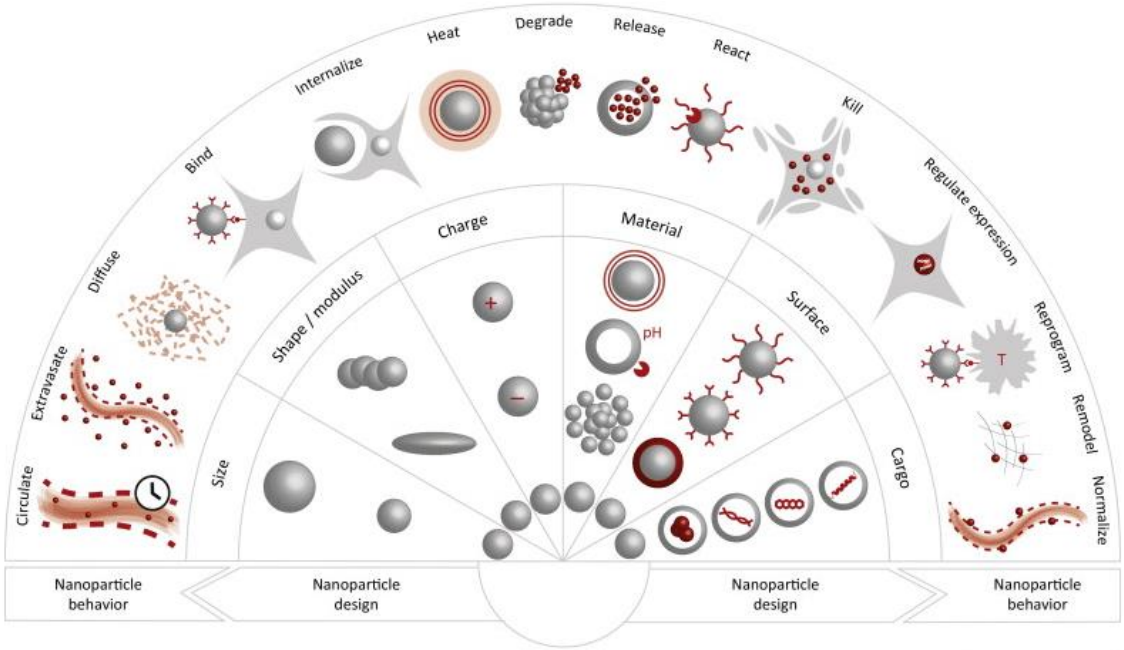

Figure 4. Nanoparticle designs, in terms of size, shape, modulus, charge, material, surface, and cargo, as well as their interactions in the body, determine their individual behavior[54].

Although the EPR effect in tumors has propelled the field of nanoparticle-based drug delivery, the phenomenon has been shown to vary dramatically with regards to the degree of tumor vascularity, tumour type and the expression of permeable factors.

Evasion of macrophage sequestration. After intravenous administration, nanoparticles are coated by a layer of plasma protein called opsonins. The protein corona is recognized by specific receptors on the surface of phagocytes which sequester nanoparticles. The opsonization process depends on size, surface charge, hydrophobicity and surface chemistry[58].

Cellular internalization: active targeting. Low molecular weight hydrophobic molecules easily diffuse through the cell membrane. On the contrary, supramolecular systems require active uptake mechanisms. Efficient targeting may be obtained by conjugation of specific target molecules, distinguishing of tumour type, organ or tissue. Many targeting moieties can be used for the chemotherapeutic delivery specifically to cancer cells: antibodies, peptides, lectins, sugars, and vitamins are some examples[59]. Cancer cells require abundance of oxygen and nutrients to sustain the rapid proliferative activity and promote tumour invasiveness. For this reason several receptors are up-regulated in some cancer tissue and may play a role in

cancer progression (e.g. Human epidermal growth factor receptor 2 (HER2), Folate receptor, Transferrin receptor[60]).

The term "active targeting" simply means a specific "ligand–receptor type interaction", condition that occurs only after blood circulation and extravasation. A long circulation time can ameliorate drug accumulation in tumour site. Consequently "active targeting" by itself does not automatically translate into effective delivery to the entire tumor, while the combination of passive and active targeting can further increase the drug accumulation.

Once drug carriers reach cancer cells, an efficient ligand–receptor interaction is dependent upon a variety of factors which include: targeted cell selective expression of the receptor relative to non-target cells, receptor availability on the target cell surface, the rate of internalization against shedding of that surface receptor following ligand binding, etc[61].

Even the targeting agent density on particle surface can influence the uptake efficiency. It has been shown how decoration of particles with multiple copies of such targeting ligands can increase the avidity of particles for target-cell binding, via the cooperative nature of multivalent binding to cell-surface receptors[62].

Drug release. When interaction with the receptor occurs, the drug can have two fates:

a) Drug is released from the carrier in the extracellular space, and then diffuses into the cell.

b) Carrier is internalized, and then the drug diffuses out of the carrier (if physically entrapped) or it is released by bond cleavage (if chemically conjugated to the carrier) upon reaching the endosomal compartment. Some proportion of the encapsulated material can escape the endosomes and traffics to its intracellular site of action.

The release mechanism can be triggered by several stimuli:

- *Temperature:* Thermosensitive polymers exhibit a phase transition at a certain temperature, called LCST, which results in changes in conformation, solubility and hydrophilic-hydrophobic balance. The drug release could be in response to an endogenous temperature increase which makes the

thermosensitive polymer collapse, or to an externally applied temperature increase[63].

- *pH:* pH change can induce the polymer hydrolysis and consequent disruption of the vesicle and drug release[64]. Another method to realize a controlled drug release upon pH change is the chemical conjugation of the drug to the carrier via a pH-sensitive bond (e.g. hydrazone bond, azo bond, citraconic amide bond).
- *Oxidation/Reduction:* Polymers which contain disulfide bonds between the hydrophobic and hydrophilic blocks reveal a good stability in the typically oxidizing

  extracellular environment, and lability once within the intracellular compartments. In particular, the elevated level of glutathione (GSH) found in many tumours can be exploited to realize a redox sensitive system able to selectively release content in the cytosolic compartment[65].
- *Ultrasound:* Ultrasounds are an effective harmless method which allow for a spatiotemporal controlled drug release. US are noninvasive and the tissue penetration depth can be easily regulated by varying frequency, duty cycles and time of exposure. Ultrasound treatment can induce the release of the drug by either thermal or mechanical effects generated by cavitation phenomena or radiation forces.
- *Light:* Drug release can be induced by illumination at a specific wavelength. An interesting system was reported by Mabrouk and coworkers who introduced azobenzene moieties to polymerosomes. Illumination with UV light triggered a conformational change in the membrane inducing polymerosome disruption.

4.4. ENDOCYTOSYS PATHWAYS

The plasma membrane is a fluid, dynamic, semi-permeable bilayer that surrounds cells and forms a barrier which gates access to the cell, permitting entry to nutrients and extracellular messenger molecules, but locking out hazardous compounds and deadly viruses[66]. The internal composition of the cell is maintained by specific transport proteins which mediate the selective transport of small molecules such as aminoacids, sugars and ions. On the other hand, macromolecules are internalized via

receptor-mediated endocytosis (RME) which involves the interaction with specific receptors on cell surface. Macromolecules are carried into the cell in membrane-bound vesicles derived by the invagination and pinching-off of pieces of the plasma membrane in a process termed endocytosis. Endocytosis involves many mechanisms that can divided in two main categories:

- *Phagocytosis:* this is a highly controlled process for the uptake of large particles and represents a prerogative of mammalian cells. Specific cell-surface receptors and signalling cascades mediated by Rho-family GTPases are involved[67,68].
- *Pinocytosis:* this is a fluid-phase uptake which occurs in all cells. Pinocytosis can be further divided into three main pathways: clathrin-mediated pathway, caveolae-mediated endocytosis and clathrin and caveolae independent pathway[69].

Deep knowledge of the endocytic pathways will allow the design of drug delivery systems able to release their drug payload only inside the cell, with obvious advantages in term of systemic toxicity and side effects.

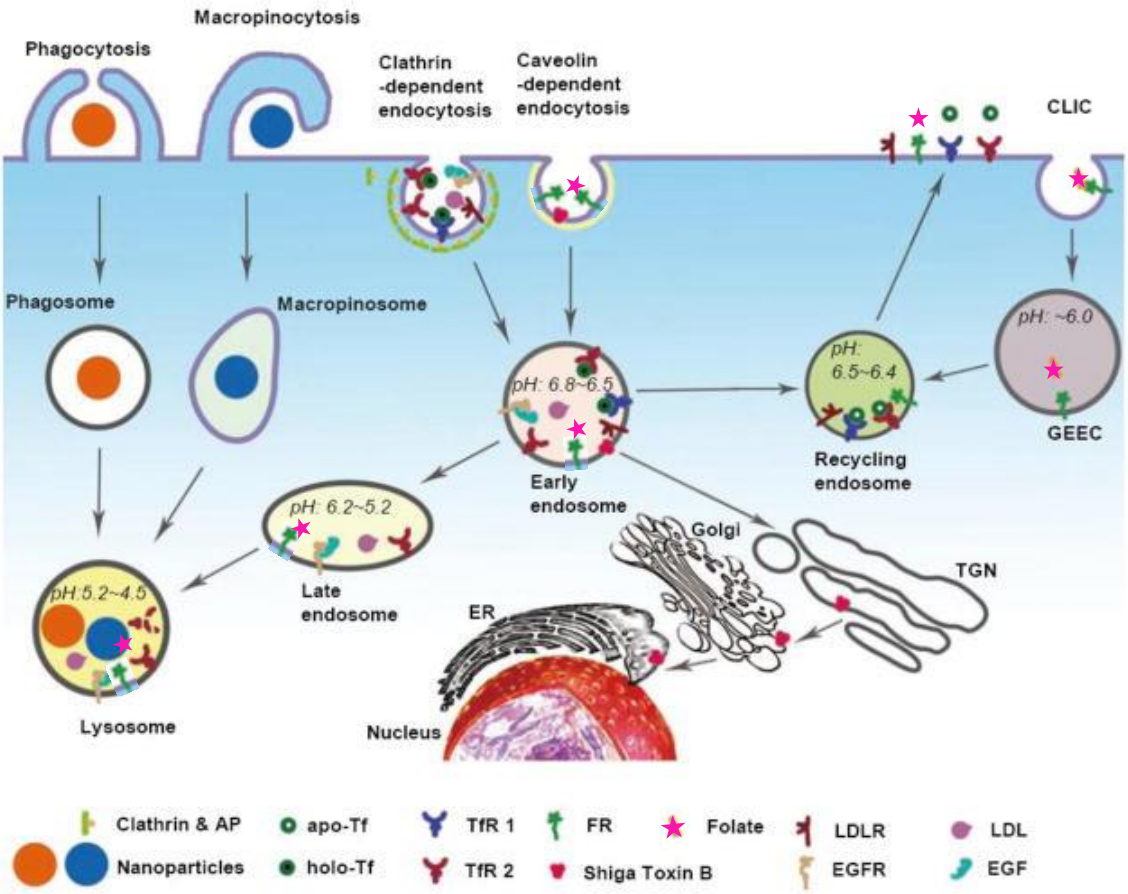

Figure 5. Multiple cell uptake mechanisms. The endocytic pathways differ with regard to the size of the endocytic vesicle, the nature of the cargo (ligands, receptors and lipids) and the mechanism of vesicle formation[70].

4.4.1. Clathrin mediated endocytosis

Clathrin mediated endocytosis (CME) is a constitutive process in mammalian cells and it is involved in the uptake of nutrients, growth factors, pathogens and receptors[69]. Cargo is packaged into vesicles of well-defined size that are surrounded by a coat predominantly made of the protein clathrin and adaptor protein complexes[71]. Clathrin shows a triskelion shape composed of three clathrin heavy chains and three light chains. It forms a polyhedral lattice surrounding the vesicle which mediates the cargo internalization. The uptake process is highly selective and includes 4 key steps, illustrated in Figure 6.

• *Initiation and cargo selection:* cargo recognition by specific receptors on cell membrane.

• *Coat assembly:* concentration of high-affinity transmembrane receptors and their bound ligands into 'coated pits' on the plasma membrane which are formed by the assembly of clathrin (clathrin-coated pits, CCPs).

• *Scission:* CCPs invaginate and pinch off to form endocytic vesicles (CCVs) that are encapsulated by a polygonal clathrin coat and carry concentrated receptor–ligand complexes into the cell. Finally the conditions are ripe for the assembled scission molecule dynamin and subsequently the uncoating molecule auxilin to function.

• *Uncoating:* After that, clathrin is usually removed from the vesicle (clathrin recycle), whose final size is around 120 nm[68]. When the internalization occurs through this pathway, the vesicle finally fuses with an endosome and, later on, the endosome fuses with a lysosome in which the internalized particle can be degraded. The pH of the endo-lysosome gradually drops from about 6 in the early endosome to around 5 in the late endosome, due to proton pump activity[72].

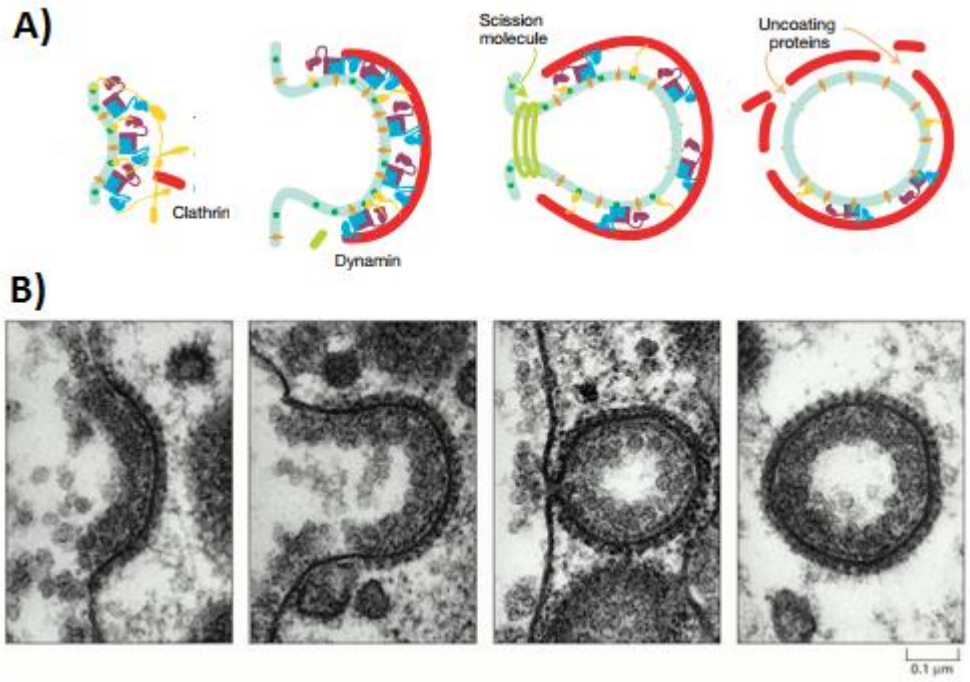

Figure 6. The Key Steps in Clathrin-Mediated Endocytosis: endocytic vesicles starting from clathrin-coated pit. Graphical representation (A) and TEM images of the process over time (B).

Intracellular transport and processing after receptor-mediated endocytosis vary markedly among different receptor-ligand systems and different cell types, and determine the fate of drug-carrier composites to specific intracellular destinations. Endogenous ligands and receptors can follow various routes:

- Receptors are recycled along with the ligand, back to the site from where the receptor originated.
- Receptors can move to lysosomes and, with the ligand bound to them, share the fate of the ligand.
- Receptors can provide for intracellular transport of ligand and return to the initial plasma membrane domain.
- Receptors can return to a different domain of the plasma membrane (transcytosis).

When the internalization occurs through this pathway, the vesicle finally fuses with an endosome and, later on, the endosome fuses with a lysosome where the internalized cargo is degraded. Through its route, cargo encounters a mildly acidic pH in early endosomes (6.8-6.5), an acid pH in late endosomes (pH 6-5) and finally reaches a strongly acidic milieu in lysosomal compartments (pH 5-4). These different pH conditions can promote the dissociation of the ligand-receptor complex and the degradation of vesicle cargos.

4.4.2. Caveolae-mediated endocytosis

Caveolae are flask-shaped invaginations of the plasma membrane. The shape and structure are conferred by caveolin, a dimeric protein that binds cholesterol and self-associates to form a striated caveolin coat on the surface of the membrane invaginations[68]. Many signalling molecules are associated with caveolae and are involved in key signalling cascades, such as cholesterol homeostasis. In most cells, caveolae internalization rate is quite slow and the small vesicles, 60-80 nm in diameter, can carry little fluid-phase volume[73]. Caveolin pathway is one division of the non-clathrin endocytic pathways and, even if the internalization process is very similar to CME, it doesn't involve any enzymatic activity. Folic acid and albumin are ligands usually undergoing internalization by Caveolae-mediated endocytosis.

4.4.3. Clathrin- and caveolae- independent pathway

Caveolae represent just one type of cholesterol-rich microdomain on the plasma membrane. Others, more generally referred to as 'rafts', are 40–50nm structures that diffuse freely on the cell surface[68]. These small rafts internalize extracellular fluid, GPI-linked proteins, Interleukin-2 and growth hormone receptors etc. One such pathway is GPI AP-enriched early endosomal compartments (GEECs) which delivers cargoes to endosomes through the formation of acidic, tubulovesicular compartments[73]. Even if the recruitment of GPI-linked proteins into these endocytic structures is dependent on the GPI moiety, the mechanisms that govern clathrin- and caveolae- independent endocytosis remain poorly understood.

4.4.4. Folate receptor endocytosis and trafficking

Folic acid (Figure 7.) is an essential vitamin which cannot be synthetized by humans and must be supplied through diet. Folates are important one-carbon donors in *de novo* nucleotide synthesis of eukaryotic cells. For this reason, Folate deficiency is associated with many diseases, including fetal neural tube defects, cardiovascular disease and cancers[74].

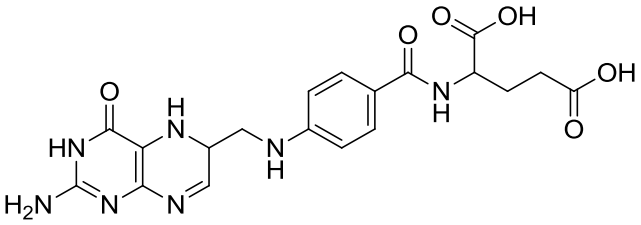

Figure 7. Chemical structure of Folic acid.

Folate uptake is mediated by different transporters. Reduced Folate Carriers are ubiquitously expressed anion channels with a low folate-binding affinity (K_d = 1–10 μM) that transport reduced folates directly into the cell cytosol. By contrast, high-affinity uptake of folic acid is mediated by Folate Binding Proteins (FBP), known also as Folate receptors (FR). Folate receptors (FRα, FRβ and FRγ) are cysteine-rich cell-surface glycoproteins that bind Folate oxidized form with high affinity (K_d < 1 nM) to mediate its cellular uptake. FRα and FRβ are (GPI)-anchored whereas the FRγ isoform

is a soluble protein[75]. Folate receptors are identified as low capacity transporters that require to recycle back to the cell surface[76]. Although Folate receptors are expressed at low levels in most of healthy human tissues, FRα isoform expression is up-regulated in a large number of epithelial malignancies to sustain the demand for rapid cell replication[75]. For this reason, FR is exploited as diagnostic marker of various tumors (e.g. brain[77], and ovarian cancers[76]), but also as targeted drug delivery to cancer tissues.

FRα possesses a globular structure stabilized by eight disulphide bonds and contains a deep open folate-binding pocket. The folate pteroate moiety is hidden inside the receptor, while its glutamate moiety is exposed to the solvent. Notably, Folate shows two carboxylic groups: the one in α position is responsible for the biological activity, while the γ-carboxylic group can be conjugated to drugs without affecting the affinity for the receptor[74].

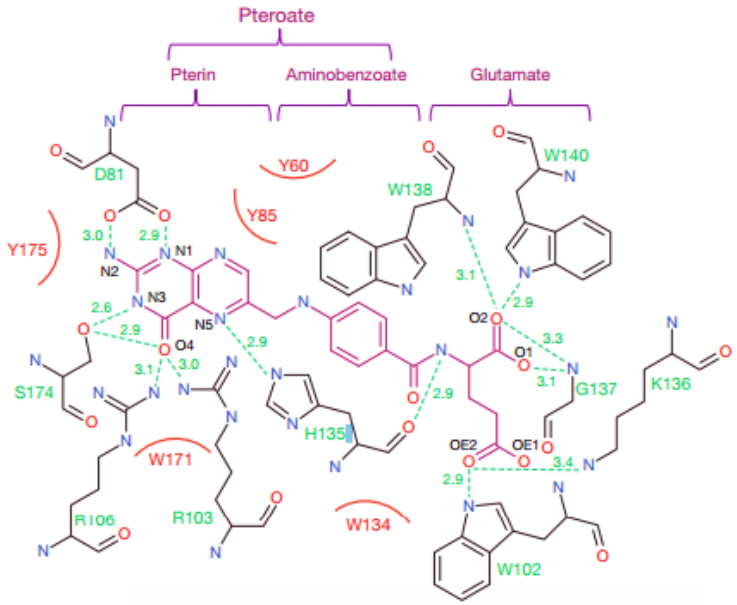

Figure 8. Interaction map of folic acid with ligand-binding-pocket residues. The folic acid chemical structure is shown in magenta, pocket residues in black and hydrogen bonds as green dashed lines with bond distances (Å) indicated. Hydrophobic interactions are presented as curved red lines. The pteroate and glutamate moieties of folic acid are indicated above the map[74].

Quantitative analysis of Folate receptor distribution highlighted the diffusely distribution on cell membrane, and only after cross-linking there is a substantial folate receptor enrichment localized to caveolae[75,78]. Although FR redistribution and clustering to caveolae was not mediated by folate binding, it is however induced by

incubation with cross-linking antibodies. As confirmed by many studies reported in literature, endocytosis of GPI-APs is mediated by clathrin-independent pathway[79,80], in particular GEEC compartments appear to be involved in the delivery to late endosomes[75,81].

After folic acid binds to the transmembrane receptor, internalization occurs via caveolae-mediated pathway, and then the ligand is released from the complex in an acidic intracellular compartment and exported from the intact endosome into the cytoplasm. This putative exporter was shown to require a trans-endosomal pH gradient[82].

The described process is termed potocytosis and is specific for small molecules, such as folic acid. The rate of FRα internalization is not affected by folic acid binding: a dynamic exchange between the internalizing receptors and an internal pool guarantees a constant number of FRs on the cell surface[83].

Granted the specific FR overexpression by some human tumors, folic acid can be exploited for efficient intracellular delivery of anticancer agents[84]. Several nanocarriers such as cyclodextrin, dendrimers, gold nanoparticles and liposomes, have been widely decorated with folic acid. Many studies highlighted important implications of multi-ligand attachment per nanoparticle for the development of more effective targeting systems. Multivalent targeting

devices can provide dramatic improvements in avidity by enhancing the resident time of the drug on the cell target[85]. On the other hand, increasing the average number of ligands per nanoparticle will create competition among multiple ligands for a single receptor, limiting the access that ligands have to receptors[86]. In several reports it was further shown that once a certain threshold in the ligand density is reached, there is no further improvement of internalization efficiency, due to the receptor saturation effect.

Moreover, multivalent targeted carriers can induce receptor clustering, as reported for folate receptor[87], $\alpha_v\beta_3$ integrin[88] and the transferrin receptor[89]. Targeting these clusters can be optimized by decorating carrier surface with intermediate ligand density, to assure multiple nanoparticles binding to each cluster. On the contrary, too high ligand density will hinder the binding of the same cluster to other particles, because of the high ratios of receptors bound per nanoparticle[86]. Even the use of linkers to connect the nanoparticle surface and folate can affect the affinity to the

receptor. For instance, PEG linker with different lengths and flexibility could increase the availability of targeting ligands and alleviate potential steric hindrances.
In conclusion, there are so many factors that can affect the affinity for the receptor, the uptake efficiency and even the internalization pathway.

4.5. ENVIRONMENTALLY RESPONSIVE CARRIERS FOR CANCER THERAPY

Various in *vivo* studies have demonstrated that the specific delivery of antineoplastic drugs can be obtained by incorporation of active targeting moieties that bind to antigens or receptors overexpressed on the target cells relative to normal tissues.
Despite their potential for increased drug half-lives, stability and improving a drug's propensity to accumulate at sites of injury, the nanocarriers have to face a complex framework of sequential biological barriers that severely limit site-specific bioavailability, preventing achievement of proper therapeutic outcomes[3]. A vast amount of research and resources are continually invested in the incorporation of innovative design features within traditional nanocarrier constructs for proper negotiation of biological barriers, resulting in the creation of multifunctional nanoparticles. The structural particularity of the vascular endothelium and the micro-environmental characteristics (pH, temperature, redox potential and enzymatic composition) can be exploited to control the delivery of drugs in specific tissue, organ or intracellular compartment. For these reasons, stimuli-responsive systems are becoming more important in the field of anticancer therapy as it is possible to tune and control their properties at the molecular level by applying certain external triggers. Thus, stimuli-responsive nanomedicines could be one class of possible candidates to fulfill all the requirements of "magic bullets", able to realize an on-demand drug delivery.
This approach requires the use of biocompatible materials that are able to undergo a specific protonation, a hydrolytic cleavage, or a molecular or supramolecular conformational change in response to a desired stimulus[90].
Among the array of the stimuli-sensitive systems, pH responsive nanocarriers have been the most investigated: the wide range of pH gradients available in different tissues and subcellular compartments in physiological and pathological conditions can be exploited to exercise a finely carrier response.

Moreover, several exogenous physical stimuli can be applied to the disease site to allow for tailored release profiles with excellent spatial, temporal and dosage control. Among the various external stimuli, thermoresponsive drug delivery is among the most investigated stimuli-responsive strategies, and thus has the highest potential for clinical applications. Temperature sensitive carriers are generally liposomes, polymer micelles or nanoparticles whose constituents are generally lipids or polymer (usually poly(N-isopropyl acrylamide), PNIPAM). These materials are able to switch from the hydrophilic to the hydrophobic state upon dehydration when exposed to temperatures above the LCST (Lower Critical Solution Temperature). This switch takes place because at lower temperatures the hydrogen bonds between the polymer and water molecules maintain the adequate polymer hydration thus allowing the polymer dissolution. As the temperature increases, the water is desorbed from the polymer and hydrophobic interactions among the side chains of polymers become prevalent. This behaviour leads to finely control on the release of the drug following a variation in the surrounding temperature. Ideally thermoresponsive nanocarriers should retain the cargo at body temperature (~37 °C), and rapidly release the drug within a locally heated tumour (~40–42 °C). Thermosensitive liposomes are at the present the most advanced thermoresponsive nanosystems and thus have the highest potential for clinical applications. Lyso-Thermosensitive Liposomal Doxorubicin (LTLD) is a proprietary heat-activated liposomal encapsulation of doxorubicin, an approved and frequently used oncology drug for the treatment of a wide range of cancers (Phase III clinical trial for primary liver cancer and a Phase II clinical trial for recurrent chest wall breast cancer).

4.6. GOLD NANOPARTICLES AS CARRIER FOR DRUG DELIVERY APPLICATION

4.6.1. Historic introduction

Gold is a transition metal with a high stability thanks to its electronic configuration: $[Xe]4f^{14}5d^{10}6s^{1}$. Since the 6s orbital with one electron is contracted, this electron is more tightly bound to the nucleus and less available for bonding with other atoms. The 4f and 5d orbitals expand, but cannot be involved in bond formation since they are completely filled. Under standard conditions, gold is solid. In its bulk form, this element is a dense, soft, malleable and ductile metal with a bright yellow colour and

luster. The extraction of gold started in the 5th century B.C. in Bulgaria and reached 10 tons per year in Egypt around 1200-1300 B.C. when the marvellous statue of Touthankamon was constructed[91]. Its soluble form, colloidal gold, first appeared in China and Egypt around the 5th century B.C. for therapeutic and decorative purposes. A famous example is the Lycurgus cup, from the 4th century A.C., visible at the British Museum in London: the cup is ruby red in transmitted light and green in reflected light, due to the presence of gold colloids. In antiquity, gold solutions were used for curative purposes for various diseases, such as heart and venereal problems, dysentery, epilepsy, and tumours. In the 17th century the heterocoagulation of gold particles and tin dioxide became popular as glass-colouring process, called "Purple of Cassius". In 1857, Faraday reported the first scientific article on gold nanoparticle (GNPs) synthesis by reduction of tetrachloroauric acid solution using phosphorus in CS2 (a two-phase system), following a procedure already reported by Paracelsus in 16th century for the preparation of "*Aurum potabile*". He investigated the optical properties of gold solutions attributing for the first time the red colour to the colloidal nature of GNPs. At the beginning of the 20th century, the German physicist Gustav Mie rationalized the plasmon resonance absorption of gold colloids using Maxwell's electromagnetic theory. Afterwards, various methods for the preparation of gold colloids were developed. One of the most common synthesis methods
was introduced by Turkevitch *et al*. in 1951: it is a reduction of $HAuCl_4$ by sodium citrate in water which allows the production of 20 nm gold nanoparticle. In 1973, aiming to obtain GNPs of a chosen size, Frens reported the direct correlation of the particle size with the citrate-to-gold ratio. In this way, particles with a size range of 16-147 nm can be obtained by varying the stabilizer/gold ratio[92]. Smaller size particles can be obtained using stronger reducing agents such as sodium borohydride. This reduction strategy was proposed by Brust *et al.* in 1994 and is based on the gold reduction by sodium borohydride in a two phase (water-toluene) system in the presence of an alkanethiol.

Due to their considerable applications in several fields such as optics, catalysis, materials science, nanotechnology, biology and nanomedicine, other methods for gold colloids synthesis have been developed, including seeding-growth procedures, and physical methods, such as sonolysis.

4.6.2. Gold nanoparticle synthesis

Two main approaches are traditionally used in nanotechnology, involving a physical or chemical synthetic strategy respectively.

Top-down methods.

In the "top-down" approach, nanoparticles are produced from larger entities without atomic-level control. Laser ablation is one of the most exploited method for the synthesis of gold colloidal suspensions. This approach consists in the ablation by a laser beam of a gold solid target dipped in water Control on particles size and particles distribution is usually done by modulating the main ablation parameters (duration, wavelength and frequency of laser pulse)

Other physical methods that have been exploited for the control of GNP size are sonochemistry and radiolysis[91].

Bottom up methods.

The "top-down" approach is a chemical self-assembly processes of molecular components in liquid, solid or gas phase. The most widely used methods are based on chemical reduction in solution to yield nanoparticle colloids.

- Turke*vitch method:* this is the most popular method which consists of a single step reduction of tetrachloroauric acid in a boiling aqueous solution by sodium citrate (Scheme 1.). Citrate anions act both as reducing agent and capping agent, preventing particle aggregation by neutralizing surface charge. The average particle diameter can be tuned between 10 – 100 nm with narrow distributions by varying the citrate-to-gold ratio[93,94]. Nanoparticle decoration occurs by citrate displacement by various stabilizing ligands.

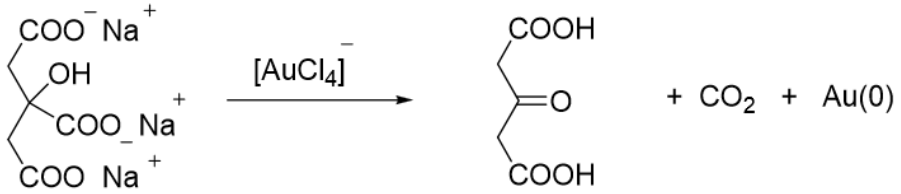

Scheme 1. Turkevitch's reaction of reduction of Au(III) to metal gold, Au(0), by using sodium citrate as a reducing agent.

- *Brust-Schiffrin method:* this synthesis method is used to prepare thermally stable and air-stable GNPs of narrow dispersity and controlled size in non-miscible organic liquids (a two phase system of water-toluene). In detail, tetrachloroaurate is transferred to toluene by tetraoctylammonium bromide (TOAB, the phase transfer catalyst), and is reduced by sodium borohydride in the presence of an alkanethiol which act as stabilizing agent (Scheme x.)[95]. Particle ranging in diameter between 1.5 and 5.2 nm can be produced.

  These alkanethiol-protected GNPs possess higher stability when compared to most other GNPs due to the synergic effect of the strong thiol-gold interactions and van der Waals attractions between the neighboring ligands[96].

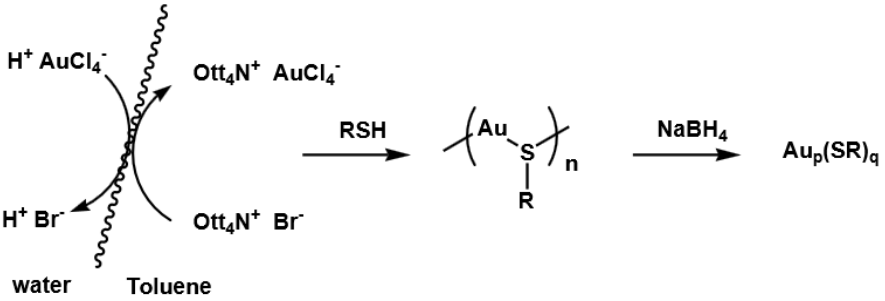

Figure 9. Brust-Schiffrin method for two-phase synthesis of gold nanoparticles.

- *Seed-mediated growth*[97,98]: The seeding-growth procedure is another popular technique which allows to control the size distribution in the range 5-40 nm[91]. Gold nanospheres are synthetized by reduction mediated by a weak reducing agent of Au salt over preformed "seed". A growth solution, prepared by addiction of cetyltrimethylammonium bromide (CTAB, stabiling agent) to a chloroauric solution, is brought to 100 °C. A part, a seed solution is prepared by adding sodium citrated to a chloroauric aqueous solution. Finally, the seed solution is mixed with the growth solution in the presence of ascorbic acid.

  The step-by-step particle enlargement was shown to be more effective than a one-step seeding method to avoid secondary nucleation[91]. Moreover gold nanorods can be easily fabricated by using a variety of different seeds with different sizes and surface functionalities[99].

4.6.3. Physico-chemical properties of colloidal gold

Gold nanoparticles in the size range of 2-100 nm exhibit various size-dependent optical and electronic properties that are significantly different from their bulk counterpart. These specific properties arises from the "size quantum effect", typical of nanosized materials. Irradiation with light in the visible spectra window results in a collective oscillation of electrons known as surface resonance plasmonic band. Any changes to the gold nanoparticle surroundings, such as surface decoration, aggregation, local environment, leads to SPR absorption peak red shifts to longer wavelength, in good agreement with the Mie's theory[100]. This phenomenon is clearly visible by a colorimetric change of the dispersions. SPR bands are characterized by extremely high extinction coefficients, up to 10^{11} $M^{-1}cm^{-1}$, which are much higher than those of organic dyes. Beside the light absorption, which is prevalent in particles smaller than 20 nm, scattering is another peculiar property of particles up to 80 nm. Thanks to all these unique optical features, gold nanoparticles have been exploited in several fields such as biosensing, labeling and biological imaging.

Moreover In virtue of their large surface-to-volume ratio, gold nanoparticles can be largely functionalized with different ligands, such as fluorophores, biomolecules, drugs, oligonucleotides etc., endowing the nanosystem of suitable characteristics for the application in the drug delivery field. Due to their ability to participate in noncovalent and covalent/dative bonding, GNPs can undergo facile surface chemistry[13]. Notably many chemical groups have shown the ability to form stable bonds with gold surfaces. Among those, thiols, disulfides, thioesters, thioethers and isocyanates interact strongly, by a chemisorbing process that spontaneously forms strong and stable Au-S bonds, whereas amino and carboxyl groups bind weakly, comparable to in strength with a hydrogen bond and thus easily displaced.

The reason of this strong affinity is still not completely clear. An explanation may be that as the thiol end of an alkanethiol approaches gold, the Sulphur hydrogen bond becomes weak and hydrogen is released, as shown in (1).

$$(1)\quad R\text{-}SH + Au^0 \rightarrow R\text{-}S^- Au^+ \cdot Au_n^0 + \tfrac{1}{2}\, H_2$$

The thiolate molecule serves as a nucleophile and donates a pair of electrons to the gold surface, which participate to the formation of a strong bond, with strength very

similar to that of a covalent one. The energy estimated for this bond is 45 kcal/mol[13]. Whereby stabilizing polymers and biomolecules are often modified to contain a thiol end-group to enhance their conjugation on the surface of the Au surface.

4.6.4. Gold nanoparticle applications

Gold nanoparticles exhibit distinctive physico-chemical and optical properties, which have been exploited in many fields from electronics to medicine, diagnostics and catalysis. Nanometric size and multiple surface functionalities are the main features of this nano-objects which allow for the wide surface decoration with biomolecules, imaging labels, therapeutic agents and other functionalities for site specific drug and gene delivery and cellular uptake. Gold nanoparticles show several advantages as the the easiness of synthesis, colloidal stability, biocompatibility and the versatility of GNP size (good stability in the range of 2-100 nm), shape (Gold nanorods, Gold nanoshells, Gold nanocages, Gold nanosphere) and surface decoration has provided useful materials for a broad range of biomedical applications. The transport of therapeutic agents to the cells is a critical process especially in the treatment of cancer. GNP therapeutics can be delivered into cells through either passive or active targeting mechanisms. Surface functionalization with specific cancer-markers, such as antigens or receptors whose expression is up-regulated in the tumour, enhance the selective accumulation of the carrier within the disease site. Passive targeting relies on the enhanced permeability and retention (EPR) effect whereby GNPs will accumulate within the tumour via its irregular vasculature, allowing larger particles to pass through the endothelium. Furthermore, decoration of gold nanoparticles with stimuli-responsive materials and targeting ligands provide the unique opportunity to achieve a multimodal targeting arising from both environmental and phenotypical variations. This is reflected into an enhanced therapeutic benefit, while minimizing side effects and decreasing the administration dose. Several nanoformulations for the treatment of cancer are currently undergoing phase II-III clinical trials and few of them have been approved. Aurimmune (Cytimmune Sciences, Rockville, MD) is a 27nm gold nanoparticle coated with thiolated PEG and attached to recombinant human tumor necrosis factor α (TNF-α). It is in clinical trial phase II for the treatment of Head and Neck cancer[101].

Effective targeting strategies have been exploited also for therapeutic applications including genetic regulation, photothermal and sonodynamic therapy. In virtue of their great extinction coefficient, GNPs can strongly absorb light energy which is then converted into thermal energy inducing cell damage and death[102]. In particular, thermoresponsive GNPs can be induced to aggregate in clusters causing a redshift of the absorption band towards near infrared wavelengths (700-1000 nm) which possess remarkable tissue penetration features allowing for the treatment of deep cancer tissues. AuroShell (Nanospectra Bioscience Inc, Houston, Texas) consist of silica nanoparticles coated with a thin layer of gold currently used in clinical trial phase I as enhancer of photothermal therapy of head and neck cancer[101].

Gold nanoparticles are currently being studied for the improvement of sensitivity and resolution of tumour imaging. The high atomic number of gold (Au = 79) enables a high absorption and enhancement of ionizing radiation, as well as superior X-ray attenuation for imaging applications. Other physical characteristics of gold such as surface plasmon resonance and Raman scattering activity have been exploited in non-radiation based cancer applications including optical imaging and photoacoustic tomography of tumours and tumour-specific photothermal therapy agents[103]. Recently decorated gold nanoparticles have been proposed as new NMR chemosensing agents that enable the detection and identification of metabolites in biological fluids. Gold nanoparticles decorated by a monolayer of self-organized receptors allow the binding to the substrates with high selectivity and sensitivity. The interacting molecule appears in the NMR spectrum allowing its detection and recognition[104].

In conclusion, GNPs have emerged as potent tool for the use in bionanotechnology thanks to multiple attributes: the wide range of surface functionality and bioconjugates coupled with the outstanding physical properties of GNPs and controllable release of their cargo make these systems valuable for imaging and drug delivery applications[96]. Moreover, gold nanoparticle synthesis revealed a good reproducibility, high yield and low cost providing homogeneous products: this result enables the scalability of the production. [105]

4.6.5. Nanotoxicity

Although bulk gold is generally accepted as inert and nontoxic, some concerns arise about the biocompatibility of gold nanocolloids due to their deeper penetration and wider systemic distribution.

As showed in many studies reported in literature, cytotoxicity depends on the particle size. GNPs with a size of 1-2 nm revealed necrosis, induction of oxidative stress and mitochondrial damage[106]. In general GNPs with a dimension less than 6 nm show a limited circulation time and renal clearance. However they can efficiently interact with DNA and other key molecules. Larger particles (>6 nm) showed a diminished cytotoxicity because of the diminished binding to DNA, and a prologed systemic circulation thus enhancing accumulation within tumours. Notably 20 nm GNPs decorated with PEG exhibited the lowest clearance and a significantly higher accumulation in the tumour site as direct consequence of the EPR effect. 50 nm GNPs showed a faster internalization rate compared to the other particle sizes and gold nanorods, resulting in a high accumulation in the blood, liver and spleen. Cytotoxicity is also correlated to the GNPs concentration: at low concentration (1 ppm), GNPs in size range of 2-20 nm were found nontoxic to murine macrophage cell line, whereas concentrations higher than 10 ppm induced apoptosis of cells and upregulation of pro-inflammatory genes[106]. Furthermore, the interaction of naked GNPs with plasma proteins determines an increase in the hydrodynamic size. Interestingly, 30 nm particles with protein corona from plasma showed a larger hydrodynamic size in comparison to 50 nm particles.

However, it is essential to distinguish between the toxicity of the GNP core and that one rising from the ligands[91]. Many studies highlight that cationic GNPs are more toxic than anionic particles due to the electrostatic interaction with negatively charged cell membrane[105]. In particular, CTAB-stabilized GNPs were found very toxic as it is a cationic surfactant that can break open cell membranes[105,106]. GNP cytotoxicity can be reduced by PEGylation (coating with polyethylene glycol) that is a well-known material able to reduce nonspecific binding of biological molecules to surfaces and provide stealthness to the nanosystem.

Furthermore, it is important to differentiate between cytotoxicity and cellular damage. In fact, particles that show negligible cytotoxicity via several standard assays may be still able to cause serious cellular damage. It is reported that 13 nm citrate-

capped GNPs showed no relevant cytoxicity according to an assay, but were able to promote the formation of abnormal actin filaments, which led to decreases in cell proliferation, adhesion, and motility[107]. Cytotoxicity also depends on the type of cells used. Finally, GNP cytotoxicity may also depend on the cell lines[91,105].

Concerning the in *vivo* distribution of GNPs, size, surface charge and surface hydrophobicity are crucial features. The presence of biocompatible amphiphilic chains on GNP surface reduced the recognition by macrophages, thus prolonging the circulation time in blood. The biological distribution of various sizes (15, 50, 100 and 200 nm) of GNPs on intravenous administration in mice was investigated and revealed that GNPs of all sizes were mainly accumulated in liver, lung and spleen, whereas accumulation in various tissues depended on GNP size. Notably, 15 nm and 50 nm GNPs spread in all tissues, whereas small amount of 200 nm GNPs were found in blood, brain, stomach and pancreas[91].

4.7. RAFT POLYMERIZATION

Reversible Addition Fragmentation chain Transfer (RAFT) polymerization is one of the most versatile methods for conferring living characteristics on radical polymerizations[108]. This technique was first reported in 1970s but the process was irreversible, so the transfer reagents could not be used to control radical polymerization at this time. Scientists began to realize the potential of RAFT in controlled radical polymerization in the 1980s. RAFT technology can be used to synthesize polymers with predetermined molecular weight, narrow polydispersity index (M_w/M_n) and defined architecture obtaining linear block copolymers, random copolymers, and other complex architectures. RAFT process allows to obtain high monomer conversion and polymerization rate. Moreover, polymerization can be performed in a wide range of monomers, initiators, solvent and heterogeneous media (emulsion, suspension).

It involves the use of Chain Transfer Agent (CTA), known as RAFT agent, to afford control over the generated molecular weight, polydispersity, chemical composition and rate of the reaction. The most commonly used CTA are thiocarbonylthio compounds (Figure 10.).

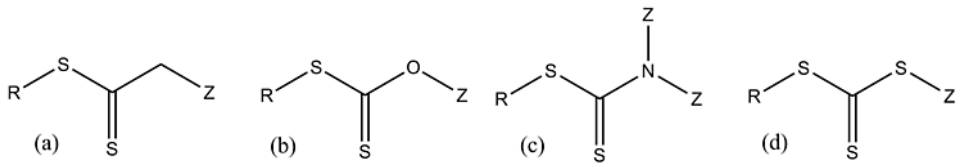

Figure 10. Chemical structure of representative RAFT agents: (a) dithiocarbonate, (b) xanthate, (c) dithiocarbamate and (d) trithiocarbonate.

The efficiency of the RAFT agents is dictated by the substituents R and Z. Notably Z-group (aryl or alkyl group) controls the reactivity of the C=S bond towards radical addition and influences the stability of the intermediate radicals. R is the free radical leaving group: it undergoes a scission from the RAFT-adduct radical and the generated radical must be able to reinitiate the polymerization. R group must give better homolytic cleavage from the RAFT agent in comparison with the growing polymeric chain and give efficient re-initiating species towards the monomer used.
The mechanism of the RAFT polymerization is shown in Figure 11.
At the start of the process (Initiation) a radical species $I^{\bullet}$ is generated from a suitable initiator. Initiators are usually azo-compounds, such as azobisisobutyronitrile (AIBN), which decomposes and releases a molecule of nitrogen and two radicals (2 $I^{\bullet}$). $I^{\bullet}$ reacts with a monomer forming a propagating radical species ($P_n^{\bullet}$). The propagating chain then adds to the RAFT agent generating into a polymeric thiocarbonyl derivative. R-group is released which will reinitiate the polymerization (Reinitiation).

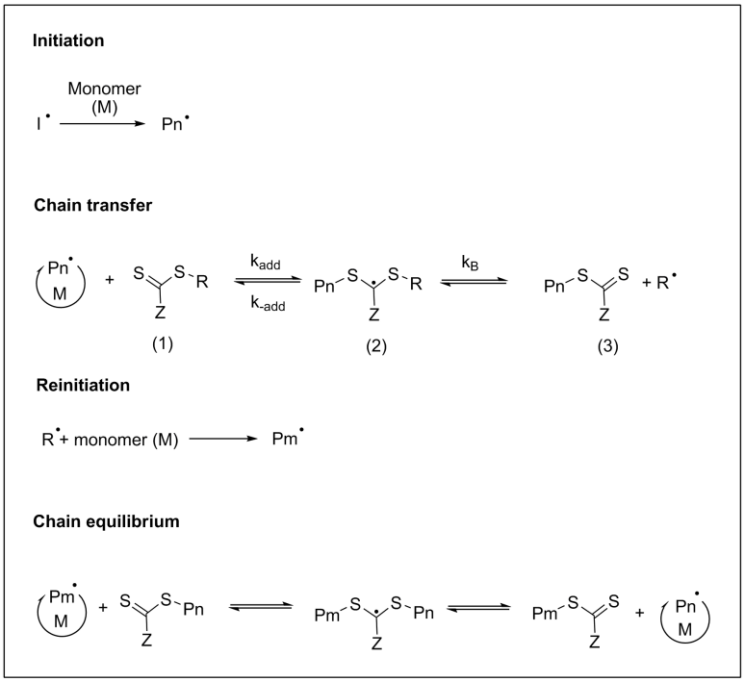

Figure 11. Mechanism of RAFT polymerization. A radical initiator, I$^{\bullet}$, reacts with a single monomer molecule (M) to yield a propagating polymeric radical, which subsequently react with other monomer to form a longer propagating chain (Pn$^{\bullet}$). A polymeric radical reacts with the RAFT agent to form a radical RAFT adduct, and fragmentation may occur, releasing a radical (R$^{\bullet}$) and a polymeric RAFT agent. This step of the reaction is reversible. The radical R▪ can reinitiate another polymerization process. The main RAFT equilibrium consists of steps of RAFT adduct formation and fragmentation, until a bi-radical termination ends the growing chain.

The key step in the RAFT polymerization process is the establishment of equilibrium the growing chains and the dormant poly-RAFT agent species.

To achieve control over polymerization it is required that the dormant species concentration is favored than that of the active one but in rapid exchange with one another. In this way the radical-radical termination is minimized and the resulting chains grow homogeneously, with narrow, unimodal molecular mass distributions and low polydispersity index. Termination may occur when living chains react in a process known as a bi-radical termination, which leads to a dead polymer. Ideally, the RAFT adduct is sufficiently hindered such that it does not undergo termination reactions. The total number of radical chains formed is determined by the initial amount of radicals, which depends by the amount of initiator, while the number of polymer chains elongation is mainly controlled by the RAFT agent.

At the end of the polymerization reaction, most of the chains retains the thiocarbonyl group at the end. In light of this polymers with defined end-groups can be synthetized[98].

5. MATERIALS AND METHODS

5.1. REAGENTS

- Folic acid, sodium citrate tribasic dihydrate, tetrachloroauric(III) acid trihydrate, iodine, potassium iodine, barium chloride, sodium hydroxide, hydrochloridric acid, dimethyl sulfoxide, tris(2-carboxyethyl)phosphine hydrochloride (TCEP), triethylamine, azobisisobutyronitrile (AIBN), sodiumhydroxide (NaOH), oxalyl chloride, glycidyl methacrylate, magnesium sulfate, N,N dimethylamino pyridine (DMAP), dimethyl formamide anhydrous (DMF), dimethylsulfoxide anhydrous (DMSO), chloroform, dichloromethane (DCM), ethyl acetate (EtOAc), methanol (MeOH), diethyl ether (Et_2O), petroleum ether (b.p. 40-60 °C), (3-(4,5-dimethylthiazol-2-yl)-2,5-diphenyltetrazolium bromide) were purchased from Sigma-Aldrich (St. Louis, MO, USA) and Alfa Aesar companies.
- Cysteine, N-iydroxysuccinimide (NHS), N,N'-Dicyclohexylcarbodiimide and 5,5'-di-thiobis-(2-nitrobenzoic acid) (DTNB) were purchased from Fluka (Buchs, Switzerland).
- Sephadex G-25 and sephadex LH 20 gel filtration resins were obtained from Amersham Pharmacia Biotech (Uppsala, Sweden).
- Amino-mercapto PEG 2 kDa and 3.5 kDa, methoxy-mercapto poly PEG 2kDa were purchased from Iris Biotech GmbH (Marktredwitz, Germany).
- Carboxytetramethylrhodamine (Rhodamine NHS) was purchased from Thermo Fisher Scientific (Waltham, MA, USA).
- Bodipy FL NHS was purchased from Lumiprobe GmbH (Hannover, Germany)
- All the chemical reagents for cell culture, Dulbecco's modified Eagle's medium (DMEM) and folic acid free DMEM, RPMI-1640 medium, L-Glutamine solution, D-(+)-Glucose solution, sodium bicarbonate solution, fetal bovine serum (FBS), penicillin-streptomycin solution, Trypan Blue solution, fibronectin and trypsin were supplied by Sigma-Aldrich (St. Louis, MO, USA).

- Analytical thin-layer chromatography (TLC) was carried out on glass sheets coated with silica gel (Merck F-254, Merck, Darmstadt, Germany)
- KB (human epithelial cervix carcinoma cell line) and MCF7 (human breast adenocarcinoma cell line) cells were obtained from the American Type. Culture Collection.
- Water for the preparation of all suspensions and solutions was "ultrapure" water (milliQ-grade, 0.06 μSiemens cm-1) produced with the Millipore Milli-Q purification system (MA, USA).
- Salts and buffers were purchased from Fluka Analytical (Buchs SG, Switzerland) and Sigma-Aldrich (St. Louis, MO, USA).

5.2. INSTRUMENTATION

- Spectrophotometric analysis were carried out with an UV-Vis λ25 Perkin Elmer spectrophotometer (Norworlk, CT, USA)
- Multiwell plate detections were carried out with Microplate Autoreader purchased from Biotek Instruments inc., mod. EL311SK (Highland, Vermont U.S.A.).
- HPLC system Jasco, equipped with two pumps PU-2080 Plus, a detector UV-2075 Plus and Hercule 200 JMBS, and analytic column Luna (C18, 5 μ, 300 Å, 250 x 4.6 mm) from Phenomenex (Torrance, U.S.A.) was used for reverse phase chromatographic analysis (RP-HPLC).
- Sample vials were kept stirring with Rotating stirrer, MOD 708 (ASAL S.r.l.) and Heto Mastermix.
- Lyophilization was carried out with freeze-dryier Hetossic HETO Lab Equipment (Birkerod, Denmark).
- Solvents were evaporated with Rotavapor R114 of BÜCHI Labortechnik AG (Postfach, Switzerland).
- pH measurements were carried out with a pH-meter Seven Easy 20-K Mettler Toledo with a Mettler Toledo Inlab 413 electrode (Schwerzenbach, Switzerland) and with a 744 pH Meter - Metrohm (Herisau, Switzerland)
- The buffers were filtered with Millipore Systems using a 0.22 μm cellulose acetate filter.

- The samples were centrifugated with a Sigma 1-14 Microfuge (Celbio Spa) and on a Centrikon T-42K, Kontron Instruments, Eching, Germany.
- Dynamic Light Scattering measurements were performed by Zetasizer NanoZS (Malvern instruments Ltd, UK).
- TEM images were obtained with a Tecnai G2 (FEI, Oregon, USA). Samples were placed on copper grid, the excess was removed with filter paper and then stained with uranyl acetate (1% in deionized water). Particle size analysis were performed with ImageJ Software (developed at the National Institute of Health, USA).
- Polymerizations were carried out using standard Schlenk techniques under a nitrogen atmosphere. Thin layer chromatography (TLC) was performed using pre-coated plates (silica gel 60 ALUGRAM SIL G/UV254) and eluted in the solvent system indicated. Compounds were visualized by using UV light (254 nm) or stained with a basic solution (10% w/w $K2CO_3$ in water) of KMnO4. Across Organic 60 Å (0.035-0.070 mm) silica gel was used for column chromatography.
- ^{1}H and ^{13}C NMR spectra were recorded on a Bruker DPX400 Ultrashield spectrometer and Bruker Spectrospin AMX 300 MHz (Fallanden, Switzerland). All NMR data were processed using MestreNova 6.2.1 Software.
- Biological studies were carried out in biological safety cabinet Space, cells were grown using the incubator from PBI International and imaged with optical microscope Axiovert 40CFL Zeiss.
- Fluorimetry analyses were performed using a LS 50 B Perkin-Elmer fluorimeter (Norworlk, CT, USA).
- Flow cytometric analyses were performed using a BD FACSDiva flow cytometer (Becton, Dickinson and Company, Buccinasco, Milan) and results were processed with BD FACSDiva Software.
- Confocal microscopy images were obtained using a Leica TCS SP5 confocal laser-scanning microscope equipped with a 488 nm Ar laser, 543/633 nm HeNe laser, 100 × 1.4 NA or 40x 1.4 NA objectives using a Leica Type F immersion oil - Leica Microsystems GmbH (Wetzlar, Germany). Image quantification and elaboration was performed using ImageJ Software (developed at the National Institute of Health, USA).

5.3. ANALYTICAL METHODS

5.3.1. Iodine assay for quantitative and qualitative evaluation of polyethylene glycol

"Iodine assay" is a colorimetric test originally described by Sims and Snape[109], which allows to assess the polyethylene glycol (PEG) concentration in an aqueous solution. The test is performed by using two reagent solutions: Barium chloride (5% m/v in 1M HCl) and Iodine (1.27 g di I_2 in 100 mL of a 2% w/v KI solution) solutions. PEG forms a complex with Barium Iodine that absorbs light at 535 nm.

Solutions of PEG to be quantified in milliQ water (1 mL) were added of 250 µL of a Barium chloride solution and 250 µL of a Iodine solution. The Blank sample was prepared as described above by replacing the PEG solution volume with milliQ water. The samples were incubated in the dark for 15 minutes at room temperature, and then analyzed spectrophotometrically at 535 nm.

The PEG concentration was derived from a calibration curve previously prepared in the concentration range 0-10 µg/mL, from serial dilutions (in triplicate) of a 5 mg/mL stock solution of $mPEG_{5kDa}$ in milliQ water (Figure 12).

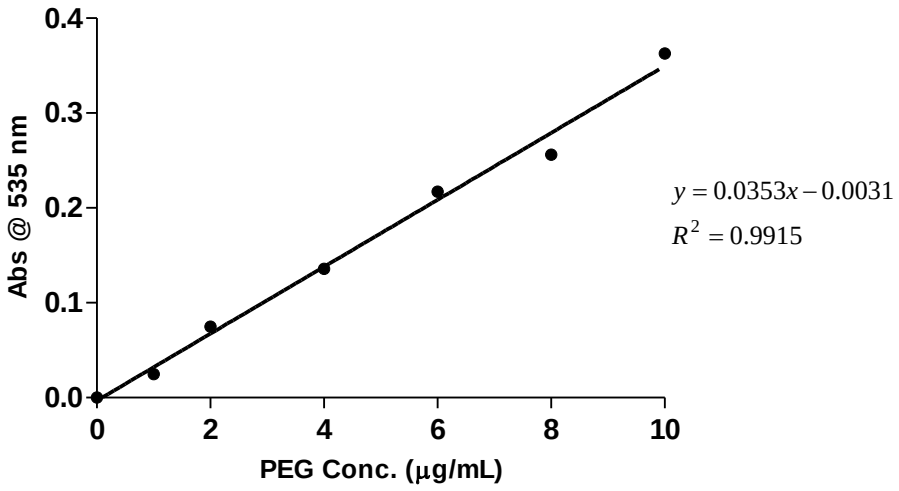

Figure 12. Calibration curve of PEG obtained with Iodine assay. Optical density was measured at 535 nm.

5.3.2. Calibration curve for the block copolymer poly(MCH-co-GMA)

The quantitative assessment of the pH sensitive copolymer poly(MCH-co-GMA) was carried out by UV-Vis spectroscopy. The UV-Vis analysis of a poly(MCH-co-GMA) solution in NaOH 0.1 N showed a bell-shaped profile with a maximum absorption peak at 300 nm.

In light of this, a calibration curve was prepared as follows. Five mg of poly(MCH-co-GMA) were precisely weighed and dissolved in 1 mL of NaOH 0.1 M to generate a stock solution. Serial dilutions were then prepared from the stock solution in the range 0-80 μg/mL (in triplicate). The optical density of each solution was measured at 300 nm and plotted versus the concentration to obtain the calibration curve (Figure 13).

Polymer solutions with unknown concentration were suitably diluted in NaOH 0.1 N and analyzed as described above.

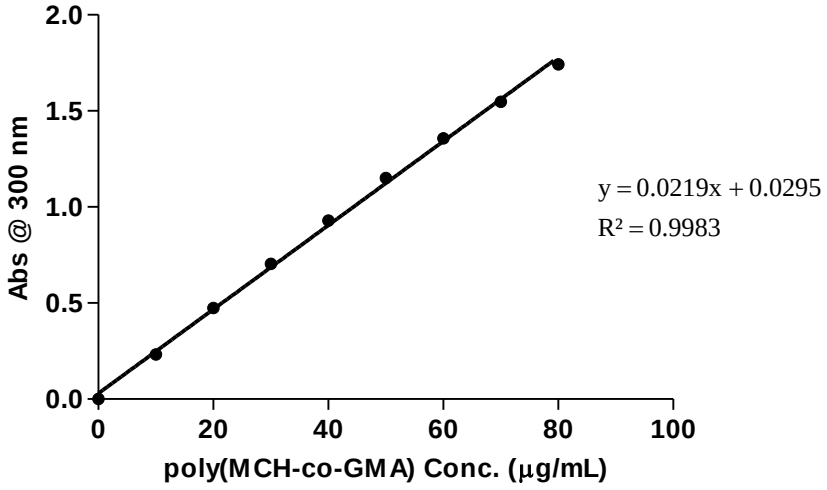

Figure 13. Calibration curve of poly (MCH-co-GMA) in NaOH 0.1 N obtained by UV-Vis analysis at 300 nm.

5.3.3. Ellman's assay for quantitative analysis of thiol groups

Ellman's reagent (5,5'-dithiobis-(2-nitrobenzoic acid) - DTNB) is a chemical used to quantify the concentration of thiol groups in a sample solution. It possesses a disulphide bond which reacts stoichiometrically with free thiol groups. The reaction with thiols implies the cleavage of the disulphide to yield 2-nitro-5-thiobenzoate

(TNB^-) which ionizes to the TNB^{2-} dianion in water at neutral and alkaline pH. TNB^{2-} shows an UV-Vis absorption band at 412 nm[110,111].

This assay was exploited to evaluate the ratio of free thiol groups of the polymeric derivatives after synthesis and purification. A calibration curve was prepared using dilutions of cysteine.

Cysteine (2 mg, 16.5 μmol) was dissolved in 1 mL of freshly prepared 0.1 M PBS added of 1 mM EDTA at pH 8. Dilutions from 10 to 200 μM were prepared in the same buffer and plated into a 96-well plate (100 μL/well). A 10.1 mM DNTB solution in 0.1 M PBS added of 1 mM EDTA at pH 8 was prepared and 30 μL of this solution were added to the cysteine dilutions. Blank sample was prepared by replacing the cysteine volume with the dilution buffer. All the samples were incubated for 30 minutes at room temperature and then optical density was measured at 405 nm.

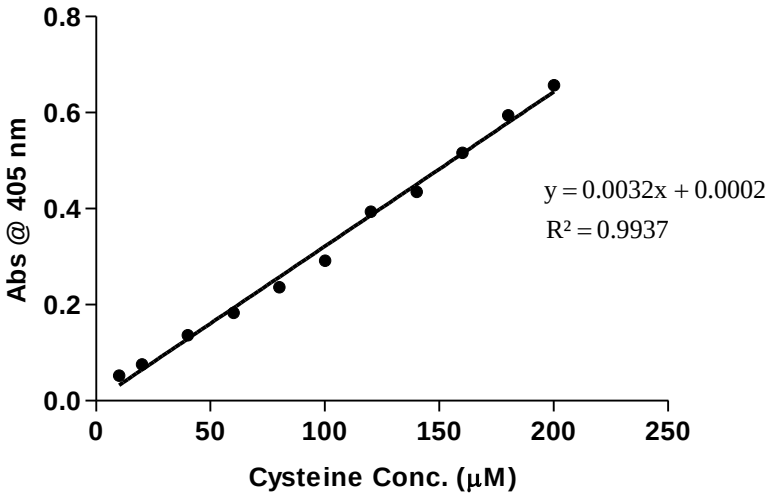

Figure 14. Calibration curve for the Ellman's assay; optical density was measured at 405 nm.

The polymer solutions of unknown thiol concentration were analyzed as described above and the thiol concentration was derived from the calibration curve of Figure 14.

5.3.4. Bicinchoninic acid (BCA) Test for cell countig

BCA test is a colorimetric assay developed by Paul K. Smith[112] which enable to assess the total concentration of proteins in a solution. At alkaline pH, in the presence of specific aminoacids of the peptide sequence (cysteine, cystine, tyrosine, and tryptophan), Cu^{2+} ions are reduced to Cu^+. Afterwards, two molecules of BCA chelate

each Cu^{+} ion, forming a purple-colored complex that strongly absorbs light at a wavelength of 570 nm.

The concentration of proteins on cell lysates was determined by a calibration curve generated according to the following procedure. Serial dilutions of a cell lysate obtained from cell suspension at known cell concentration were plated into a 96 well-plate (100 µL). 200 µL of BCA reagent (50 parts of Bicinchoninic acid and 1 part of Copper sulfate (II)) were added to each well. The plate was incubated for 30 minutes at 37 °C and then was read at 570 nm by a UV-Vis Microplate Autoreader.

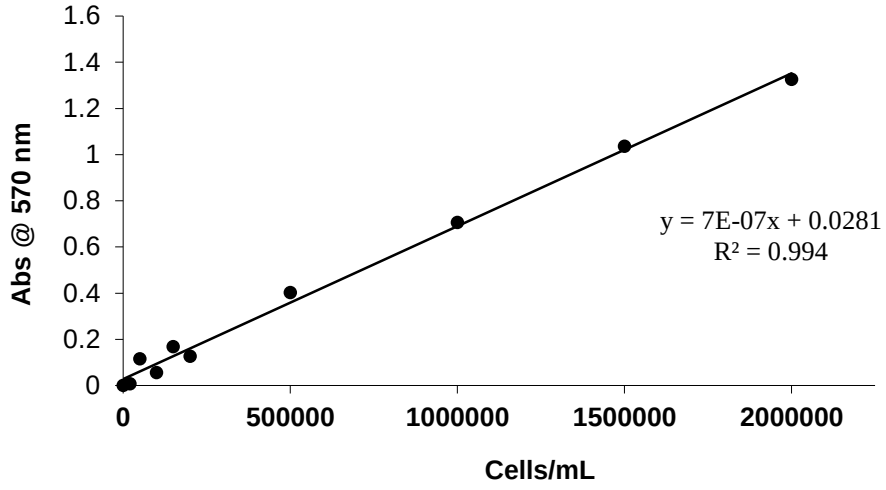

Figure 15. BCA Calibration curve obtained from cell lysates.

5.4. SYNTHESIS OF POLYMERS

5.4.1. Synthesis of Lipoic terminating CTA

The Lipoic terminating chain transfer agent (CTA) was synthetized by a dual step procedure. The carboxylic group was activated to acyl chloride as described in literature[113,114] and then conjugated to tetraethylenglycole.

Lipoic acid (1 g, 4.85 mmol) was dissolved in anhydrous DCM (5 mL) and the solution was cooled into an ice bath. Oxalyl chloride (0.61 g, 4.85 mmol) was added dropwise to the reaction mixture using a dropping funnel. The reaction vessel was sealed with a glass stopper and the reaction was left under stirring for 4 hours at 0 °C. The volume of the reaction mixture was reduced under *vaccum*. The residue was redissolved in anhydrous DCM (5 mL) and the organic solvent removed in *vacuum* to remove the final traces of oxalyl chloride[115].

Traces of water were removed from tetraethyleneglycole (TEG) (9.42 g, 48.5 mmol) by azeotropic distillation with toluene under reduced pressure. TEG was then dissolved in anhydrous DCM (5 mL) in the presence of triethylamine (0.77 g, 7.63 mmol). Acylchloride activated Lipoic acid was dissolved in 4 mL of anhydrous DCM and added dropwise to the tetraethylenglycole solution and the mixture was left overnight at room temperature under stirring. Afterwards the solvent was removed under reduced pressure to yield the crude product mixture as brown oil, which was further purified by column chromatography on silica gel using elute with 4:1 (v/v) diethyl ether/ethyl acetate mixture. The conjugate Lipoic-TEG was obtained as viscous yellow oil that was used for the next synthetic step (0.39 g, 1.03 mmol, 22 % of yield).

Lipoic acid-TEG (0.23 g, 0.60 mmol) and 4-cyano-4-(phenylcarbonothioylthio) pentanoic acid (0.17 g, 0.60 mmol) were dissolved in anhydrous DCM (2 mL) and the mixture was cooled in an ice bath. Separately, DCC (0.15 g, 0.72 mmol) and DMAP (3.66 mg, 0.03 mmol) were solved in anhydrous DCM (1 mL) and added dropwise to the solution. The mixture was stirred for 48 hours. The purification was performed by chromatography on silica gel (Petroleum ether/Ethyl acetate v/v 4:1) which yielded the pure product as a red oil: 0.16 g (42 % of yield).

5.4.2. Synthesis of poly(MCH) macro-CTA

MHC was synthesized as reported before[116]. MCH (1.5 g, 5.28 mmol), Lipoical CTA (77.2 mg, 0.12 mmol) and AIBN (20 mg, 0.05 mmol) were dissolved in anhydrous DMF (9 mL) in a Schlenk tube. After deoxygenation by nitrogen bubbling for 30 minutes, the resulting mixture was thermostated in an oil bath at 70°C. The polymerization was monitored by regular withdrawal of samples analyzed by ^{1}H NMR in DMSO-d_6. The monomer conversion was calculated following the formation of a new broad peak at 6.9 ppm deriving from the shift of the MCH aromatic protons (originally at 7.08 ppm in the monomer) throughout the polymer formation.
At 70 % of conversion (DP=26) the polymerization was stopped by exposing the reaction mixture to the air. The polymer was recovered by precipitation in 1:1 (v/v) diethyl ether/petroleum ether, redissolved in DCM and precipitated again in the same

solvent mixture. After filtration, the organic solvent residues were removed under reduced pressure obtaining 730 mg of a pink precipitate (0.091 mmol, 49 % of yield).

5.4.3. Synthesis of glycerol methacrylate (GMA)

Glycidyl methacrylate (23.1 g, 0.16 mol, 21.5 mL) was dissolved in distilled water (487 mL) and sulfuric acid (0.5 equivalents) was added dropwise. The reaction was carried out under stirring at room temperature for 2 hours. The glycerol methacrylate (GMA) generated from the reaction was isolated by extraction with dichloromethane (DCM – 200 mL x 3), washed with brine, dried over anhydrous magnesium sulfate ($MgSO_4$) and then concentrated under vacuum.
The GMA monomer was purified by flash chromatography on silica gel using a 1:1 v/v DCM/EtAcO mixture. The pure product (14.8 g, 0.09 mol, 57 % of yield) was characterized by ^{1}H NMR in DMSO-d_6 and ESI-TOF mass spectrometry.

5.4.4. Synthesis of poly(MCH-co-GMA)

Poly(MCH) (0.619 g, 77.1 μmol), GMA (0.815 g, 5.01 mmol) and AIBN (6.3 mg, 38.5 μmol) were solved in anhydrous DMF (9 mL) in a Schlenk tube. The solution was degassed by nitrogen bubbling for 30 minutes and then placed inside of an oil bath thermostated at 70 °C. The polymerization progress was checked by ^{1}H NMR in DMSO-d_6 at scheduled times. The polymerization was stopped at 81 % of conversion (DP=53) by lifting the Schlenk tube and exposing the reaction mixture to the air. The conversion of monomer to polymer was determined by ^{1}H NMR spectroscopy in DMSO-d_6 of reaction samples and looking at the decrease of vinylic proton integrals (5.74 and 6.13 ppm) referred to the DMF peak (2.97 ppm) used as solvent for the polymerization. Finally, the polymer was isolated by precipitation in a 1:1 v/v diethylether/petroleum ether mixture, dissolved in methanol and precipitated again in the same solvent mixture. The precipitate was dried under *vacuum* and 1.01 g was recovered (60.9 μmol, 79 % of yield).

5.4.5. Synthesis of poly(GMA)

GMA (1.28 g, 7.99 mmol), Lipoical RAFT agent (51.90 mg, 80.70 μmol) and AIBN (6.62 mg, 40.35 μmol) were dissolved in anhydrous DMF into Schlenk tube and deoxygenated by N_2 bubbling for 30 minutes. Then the Schlenk tube was dipped into a thermostated oil bath at 70 °C to trigger the polymerization reaction. The reaction kinetic was monitored by ^{1}H NMR in DMSO-d_6. The polymerization degree was calculated by monitoring the decrease of the integrals of the monomer vinyl signals (6.11 and 5.58 ppm) using the singlet at 7.95 ppm of the DMF as reference. At 80% of conversion, the polymerization was stopped by exposing the reaction mixture to the air. The polymer was isolated by precipitation in a 1:1 v/v diethyl ether/petroleum ether mixture, redissolved in methanol and precipitated again in the same solvent mixture. The precipitate was dried under reduced pressure and 0.986 g was recovered (74.20 μmol, 92 % of yield).

5.4.6. Removal of Thiocarbonylthio Group

The removal of thiocarbonylthio end groups from polymers generated by RAFT polymerization was performed according to the method reported by Perrier *et al.*[117]. Typical reaction conditions described below were applied to each of the polymers synthetized by RAFT polymerization.

Poly(GMA) (0.986 g, 74.20 μmol) and AIBN (0.366 g, 2.23 mmol) were dissolved in anhydrous DMF (1:30 polymer:AIBN molar ratio) and dipped in a thermostated oil bath at 80 °C. After 4 hours the reaction mixture was precipitated dropwise in a 1:1 v/v Et_2O/petroleum ether mixture and desiccated under reduced pressure (0.940 g, 71.23 μmol, 96 % of yield).

5.4.7. Turbidimetric analysis of poly(MCH-co-GMA)

1.0 mg/mL poly(MCH-co-GMA) solution in deionized water was prepared and the pH was adjusted to pH 12 by addiction of 1 N NaOH. The solution was sequentially added of 10 μL aliquots of 1 N HCl until pH 3.0 was achieved. The spectrophotometric transmittance at 500 nm was plotted versus the pH. The relative transmittance was calculated referring to the transmittance at pH 12 (100%).

5.4.8. Potentiometric titration of poly(MCH-co-GMA) copolymer

Poly(MCH-co-GMA) (10 mg, 0.61 μmol) were dissolved in deionized water (10 mL) and the pH was brought to 12 with 1 N NaOH. Potentiometric titration was carried out by addition of 2 μL aliquots of HCl 1 N under stirring over a pH range of 12 to 3. The back titration was started from the pH 3 by addition of 2 μL aliquots of NaOH 1 N until pH 12 was achieved. pH variations were plotted the total volume of titrant obtaining two overlapping sigmoidal profiles. The apparent pKa was calculated as the median of the equivalence points of each curve.

5.4.9. Synthesis of Folate-PEG$_{3.5kDa}$-SH (FA-PEG$_{3.5\ kDa}$-SH) and Folate-PEG$_{2\ kDa}$-SH (FA-PEG$_{2kDa}$-SH)

Folic acid (50.0 mg, 0.113 mmol) was dissolved in 1 mL of anhydrous DMSO. N-hydroxysuccinimide (NHS - 15.6 mg, 0.136 mmol) was added to the solution, followed by dicyclohexylcarbodiimide (DCC - 28.1 mg, 0.136 mmol). The mixture was stirred overnight in the dark and then filtered to remove the insoluble byproduct, dicyclohexylurea. The N-Hydroxysuccinimidyl-ester-activated folic acid product was isolated by precipitation in diethyl ether and dried under reduced pressure. N-hydroxysuccinimidyl-ester-activated folic acid (25 mg, 0.046 mmol) and NH_2-PEG$_{3.5kDa}$-SH (54.1 mg, 0.015 mmol) were dissolved in 1 mL of anhydrous DMSO added of triethylamine (1.51 mg, 0.015 mmol) as catalyst. The reaction mixture was stirred for 12 h at room temperature in the dark and then added dropwise in diethyl ether (40 mL). The precipitate was recovered by centrifugation and dried under *vacuum*. The crude product FA-PEG$_{3.5kDa}$-SH was purified from the excess of folic acid by size exclusion chromatography using a Sephadex G-25 resin run with ammonia solution (pH 9) as mobile phase. The column fractions were tested by UV-Vis spectroscopy at 363 nm and Iodine test[109] to assess the presence of Folate and PEG respectively. The positive fractions to both colorimetric assays were collected and freeze-dried.

The regeneration of the thiol end-group of conjugate FA-PEG$_{3.5kDa}$-SH was performed in 50 mM acetate buffer pH 5 in the presence of Tris(2-carboxyethyl)phosphine (TCEP) as reducing agent. FA-PEG$_{3.5kDa}$-SH (20 mg, 8.2 μmoles) and TCEP (20.5 mg, 82 μmoles) were dissolved in acetate buffer and left under stirring for 3 hours. The

mixture was then purified by dialysis against 1 mM HCL, 1 mM EDTA for 2 days (Spectra/Por Float-a-lyzer G2, MWCO =0.5-1 kDa) and freeze-dried. The final product FA–$PEG_{3.5kDa}$-SH was dissolved in phosphate buffer at pH 7.4 and analyzed by UV-Vis spectroscopy at 363 nm (ε_{363}= 6.197 M^{-1} cm^{-1}), Iodine test to assess the conjugation efficiency and by Ellman assay[111] to assess the percentage of free thiol groups. FA–$PEG_{3.5kDa}$-SH was characterized by MALDI mass analysis to assess the identity and the purity of the product, and by RP-HPLC to quantify folic acid traces. The system was equipped with a RP-C18 column eluted with 10 mM ammonium acetate buffer, pH 6.5 (eluent A) and acetonitrile (eluent B), in a gradient mode from 10 to 40% of eluent B in 40 minutes using a UV detector set to 363 nm. No traces of free folate were detected in the chromatogram confirming the purity of the product.

The same synthetic and characterization procedures were used for the production of Folate-PEG_{2kDa}-SH using a NH_2-PEG_{2kDa}-SH instead of NH_2-$PEG_{3.5kDa}$-SH.

5.4.10. Synthesis of the fluorescent label Rhodamine-PEG-SH (Rho-PEG_{2kDa}-SH)

Rhodamine-NHS (25 mg, 47.3 µmol) was dissolved in anhydrous DMSO (500 µL) under stirring and added of NH_2-PEG_{2kDa} -SH (78.9 mg, 39.4 µmol) in the presence of triethylamine (3.99 mg, 39.4 µmol). The reaction was carried out overnight under stirring at room temperature in the dark. The reaction mixture was purified by size-exclusion chromatography using Sephadex LH 20 resin and ethanol as eluent. The column fractions were collected and analyzed by UV-Vis spectroscopy at 552 nm and Iodine test (535 nm) for Rhodamine and PEG determination, respectively. Fractions positive to all tests were pooled and the solvent evaporated under reduced pressure. The obtained residue was dissolved in water at pH 6 obtained by adding HCl and freeze-dried. The lyophilized pink powder was dissolved in water and the optical density was measured at 552 nm to derive the Rhodamine content referring to a calibration curve, while the concentration of PEG was assessed by Iodine test. The conjugation yield refered as Rhodamine/PEG molar ratio was shown to be of 96%.

In order to regenerate the thiol groups of the conjugate, which might be oxidized after purification, Rhodamine–PEG_{2kDa}-SH (20 mg, 8.28 µmol) was dissolved in 1 mL of 50 mM acetate buffer pH 5. Tris(2-carboxyethyl)phosphine (TCEP, 20.73 mg, 82.85 µmoles) was added to the solution and the reaction was carried out for 3 hours under rotational stirring at room temperature. The polymer was then purified from the

excess of TCEP by dialysis for 24 h against 0.5 mM HCl using a dialysis membrane with a MWCO of 1000 Da. The product was lyophilized and characterized by MALDI-TOF mass analysis.

5.4.11. Synthesis of Folate-Cadaverine-Rhodamine (FA-C_5-Rho)

The conjugate FA-C_5-Rho was synthetized by a three step procedure.

I. *Activation of Folic acid to N-Hydroxysuccinimidyl-ester:* folic acid was activated as NHS-ester according to the procedure reported in Chapter 5.4.9.

II. *N-Hydroxysuccinimidyl-ester-activated Folic acid conjugation to Cadaverine:* Cadaverine (C_5 -130.5 mg, 1.28 mmol) was dispersed in 150 µL of anhydrous DMSO. N-Hydroxysuccinimidyl-ester-activated Folic acid (FA-NHS - 23.0 mg, 0.04 mmol) was dissolved in anhydrous DMSO (1 mL) in the presence of triethylamine (TEA – 178.1 µL, 1.28 mmol) and added dropwise to the Cadaverine solution. The reaction was performed overnight under stirring at room temperature in the dark. The reaction mixture was added dropwise to 40 mL of Et_2O in order to remove the excess of Cadaverine that, on the contrary of folic acid, is soluble in Et_2O. The precipitated Folate-Cadaverine conjugate was washed with Et_2O (3 x 40 mL) and then dried under vacuum.

III. *Rhodamine-NHS conjugation to Folate-Cadaverine:* Folate-Cadaverine (16.6 mg, 31.56 µmol) was dissolved in anhydrous DMSO (1 mL) and added of TEA (3.83 mg, 37.88 µmol). 700 µL of a 54.1 mM Rhodamine-NHS solution in anhydrous DMSO were added dropwise to the Folate-Cadaverine solution. The reaction was left overnight under stirring at room temperature in the dark. The crude product was recovered by precipitation in Et_2O and the precipitate was redissolved in 500 µL of DMSO. The unreacted Rhodamine was removed by size exclusion chromatography using a Sephadex LH20 resin eluted in ethanol. The fractions containing the product FA-C_5-Rho were pooled and treated under reduced pressure to remove the solvent. The residue was dissolved in milliQ water and lyophilized obtaining a pink powder (18.2 mg, 19.4 µmol, 61 % of yield) that was characterized by ESI-TOF mass analysis and ^{1}H-NMR.

5.4.12. Synthesis of Bodipy FL-PEG-SH (Bdp-PEG$_{2\ kDa}$-SH)

Bodipy FL-NHS (14.6 mg, 37.6 μmol) was dissolved in anhydrous DMSO (400 μL) under stirring and added of NH_2-PEG_{2kDa}-SH (62.7 mg, 31.3 μmol) in the presence of triethylamine (4.4 μL, 31.3 μmol). The reaction was carried out overnight under stirring conditions at room temperature in the dark. The mixture was purified by size-exclusion chromatography using Sephadex LH 20 resin and ethanol as eluent. The column fractions were collected and analyzed by UV-Vis spectroscopy at 503 nm and Iodine test (535 nm) for Bodipy FL and PEG assessment, respectively. Fractions positive to both tests were pooled and the solvent removed under reduced pressure. The resulting yellow oil was dissolved in water added of HCl to a final pH 6 and freeze-dried. The lyophilized product was analyzed by UV-Vis spectroscopy at 503 nm (ε_{503}= 80000 $L \cdot mol^{-1} \cdot cm^{-1}$, as reported by the manufacturer) and tested by Iodine assay for the determination of Bodipy FL and PEG concentration, respectively. The conjugation yield expressed as Bodipy FL/PEG molar ratio was shown to be 94%.

5.5. GOLD NANOPARTICLE PRODUCTION, SURFACE DECORATION AND CHARACTERIZATION

5.5.1. Synthesis of gold nanoparticles (GNPs)

Preparation of gold nanoparticles was performed following the Turkevich method[94] using sodium citrate as reducing and capping agent. All the glassware was widely washed with aqua regia (3:1 v/v of [12.2 M Hydrochloric acid] : [14.6 M Nitric acid]) and then rinsed with deionized water. 0.25 mM tetrachloroauric solution in milliQ water (100 mL) was prepared and heated up to 75 °C under stirring. Trisodium citrate dihydrate (100 mg) was dissolved in milliQ water (0.34 M) and 3 mL of this solution were added dropwise to the $HAuCl_4$ solution. The mixture was left under stirring for 1 hour at 75 °C. Then, the colloidal suspension was cooled down to room temperature and characterized by UV-Vis spectroscopy, Dynamic Light Scattering, Transmission Electron Microscopy.

5.5.2. GNP characterization

Dynamic Light Scattering (DLS) Measurements. The size of GNPs was measured at 25 °C with a Dynamic Light Scattering Zetasizer Nano equipped with a red (633 nm) laser at a fixed angle of 173°. DTS applications 6.12 software was used to analyze the data. All sizes were refered to number average. For each sample, three DLS measurements were performed with a fixed 10 runs per 10 second measurement.

Transmission electron microscopy (TEM) analysis. TEM images were obtained with a Tecnai G2 microscope (FEI). The particle samples (2 nM) were suspended in milliQ water, placed on a carbon coated copper grid and the water was allowed to dry at room temperature. The average diameter of particles was calculated by measuring 200 individual particles with SIS Soft Imaging GmbH image analysis software.

The polymer functionalized GNP samples were negatively stained with 1% uranyl acetate dissolved in distilled water, and analyzed as described below.

Concentration assessment. The concentration of gold nanoparticle suspensions was assessed according to the method reported by Liu et co-workers [118]. Equation (2) was applied to derive the molar extinction coefficient (ε_{506}) referred to the sample absorbance at 506 nm:

$$(2) \quad \ln \varepsilon = k \ln D + a$$

where D is the diameter of the nanoparticles (measured by DLS), k and a are two constants whose values are 3.32111 and 10.80505, respectively [119,120].

The gold nanoparticles concentration (M) was calculated with the Lambert–Beer Equation (3):

$$(3) \quad Conc.\,(\mathrm{M}) = A_{506} / \varepsilon_{506} b$$

where A_{506} is the sample absorbance at 506 nm and b is the cell path length.

5.5.3. Assessment of GNP surface decoration efficiency

Particles were incubated with increasing ratios of the different polymers generated in order to assess the efficiency of conjugation. Folate-PEG_{2kDa}-SH, Folate-$PEG3_{3.5kDa}$-SH, Rhodamine-PEG_{2kDa}-SH, $mPEG_{2kDa}$-SH and poly(MCH-co-GMA) aqueous solutions

were prepared. Different volumes of each polymer solution were added to 3 nM gold nanoparticle suspensions to generate samples with increasing polymer/GNPs molar ratios. A reference sample, which corresponds to the polymer amount added to the particles, was prepared for each polymer excess by replacing the particle volume with milliQ water.

After 8 hours of rotational stirring at room temperature, the nanoparticles were removed by centrifugation at 14000 rpm for 30 minutes. The supernatants containing Folate–PEG were tested by Iodine assay and UV-Vis spectroscopy at 363 nm to quantify unbound Folate-PEG, supernatants containing Rhodamine–PEG were tested by Iodine assay and UV-Vis spectroscopy at 552 nm to quantify unbound Rhodamine-PEG; supernatants containing mPEG were tested by Iodine assay to quantify unbound mPEG; supernatants containing poly(MCH-co-GMA) were tested by UV-Vis spectroscopy at 300 nm to quantify unbound poly(MCH-co-GMA).

5.5.4. Production of polymer decorated GNPs

Folate targeted GNPs: 11.8 µL of 0.5 mg/mL FA-$PEG_{3.5kDa}$-SH aqueous solution were mixed with 6 µL of 50 µg/mL $mPEG_{2kDa}$-SH aqueous solution. The polymer mixture was quickly added to a 3 nM gold nanoparticle suspension (10 mL) to a final 50:5:1 FA-$PEG_{3.5kDa}$-SH /$mPEG_{2kDa}$-SH/GNP molar ratio. The mixture was left under rotational stirring overnight at room temperature. An aliquot (1 mL) of the mixture was centrifuged at 14000 rpm for 30 minutes at 4 °C to isolate the particles and the supernatant was analyzed by UV-Vis spectroscopy at 363 nm to assess the unbound FA-$PEG_{3.5kDa}$–SH. Then, 48 µL of 5 mg/mL $mPEG_{2kDa}$-SH aqueous solution were added to the particle suspension aiming to saturate the particle surface with $mPEG_{2kDa}$-SH as stabilizing component ($mPEG_{2kDa}$-SH/GNP molar ratio= 4000:1). The mixture was left overnight under rotational stirring. The resulting particle suspension was centrifuged at 14000 rpm for 30 minutes at 4 °C. The suspension supernatant was analyzed by Iodine test (FA-$PEG_{3.5kDa}$-SH + $mPEG_{2kDa}$-SH). The GNP pellet was diluted 10 times in milliQ water and analyzed by Dynamic Light Scattering (DLS) and by UV-Vis spectroscopy in the range 600-400 nm for the determination of the size and the particle concentration, respectively. Control non targeted particle (mPEG-GNPs) were produced and characterized as describe above, using $mPEG_{3.5kDa}$-SH instead of FA-$PEG_{3.5kDa}$-SH. Particle size and morphology were characterized also by TEM analysis

Rhodamine labelled gold nanoparticles: Folate targeted gold nanoparticle formulations were produced by decorating the particle surface with increasing ratio of Folate–$PEG_{3.5kDa}$-SH. All the particle batches were labelled with Rhodamine-PEG_{2kDa}-SH to allow the particle tracking *in vitro*. Typical particle surface decoration procedure is explained hereinafter. In the first step, gold nanoparticles were functionalized with increasing ratio of targeting agent Folate–$PEG_{3.5kDa}$-SH combined with 10% mol/mol of $mPEG_{2kDa}$-SH to ensure the particle stability. For particle visualization and stabilization, GNP surface was saturated with Rhodamine-PEG_{2kDa}-SH.

23.6 µL of 0.5 mg/mL FA–$PEG_{3.5kDa}$-SH aqueous solution were mixed with 12 µL of 50 µg/mL $mPEG_{2kDa}$-SH aqueous solution. The polymer mixture was added to a 3 nM gold nanoparticle suspension (10 mL) in order to achieve a 100:10:1 FA–$PEG_{3.5kDa}$ -SH /$mPEG_{2kDa}$-SH/GNP molar ratio and the suspension was left under rotational stirring overnight at room temperature. An aliquot (1 mL) of the mixture was centrifuged at 14000 rpm for 30 minutes at 4 °C to isolate the particles and the supernatant was analyzed by UV-Vis spectroscopy at 363 nm to assess the unbound FA-$PEG_{3.5kDa}$–SH.

Subsequently Rho-PEG_{2kDa}-SH (5 mg, 2.07 µmol) was dissolved in 1 mL of milliQ water and 14.5 µL of the solution were added the particle suspension together with 12 µL of 0.5 mg/mL $mPEG_{2kDa}$-SH aqueous solution. (1000:100:1 Rho–PEG_{2kDa}-SH/ $mPEG_{2kDa}$-SH/GNP molar ratio). Control non targeted particles (mPEG-GNPs) were produced by replacing the amount of Folate- $PEG_{3.5kDa}$-SH with $mPEG_{3.5kDa}$-SH. The resulting decorated particles were recovered by centrifugation at 14000 rpm for 30 minutes at 4 °C. The GNP pellet was diluted 10 times in milliQ water and analyzed by Dynamic Light Scattering (DLS) and TEM, and by UV-Vis spectroscopy in the range 600-400 nm for the determination of the size and the particle concentration, respectively. The supernatant was analysed by UV-Vis spectroscopy at 552 nm for the determination of the unbound Rho-PEG_{2kDa}-SH.

Folate targeted pH responsive GNPs: Folate–PEG_{2kDa}-SH (5 mg, 2.06 µmol) was dissolved in milliQ water and diluted to obtain a 0.5 mg mL^{-1} solution. In a vial, 11 µL of 0.5 mg mL^{-1} Folate–PEG_{2kDa}-SH solution (5.46 µg, 2.25 nmol) were mixed with 9 µL of a 50 µg mL^{-1} $mPEG_{2kDa}$-SH solution in water (0.45 µg, 0.22 nmol). The mixture was quickly added to 15 mL of freshly prepared 3 nM GNP suspension to yield a 50:5:1

Folate-PEG-SH/mPEG-SH/GNP molar ratio. The particle suspension was incubated at room temperature under rotational stirring overnight protected from the light. Bdp-PEG_{2kDa}-SH (5 mg, 2.18 μmol) was dissolved in 1 mL of milliQ water and diluted ten times in milliQ water. GNP suspension was added of 21 μL of the 0.5 mg mL^{-1} Bdp-PEG-SH solution yielding a 100:1 Bdp-PEG-SH/GNP molar ratio and the suspension was left under rotational stirring overnight at room temperature. Afterwards 278 μL of a 8 mg mL^{-1} solution of poly(MCH-co-GMA) in 0.2 N NaOH were added to the GNP sample (3000:1 poly(MCH-co-GMA) /GNP molar ratio and the mixture was stirred overnight at room temperature in the dark. A reference mixture was also prepared with the same ratio and concentrations of polymer without GNPs. The particles were isolated by centrifugation at 14000 rpm for 30 minutes. The supernatant was isolated and analyzed by UV-Vis spectroscopy at 300 nm. The particle pellet was resuspended in milliQ water and centrifuged again to remove unreacted components; this process was repeated three times. The nanoparticle suspension was analyzed by different techniques to assess the size, morphology and concentration: UV-Vis spectroscopy, Dynamic Light Scattering and Transmission Electron Microscopy.

5.5.5. Stability studies of gold nanoparticles

Naked GNPs, PEGylated GNPs and Folate targeted pH responsive GNPs were diluted with either milliQ water or Folic-free DMEM without serum at pH 6.5 or 7.4 to a final concentration of 2 nM. Particles size was then analyzed with Dynamic Light Scattering (DLS) at scheduled intervals for 2 hours.

5.6. IN VITRO CELL STUDIES

5.6.1. Cell culture

KB cells (human cervical carcinoma) were grown at 37 °C, in 5% CO_2 atmosphere, using folic acid free DMEM medium supplemented with 15% FBS, 2 mM L-glutamine, 100 IU/mL penicillin, 100 μg/mL streptomycin and 0.25 μg/mL of amphotericin B (Sigma-Aldrich). MCF-7 (human breast adenocarcinoma) were grown at 37 °C, in 5% CO_2 atmosphere, using RPMI-1640 medium supplemented with 10% FBS, 100 IU/mL penicillin, 100 μg/mL streptomycin and 0.25 μg/mL of amphotericin B.

5.6.2. Cell viability assay

MCF-7 cells in RPMI-1640 containing 10% fetal bovine serum (FBS) and KB cells in FFDMEM added of 15% of FBS were seeded in a 96-well plate at a density of 5×10^3 cells per well (200 µL/well). After 24 hours, the medium was replaced with *Folate targeted pH responsive GNP* suspension at concentrations in the 0.2-2 nM range, in FFDMEM at pH 7.4 and pH 6.5 and cells were incubated for 6 hours. Afterwards, the medium was removed and each well was washed three times with 100 µL of PBS and 200 µL of fresh FFDMEM was placed per well. The cell viability was tested by the MTT assay. 20 µL of MTT solution (5 mg/mL in PBS pH 7.4) were added to each well and the plates were incubated for 3 hours at 37 °C. Then the medium was removed and formazane crystals were dissolved into 200 µL of DMSO per well. The absorbance of each well was read by an EL311SK microplate autoreader (Bio-Tek Instruments, Winooski, VT-USA) at a wavelength of 570 nm. All experiments were repeated six times.

CELL UPTAKE STUDIES

5.6.3. Atomic Absorption Spectroscopy on cell lysates

MCF-7 and KB cells in Folic free DMEM medium (FFDMEM) containing 15% fetal bovine serum (FBS) were seeded in 12-well plates at a density of 5×10^5 cells per well and grown for 24 hours. Then, the medium was replaced with 2 nM *Folate targeted pH responsive GNPs* in FFDMEM at pH 7.4 and 6.5; while 2 nM *Folate targeted GNPs and Rhodamine labelled Folate targeted GNPs* were tested on cells in FFDMEM at pH 7.4. After 2 hours of incubation at 37 °C, the particle containing medium was removed and the cells were washed 3 times with PBS without $MgCl_2$ and $CaCl_2$. The cells were then detached by 1% w/v trypsin treatment (150 µL per well). The trypsin was blocked by adding 500 µL of PBS with $MgCl_2$ and $CaCl_2$ and the sample was centrifuged at 1000 rpm for 5 minutes. The cellular pellets were washed twice with PBS and then added of Triton® X-100 0.1% in water (600 µL). All cellular samples were lysated under ultrasounds treatment for 1 hour and then centrifuged at 1000 rpm for 5 minutes. 500 µL of cell lysate were digested by aqua regia treatment (HNO_3/HCl 1:3 v/v, 5 mL) at 80 °C for 1 hour. The mineralized samples were diluted

to 5 mL with 1 % w/v HCl. Gold quantification was performed by Atomic Absorption Spectrometry (AAS) using a Varian AA240 Zeeman instrument equipped with a GTA120 graphite furnace, Zeeman background corrector and an autosampler (Varian Inc., Palo Alto, CA-USA). The gold content was normalized by the number of cells which was derived by the BCA Protein Assay (Thermo Fisher Scientific Inc.,Waltham, MA-USA) performed on 100 µL of the cell lysate.

5.6.4. Flow cytometric analysis

KB cells were seeded in 12-well plates at the density of $3x10^5$ cells per well and allowed to adhere and acclimate for one day. The medium was discharged, replaced with 2 nM polymer decorated GNP suspensions (*Folate targeted pH responsive GNPs* in FFDMEM at pH 7.4 and 6.5; while 2 nM *Rhodamine labelled Folate targeted GNPs* were tested on cells in FFDMEM at pH 7.4. and cells were incubated for 2 hours at 37 °C in a humidified 5% $C0_2$ incubator. Then, cells were washed with PBS without $CaCl_2$ and $MgCl_2$ (3 x 1 mL) and detached by treatment with 1% w/v trypsin in PBS without $CaCl_2$ and $MgCl_2$ (150 µL per well). After 4 minutes of incubation at 37 °C, trypsin activity was blocked by addition of 500 µL of FFDMEM and cells were recovered by centrifugation at 1000 rpm for 5 minutes. Supernatants were removed and the cellular pellet was fixed with freshly prepared 4% w/v paraformaldehyde (PFA) in PBS for 15 minutes. Samples were centrifuged at 1000 rpm for 5 minutes, washed with PBS to remove PFA traces and analyzed by flow cytometry. Cell samples incubated with *Rhodamine labelled Folate targeted GNPs* were analized at λ_{ex} 550 and λ_{em} 575 for Rhodamine detection. Cell samples incubated with *Folate targeted pH responsive GNPs* were analysed λex 488 nm ex and λem 525 nm for Bodipy detection.

5.6.5. Confocal microscopy

KB cells were seeded onto 35 mm imaging dishes (MatTek, Ashland, US) at the density of 1.5 x 10^5 cell per well in FFDMEM added of 15% v/v Fetal Bovine Serum (FBS) and grown for 48 hours at 37°C and 5% CO_2. 250 µL of 2 nM *Folate targeted pH responsive GNPs* and *Rhodamine labelled Folate targeted GNPs* in FFDMEM at pH 7.4.and 6.5 were added to each dish and cells were incubated at 37 °C in the dark for 2 hours. FA-C_5-Rho was tested on KB cells under the same condition at the

concentration of 100 nM, a comparable concentration to the amount of Folate-PEG on the surface of *Folate targeted pH responsive GNPs*. Particle suspensions or FA-C_5-Rho solution were removed and wells were gently washed three times with PBS. Cells were incubated in pre-warmed imaging medium (phenol red-free DMEM pH 7.4 containing 25 mM HEPES and supplemented with 1 mg/mL BSA). Cells were imaged on a Leica SP5 confocal laser-scanning microscope equipped with a 488 nm Ar laser, 543/633 nm HeNe laser, 100 × 1.4 NA or 40x 1.4 NA objectives using a Leica Type F immersion oil. Cell samples incubated with *Rhodamine labelled Folate targeted GNPs* were irradiated with a 514 nm laser for Rhodamine detection; cell samples incubated with *Folate targeted pH responsive GNPs*. were irradiated with a 488 nm laser for Bodipy FL detection. The microscopy imaging was performed on live cells.

The confocal images were analyzed through an ImageJ script without any manual intervention. The selection of Fluorescent pixels was performed after setting an ImageJ IsoData threshold to derive the fluorescence intensity. The background intensity was set by looking at pixels that showed a fluorescence intensity below the IsoData threshold. The fluorescence intensity correction of each image was performed by subtracting the background intensity from the intensity value. Corrected mean intensities were calculated as the mean intensity value of 5 images for each sample. All the fluorescence intensity values were normalized to the relative maximum corrected mean intensity value. The mean normalized intensity from 3 independent experiments was plotted.

5.6.6. Transmission electron microscopy (TEM) of KB cells

Intracellular disposition of gold nanoparticles was imaged by TEM analysis. KB cells were seeded at the density of 3 x 10^5 cells per well in 12 wells plates. After 24 *Folate targeted pH responsive GNPs* were tested on cells in FFDMEM at pH 7.4 and 6.5; while 2 nM *Folate targeted GNPs and Rhodamine labelled Folate targeted GNPs* were tested on cells in FFDMEM at pH 7.4.

After 2 hours of incubation at 37 °C, the medium was discharged and the cells were washed three times with PBS. Cells were fixed with 2.5 % w/v glutaraldehyde in 0.1 M sodium cacodylate buffer at 4 ˚C for 1 hour. The cells were washed twice with sodium cacodylate buffer and post fixed in 1% w/v osmium tetroxide in 0.1 M sodium cacodylate buffer for 1 h. Cell samples were dehydrated using ethanol. Afterwards the

samples were embedded in fresh EPON resin. Ultrathin sections of the samples were cut and observed with Tecnai G2 Transmission Electron Microscope (FEI, Oregon, USA).

5.6.7. Cell uptake inhibition assay

KB cells were seeded in 12-well tissue culture treated plates at a density of 5 x 10^5 cells/well. After 24 hours the culture medium was discharged and the cells were treated with 0.5 mL of GNP suspensions in FFDMEM) at pH 7.4 and 6.5, added of 200 μM free Folate. After 2 hours incubation time, the samples were treated as described above for Atomic Absorption, Flow cytometry and confocal microscopy analysis.

5.7. INTRACELLULAR TRAFFICKING STUDIES

5.7.1. Particle trafficking to the liposomes

KB cells were seeded onto 35 mm imaging dishes (MatTek, Ashland, US) at the density of 1.5 x 10^5 cell per well in FFDMEM added of 15 % v/v Fetal Bovine Serum (FBS) and grown for 48 hours at 37 °C and 5% CO_2. Cells were pulsed for 8 hours with Dex-647 (50 μg/mL in FFDMEM supplemented with 15% v/v FBS) to allow the lysosome labelling. Then cells were chased for 12 hours in dextran-free FFDMEM complete medium. Cells were incubated for 30 minutes with the following samples:

- 2 nM GNPs decorated with 10 chains of FA-$PEG_{3.5kDa}$-SH and labelled with Rhodamine (10x FA-PEG-GNPs) in FFDMEM medium
- 2 nM GNPs decorated with 50 chains of FA-$PEG_{3.5kDa}$-SH and labelled with Rhodamine (50x FA-PEG-GNPs) in FFDMEM medium
- 100 nM FA-C_5-Rho solution in FFDMEM medium

After the incubation, the medium was discharged, the cells were washed with PBS for three times and added of pre-warmed imaging medium (phenol red-free DMEM pH 7.4 containing 25 mM HEPES and supplemented with 1 mg/mL BSA). Cells were incubated at 37 °C , 5% CO_2 atmosphere and were imaged at scheduled times (0, 1, 2

and 4 hours) on a Leica SP5 confocal laser-scanning microscope equipped with a 488 nm Ar laser, 543/633 nm HeNe laser, 100 × 1.4 NA or 40x 1.4 NA objectives using a Leica Type F immersion oil.

Fluorescence microscopy images of Rhodamine labelled particles (50x FA-PEG-GNPs and 10x FA-PEG-GNPs) and the conjugate FA-C_5-Rho in the 514 channel and the images of Dex-647 in the 633 channel were captured simultaneously. Dex-647 was used to label the lysosomal regions. Analysis of each field was performed using an ImageJ script without manual intervention. A Li threshold was applied to the Dex-647 channel aiming to identify the lysosomal regions. The background fluorescence intensity was calculated by setting an IsoData threshold and considering the mean intensity of pixels below this threshold for each channel. The image analysis of samples incubated with Rhodamine labelled particles (514 nm channel) and the images for lysosome tracking (633 nm channel) allowed to derive the fluorescence intensity of Rhodamine in the lysosomes. Rhodamine fluorescence intensity within the lysosome was corrected by subtracting the background intensity from the intensity value. The mean intensity value of 5 images for each sample provided the corrected mean intensity value. All the values were normalized to the relative maximum corrected mean intensity value which provided the normalized intensity for each sample. The mean normalized intensity in Lysosomes from 3 independent experiments was plotted.

The colocalization of Rhodamine labelled particles (50x FA-PEG-GNPs and 10x FA-PEG-GNPs) and the conjugate FA-C_5-Rho within lysosomes was evaluated by Pearson's coefficient (PC). 5 images per time point were captured and analysed. To avoid the variation between a cell and another, 5 individual cells were manually selected for each image. PC values were calculated using the JaCOP ImageJ plugin and the mean PC value of 5 cells per 5 different images per time point was calculate. Standard deviation was calculated as variation between mean PC values of 3 independent experiments.

5.7.2. Pathway inhibition assay

KB cells were seeded onto 35 mm imaging dishes (MatTek, Ashland, US) at the density of 1.5 x 10^5 cell per well in FFDMEM added of 15% v/v Fetal Bovine Serum (FBS) and grown for 48 hours at 37 °C and 5% CO_2. Cells were preincubated for 30

minutes at 37 °C with 80 μM Dynasore in FFDMEM without serum. Then the medium was removed and cells were incubated for 30 minutes with the following samples in the presence or absence of Dynasore (80 μM):

- 10 μg/mL AlexaFluor 488 labelled Transferrin (Tf-488) in FFDMEM without FBS
- 100 nM FA-C_5-Rho in FFDMEM without FBS
- 2 nM Rhodamine labelled GNPs decorated with 50 chains of FA-$PEG_{3.5kDa}$-SH (50x FA-PEG-GNPs) in FFDMEM without FBS

After incubation, the medium was discharged, cells were washed 3 times with PBS and fixed with 4% w/v PFA in PBS for 15 minutes. Cells were washed twice with PBS and then analyzed by confocal microscopy. Tf488, FA-C_5-Rho and *Rhodamine labelled Folate targeted GNPs* were irradiated with a 514 nm laser for AlexaFluor 488 and Rhodamine detection. The uptake inhibition due to the presence of Dynasore was evaluated.

5.8. IN VITRO SONODYNAMIC TREATMENT

5.8.1. Ultrasound treatment and cell proliferation assay

KB and MCF7 cells in the exponential growth phase were incubated for 2 hours with 2 nM FA-PEG-GNP and mPEG-SH suspensions in FFDMEM and cells were incubated for 2 hours. Then cells were detached with 0.05% trypsin-0.02% EDTA solution (Sigma). Aliquots of 1 mL cell suspensions adjusted to 5 × 105 cell/mL were collected in polystyrene tubes which were completely filled with PBS. Cell-containing tubes were treated with continuous 1.8 MHz ultrasound (US), at energy flux density (EFD) of 0.008 mJ/cm^2 for 5 minutes. The ultrasound exposure was performed under a dim light without observing any temperature increase in the medium. After the treatment, cell growth was monitored by WST-1 cell proliferation assay (Roche) to evaluate the effects of the US treatment. In detail, 2 × 103 cells were seeded in 96-well culture plates (100 μL/well) in replicates (n=8). WST-1 reagent (10 μL) was added at 24, 48, and 72 hours, and the plates were incubated at 37°C in 5% CO2 atmosphere for 2 hours. The absorbance at 450 and 620 nm (reference wavelength) was measured by

in a microplate reader (Asys UV340; Biochrom, Cambridge, UK). Cell proliferation data were expressed as a percentage of untreated cells.

5.8.2. Cell competition assay

Cell uptake competition assay was performed, as reported in "CELL UPTAKE STUDY" section, by addiction of 200 μM free Folate to the 2 nM FA-PEG-GNP suspension in FFDMEM. Cells were then detached and subjected to ultrasound treatment as described above.

5.8.3. Cell death analysis

KB cell death was evaluated using the Dead Cell Apoptosis Kit with allophycocyanin (APC)-Annexin V and Sytox® Green (Life Technologies, Milan, Italy) with a C6 flow cytometer. Cells were incubated for 2 h with culture medium containing 2 nM FA-PEG-GNPs, cells were then trypsinized, PBS washed and normalized to to 5×10^5 cell/mL in 2.5 mL of PBS for ultrasound treatment. After ultrasound exposure cells were seeded in 6-well culture plates for 2 h, then collected, washed twice in 1x Annexin-binding buffer at 1500 rpm for 5 min and stained with APC-Annexin V and Sytox® Green for 15 minutes at 37 °C. Any cell debris with low forward light scatter and side light scatter were excluded from the analyses and a total of 10,000 events were analyzed. Fluorescence was collected at 660 and 530 nm to discriminate APC-Annexin V and Sytox® Green signals, respectively.

6. RESULTS AND DISCUSSION

6.1. SYNTHESIS OF MONOMERS, INTERMEDIATED AND POLYMERS

6.1.1. Synthesis of Lipoic terminating CTA

The preparation of *Folate targeted pH responsive gold nanoparticles* involved the synthesis of a pH sensitive polymer featuring a pKa in the 6-7 range, a targeting agent and a fluorescent moiety. To chemically adsorb these materials on the particle surface, a thiol-terminating PEG can be used: the S–H bond cleaves and the thiol molecule chemisorbs to the surface through a fairly strong Au–S bond. This is the strategy that we used for the synthesis of the targeting ligand, Folate-PEG-SH, and the fluorescent labels, Rhodamine-PEG-SH and Bodipy-PEG-SH.
A second method for decorating GNP surface is by replacing the terminal thiol substituent with a disulfide moiety. Lipoic acid was chosen to graft the pH responsive polymer to the particle surface: it possesses a disulfide moiety contained in a strained 5-membered ring that can adsorb on the gold surface by forming a stable bond. For this reason, Lipoic acid is frequently employed in the bioconjugates synthesis for gold nanoparticles decoration[121] as well as to prepare Self-assembled monolayers on gold surfaces[122].

The pH responsive polymer poly(MCH-co-GMA) was synthetized by living radical polymerization called Reversible Addition Fragmentation chain Transfer (RAFT). RAFT technology can be used to synthesize polymers with predetermined molecular weight and narrow polydispersity index (PDI). Moreover this procedure endorses to control the polymer architecture allowing the production of linear block copolymers, random copolymers, star polymers and many other complex structures. RAFT polymerization is a chain transfer process which involves a chain transfer agent (CTA), known as RAFT agent, which affects polymer length, chemical composition and rate of the reaction. For this thesis work we selected a Lipoic terminating CTA which enable either the particle decoration thanks to its simple coupling chemistry or the polymerization reactions.

Lipoic terminating CTA was produced by an initial activation of Lipoic acid to acyl chloride performed at 0 °C since it is an exothermic reaction (Scheme 2. - Step I). The ^{1}H NMR analysis confirmed the Lipoic acyl chloride formation by addiction of Methanol: oxygen of methanol instantly attacks the fairly positive carbon of Lipoic acyl chloride leading to the formation of the ester and hydrogen chloride, clearly visible in the ^{1}H NMR spectrum by the formation of a peak at 3.6 ppm corresponding to the methoxide group.

In the second step, a short alkane chain (Tetraethylene glycol) was introduced between the Au surface and the polymer chain, which is thought to produce a dense, ordered "brush" morphology on the Au surface[123].

TEG was dried from water by azeotropic distillation with toluene under reduced pressure. Then Lipoic acyl chloride was added dropwise to the TEG solution in DCM in order to avoid the dimer formation (Scheme 2. - Step II).

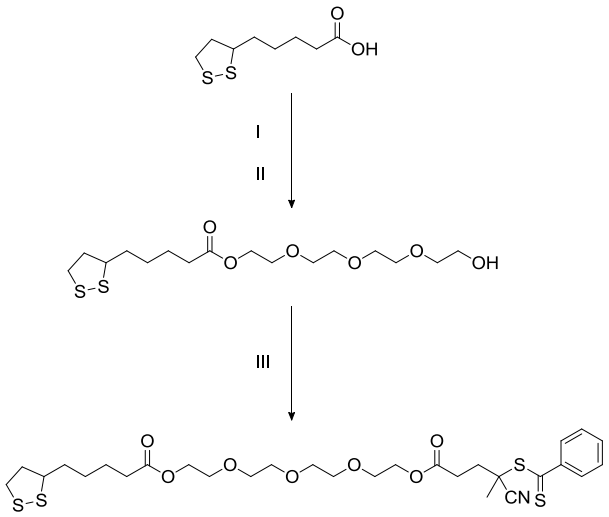

Scheme 2. Synthesis of Lipoic terminating CTA. Reaction conditions: I. Oxalyl chloride, anhydrous DCM, 0 °C. II. TEG, anhydrous DCM. III. 4-cyano-4-(phenylcarbonothioylthio) pentanoic acid/ DCC/ DMAP, DCM 0 °C.

The product Lipoic-TEG was purified by the 10-fold TEG excess by flash chromatography, isolating a yellow viscous oil which was characterized by ^{1}H and ^{13}C NMR, FTIR analysis and ESI TOF mass spectrometry. Expected a signal for m/z [M+H] 383.15 u.m.a., found 383.09 Da; and one signal at 404.99 Da for [M+Na].

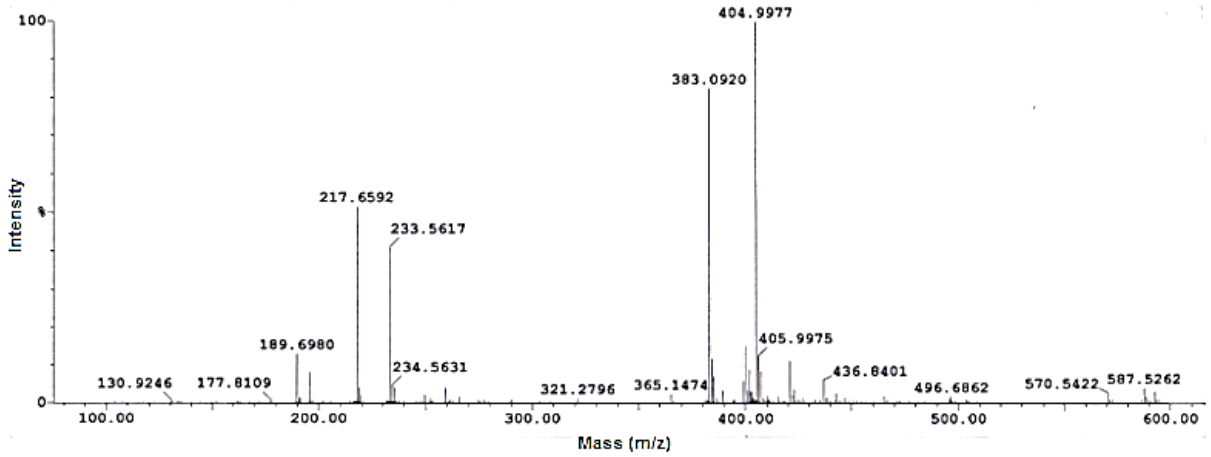

Figure 16. ESI TOF mass spectrometric analysis of Lipoic-TEG conjugate.

Lipoic-TEG was finally conjugated to 4-cyano-4-(phenylcarbonothioylthio) pentanoic acid, obtaining the Lipoic terminating CTA, used for the further polymerization reactions. The Lipoic RAFT agent chemical identity was confirmed by ^{1}H NMR, FTIR analysis and ESI TOF mass spectrometry. Expected m/z [M+H] 643.18 u.m.a., found 644.18 u.m.a. $[M+H]^{1+}$ and 666.16 u.m.a. $[M+Na]^{+}$.

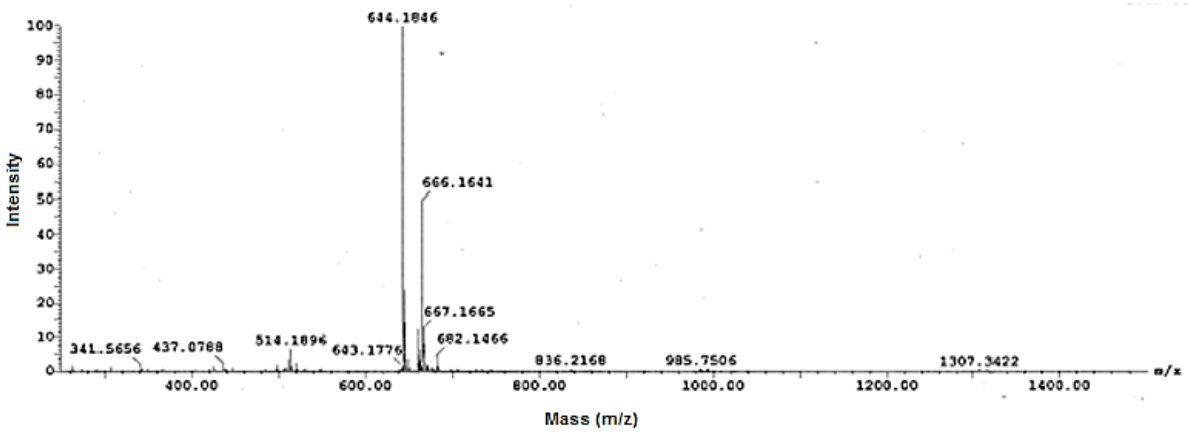

Figure 17. ESI TOF mass spectrometric analysis of Lipoic terminating CTA.

6.1.2. Synthesis of poly(MCH) macro CTA

2-(methacryloyloxy)ethyl-3-chloro-4-hydroxybenzoate monomer(MCH) was produced as described in previously reported procedures[116], and used as unit in the production of the pH responsive block of the di-block copolymer poly (MCH-co-GMA).

Poly(MCH-co-GMA) was used to decorate the surface of *Folate targeted pH responsive gold nanoparticles* which were designed to selectively accumulate in the tumor

compartment, avoiding the uncontrolled biodistribution in the body as result of the interplay of each component of the system. The pH responsiveness of the particle decorating polymer assures the targeting agent exposition once reached the target tissue. Notably poly(MCH-co-GMA) was selected among an array of pH responsive materials since it showed a satisfactory pKa (in the physiopathological range) for the aim of the project. The pH responsiveness is modulated by the MCH/GMA monomer molar ratio in the polymer backbone and by the polymer molecular weight. A key parameter is the polymer length to assure the targeting agent shielding and "revealing" in response to pH. For all these reasons, considering the bond distances, poly(MCH-co-GMA) was synthetized with a polymerization degree of 80 (number of monomeric units) and a MCH/GMA ratio of 1:2.

The polymerization of MCH was performed using MCH monomer, AIBN as radical initiator and Lipoic terminating CTA as RAFT agent (Scheme 3.). The molar ratio of the reagents was [Raft Agent]/[AIBN]/[MCH]=1:0.5:37.

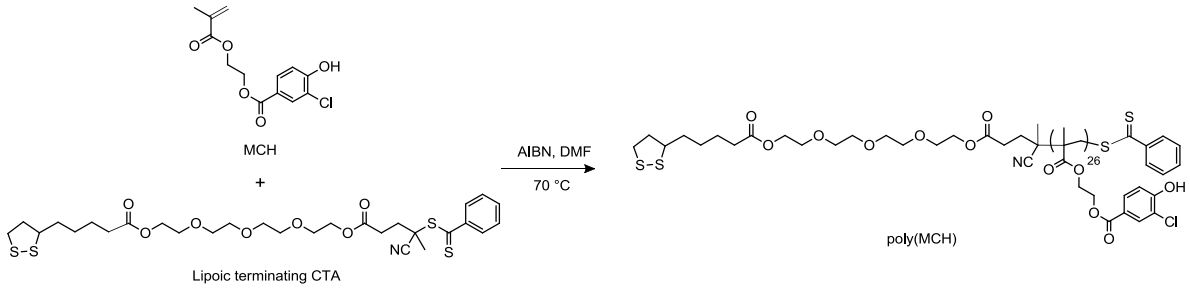

Scheme 3. RAFT polymerization of MCH to obtain poly(MCH) macro-CTA.

The reaction was monitored by ^{1}H-NMR to determine the monomer conversion. Aliquots of the reaction mixture were withdrawn at regular intervals of time and the reaction was stopped after 150 minutes once reached a monomer conversion of 70 %. The polymerization kinetic showed a first order kinetic profile, in which the rate of the reaction varies with the concentrations of the monomers (Figure 18.). The monomer conversion was calculated by monitoring the decrease of the multiplet at 4.44-4.5 ppm, relative to the two methylene groups of the MCH monomer, and the appearance of a new broad peak at 4.1-4.3 ppm, due to the polymer formation. The monomer conversion was also calculated by looking at a new broad signal at 6.9 ppm

due to the shift of the aromatic proton (originally at 7.08 ppm in the monomer) as the polymer chain grow.

The number of the repeat units in a polymer is defined by the Polymerization Degree (DP) which can be calculated by the following formula:

$$DP_n = M_n / M_0$$

where M_n is the number-average molecular weight, whereas M_0 is the molecular weight of the monomer unit.

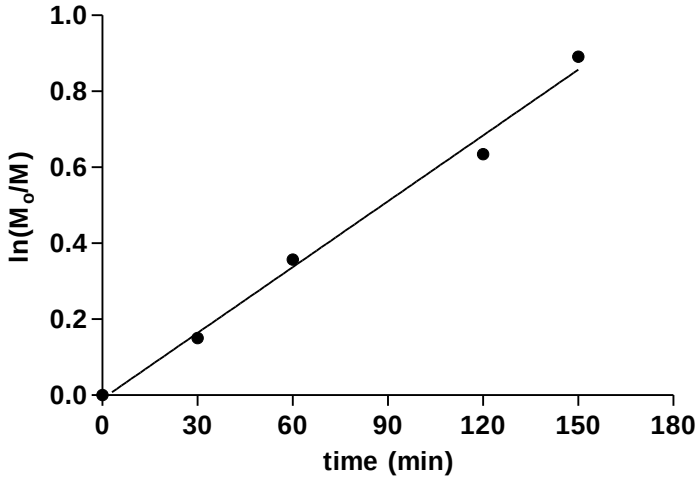

Figure 18. First order kinetic plot of the homopolymerization of MCH monomer using a Lipoic terminating CTA.

Considering the Polymerization Degree of 26, the molecular weight was calculated to be 8 kDa. The polymer was isolated by precipitation in a 1:1 (v/v) diethyl ether/petroleum ether mixture and then characterized by ^{1}H NMR and Gel Permeation Chromatography (GPC). In particular, GPC analysis showed a narrow PDI with a value of 1.13, which confirmed the high control of the RAFT polymerization technique.

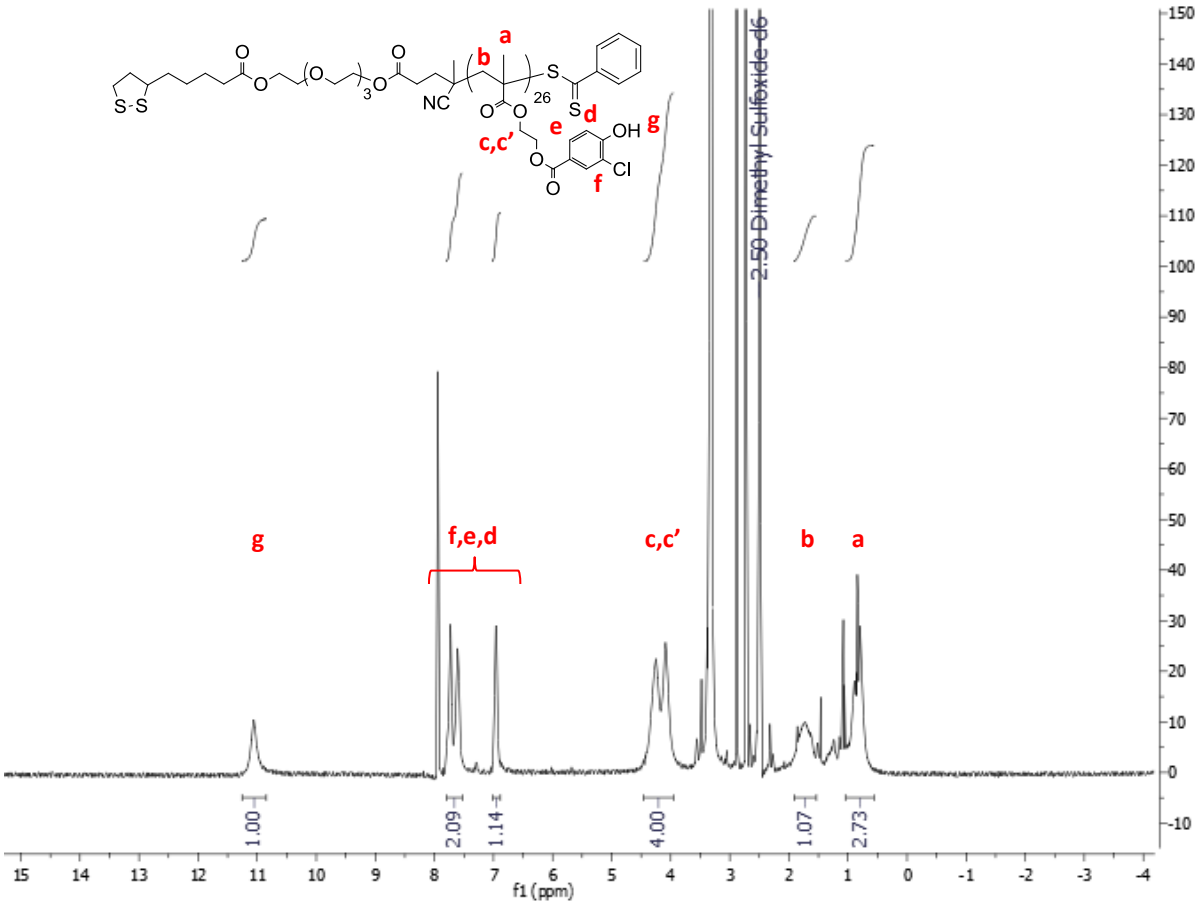

Figure 19. ^{1}H-NMR spectrum of poly(MCH) after precipitation performed in DMSO-d_6 with peak assignment.

6.1.3. Glycerol methacrylate synthesis

The Glycerol methacrylate synthesis was performed according to the protocol reported in literature[124] in which the efficient formation of diols was obtained by reacting epoxides (glycidyl methacrylate) with sulfuric acid (0.5 equiv.) in a water at RT. This method favorably competes with the classical one consisting in hydrolysis of dioxolane derivatives. Water and high-diluted H_2SO_4 were used as nucleofilic-acid catalysts and solvents and were efficient in promoting the ring opening of the epoxide to yield the diol.

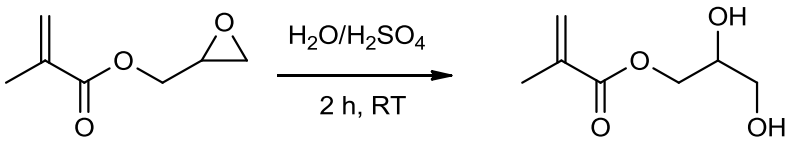

Scheme 4. Reaction scheme of the glycerol methacrylate in acidic water at room temperature.

The GMA monomer was efficiently purified by gel flash chromatography and ^{1}H-NMR, ^{13}C-NMR and ESI TOF mass spectroscopy analysis confirmed the GMA structure.

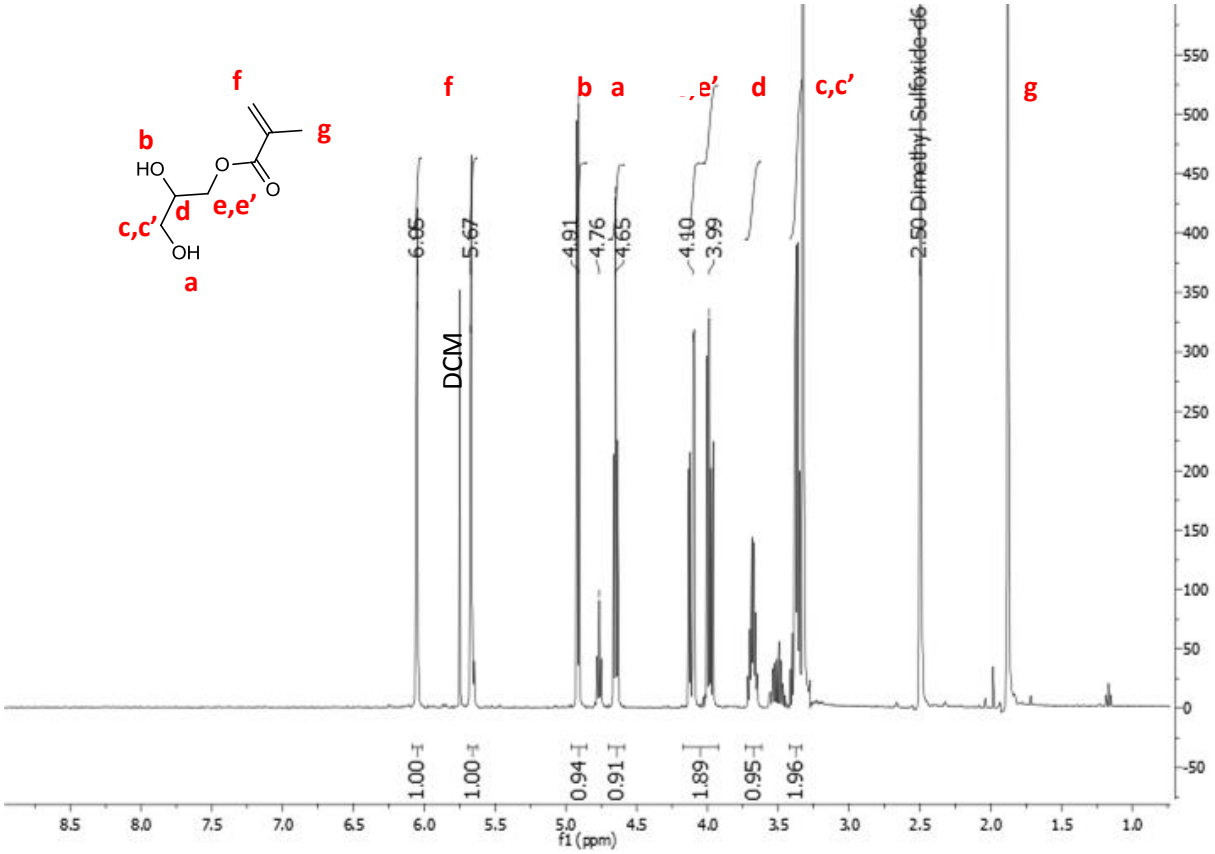

Figure 20. ^{1}H-NMR spectrum of GMA performed in DMSO-d_6 with peak assignment.

6.1.4. Synthesis of poly(MCH-co-GMA)

Poly(MCH) was by employed as macro CTA in the polymerization with GMA aiming to generate a di-block copolymer with suitable length for the aim of the project. Poly(MCH), AIBN and GMA were employed as reagents in molar ratio of [poly(MCH)]/[AIBN]/[GMA]=1:0.5:66 and the RAFT polymerization was performed at 70 °C in anhydrous DMF according to the Scheme 5.

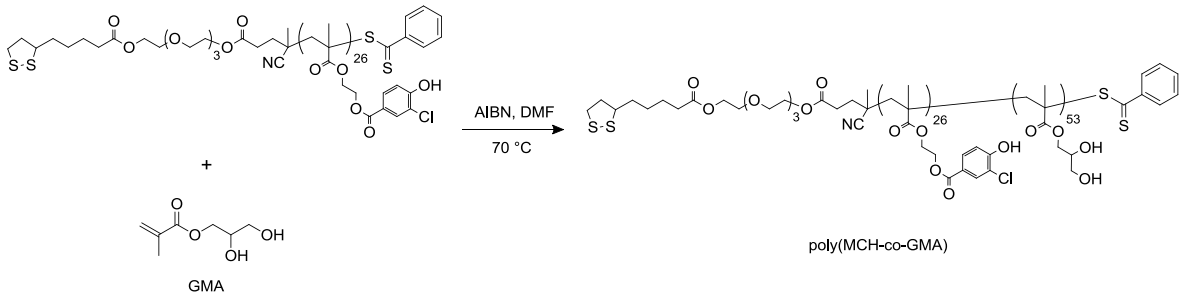

Scheme 5. Synthesis of di-block copolymer poly(MCH-co-GMA) by RAFT polymerization using poly(MCH) as macro CTA, AIBN as radical iniziator and GMA as monomer.

The polymerization progression was monitored by ^{1}H NMR through regular withdrawals of the reaction mixture, showing a first order kinetic plot (Figure 21.). The exposition of the solution to air caused the polymerization termination at a monomer conversion of 81 % (DP=53). The polymerization degree was determined by ^{1}H NMR spectroscopy in DMSO-d_6, following the decrease of the GMA vinylic proton integrals (5.74 and 6.13 ppm) referred to the DMF peak (2.97 ppm), the solvent used for the polymerization. DMF is high-boiling-solvent (153 °C) and it can be assumed that its concentration stay constant during the polymerization reaction which is performed at 70 °C. Therefore DMF can be used as internal standard to measure the decreasing in the vinylic proton integrals.

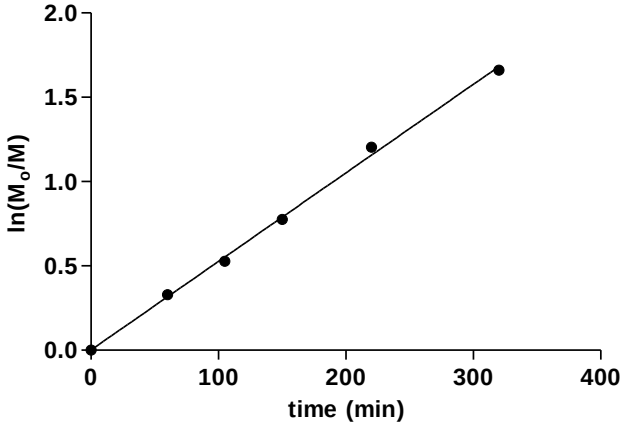

Figure 21. First order kinetic plot of the synthesis of di-block copolymer poly(MCH-co-GMA).

The polymer was purified by precipitation in diethyl ether-petroleum ether mixture and characterized by ^{1}H NMR and GPC. Notably the analysis of the ^{1}H NMR spectrum highlighted that the aromatic signals of MCH (5H at ~7 ppm) and the hydroxyl groups of GMA (2H at 4.6-4.9 ppm) have a relative ratio of 1:2, confirming the expected polymer composition. Moreover the GPC analysis revealed a PDI of 1.17, further prove of the relevance of this polymerization method.

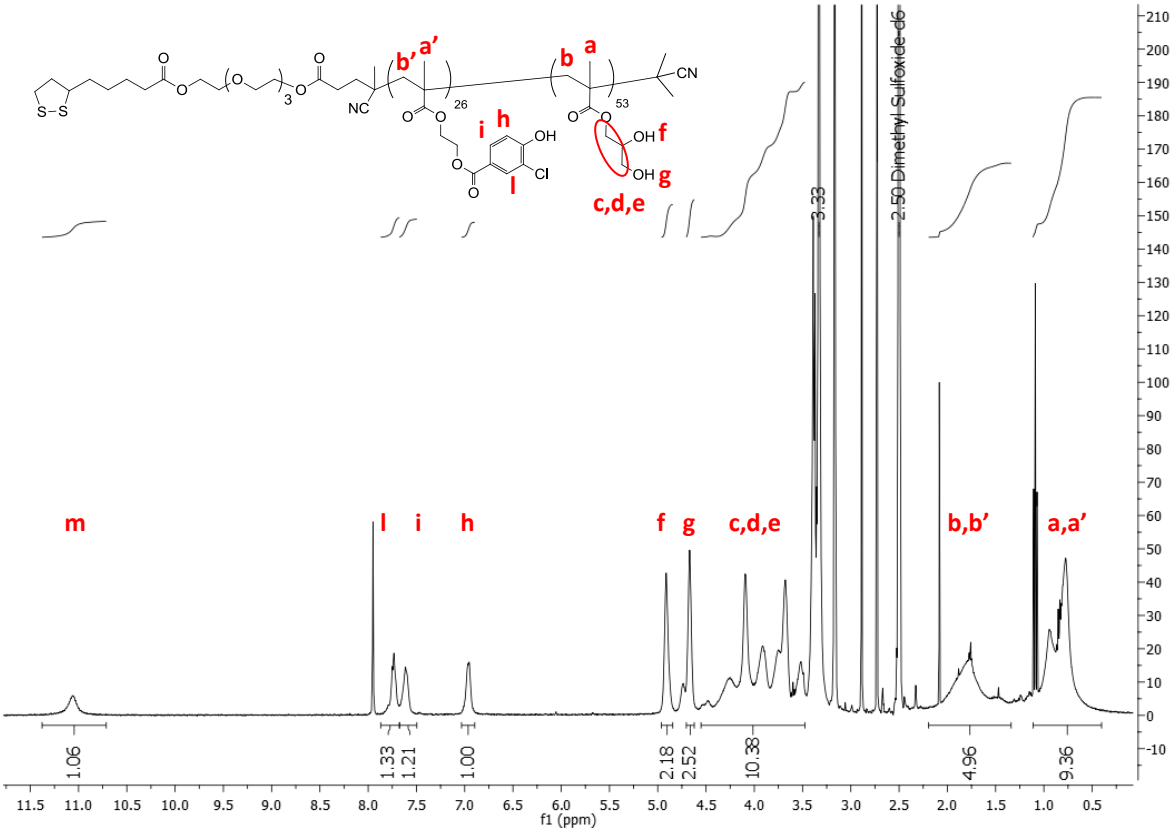

Figure 22. ^{1}H-NMR spectrum of poly(MCH-co-GMA) after precipitation, performed in DMSO-d_6 with peak assignment.

Potentiometric acid/base titration and back titration on poly(MCH-co-GMA) was carried out by adding aliquots of 1 N HCl or NaOH to a 1 mg/mL solution of the polymer. The polymer solubility decreased with the decrease of the pH due to the MCH protonation. This phenomenon caused the polymer precipitation triggered at lower pH with respect to pKa. On the other hand, the back titration showed that the polymer protonation and deprotonation occurs reversibly. Aggregation phenomena could make more difficult the access of the titrant to the phenolic group of MCH in the pH responsive block, causing a delay in the protonation/deprotonation process. For this reason, the pKa of the polymer is commonly named "apparent pKa" due to the effect of aggregation on the protonation of the polymer.

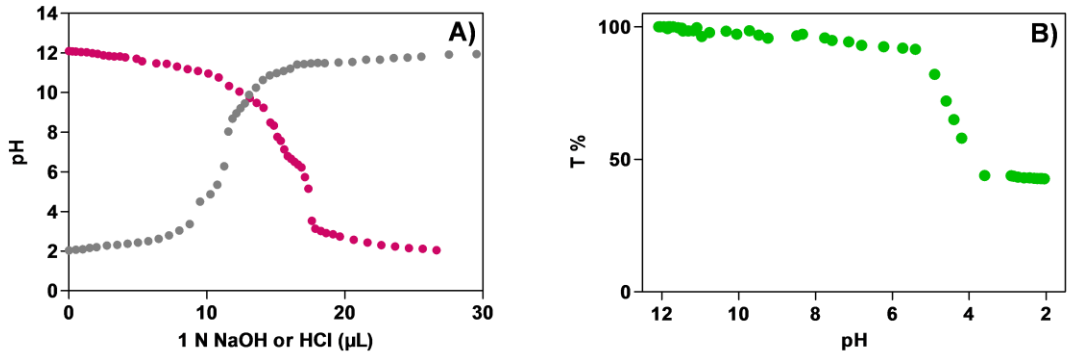

Figure 23. (A) Potentiometric Titration (●) and back titration (●) curves of poly(MCH-co-GMA). (B) Turbidimetric analysis (●) of 1 mg/mL poly(MCH-co-GMA) solution.

Turbidimetric assay was performed to assess the polymer cloud point (CP) which is defined as the pH at which precipitation occurs. Starting from a polymer solution at pH 12, the pH was gradually decreased by adding 1 N HCl and transmittance decrease, due to polymer aggregates scattering, was recorded at 500 nm (Figure 23 - B.). The polymer cloud point was shown to be 5.17, calculated as the pH at which a decrease in transmittance at 500 nm starts to be detected.

Poly(MCH-co-GMA) copolymer is soluble at physiological pH conditions, since the hydroxyl benzyl group is in its ionized form. At slightly acidic pH value, the phenolic hydroxyl moiety is protonated, and the polymer converts to an uncharged form. While the potentiometric titration provides evidence of the molecular event of the MCH monomer titration, the cloud point of the polymer is a descriptor of the

macroscopic aggregation that stems from the polymer chain conversion from coil to globule occurring when the MHC monomers undergo protonation. The cloud point is dictated by polymer protonation, and consequent hydrophobic shift, dehydration and is also affected by the polymer concentration. Notably, the polymer shift to a hydrophobic globular state is a dynamic event that takes place throughout the polymer protonation process, where the apparent pKa correspond to 50% of the MCH monomer protonation (Figure 24.).

The pH responsiveness of poly(MCH-co-GMA) can be used as sensor of the local pH decrease typical of the tumor interstitium and is suitable for the aim of the project.

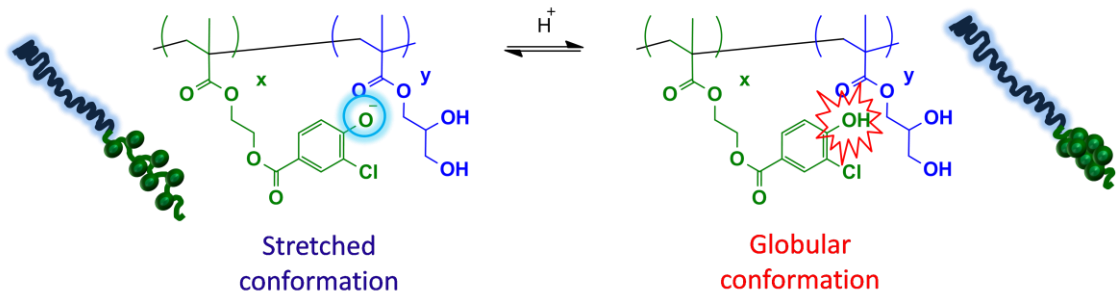

Figure 24. Poly(MCH-co-GMA) is designed to change its length upon different pH conditions. A pH decrease results in the protonation of the hydroxyl moiety of the hydroxybenzoic acid; in such a case, the polymer becomes hydrophobic and it collapses in a globular conformation.

6.1.5. Synthesis of poly(GMA)

Aiming to provide certainty that Folate biorecognition is driven by the sensing effect of the changed microenviromental pH, a polymer endowed of the same length of poly(MCH-co-GMA) (equal monomeric units) was synthetized. With this intention GMA was polymerized using AIBN as radical initiator and Lipoic terminating CTA as RAFT agent with a molar ratio of [Raft Agent]/[AIBN]/[GMA]=1:0.5:99.

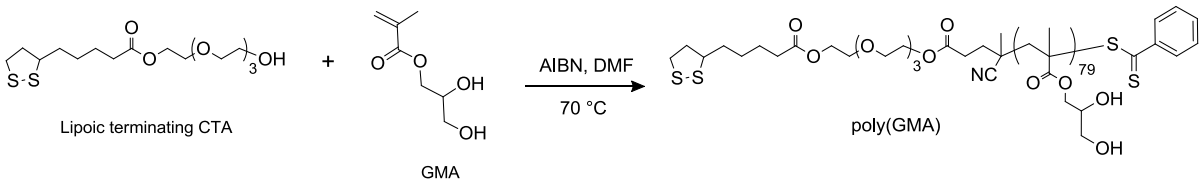

Scheme 6. RAFT polymerization of GMA to obtain poly(GMA).

The polymerization kinetic was followed by ^{1}H NMR performed at regular intervals of time. At 80 % of monomer conversion (DP=79) polymerization was stopped by exposing the reaction mixture to air. The polymerization degree was calculated monitoring the decrease of the integrals of the monomer vinyl signals (6.11 and 5.58 ppm) with respect to the singlet signal at 7.95 ppm of the DMF, used reference peak. Poly(GMA) was isolated by precipitation in 1:1 (v/v) diethyl ether/petroleum ether mixture and was characterized by ^{1}H NMR in DMSO-d_6 and GPC.

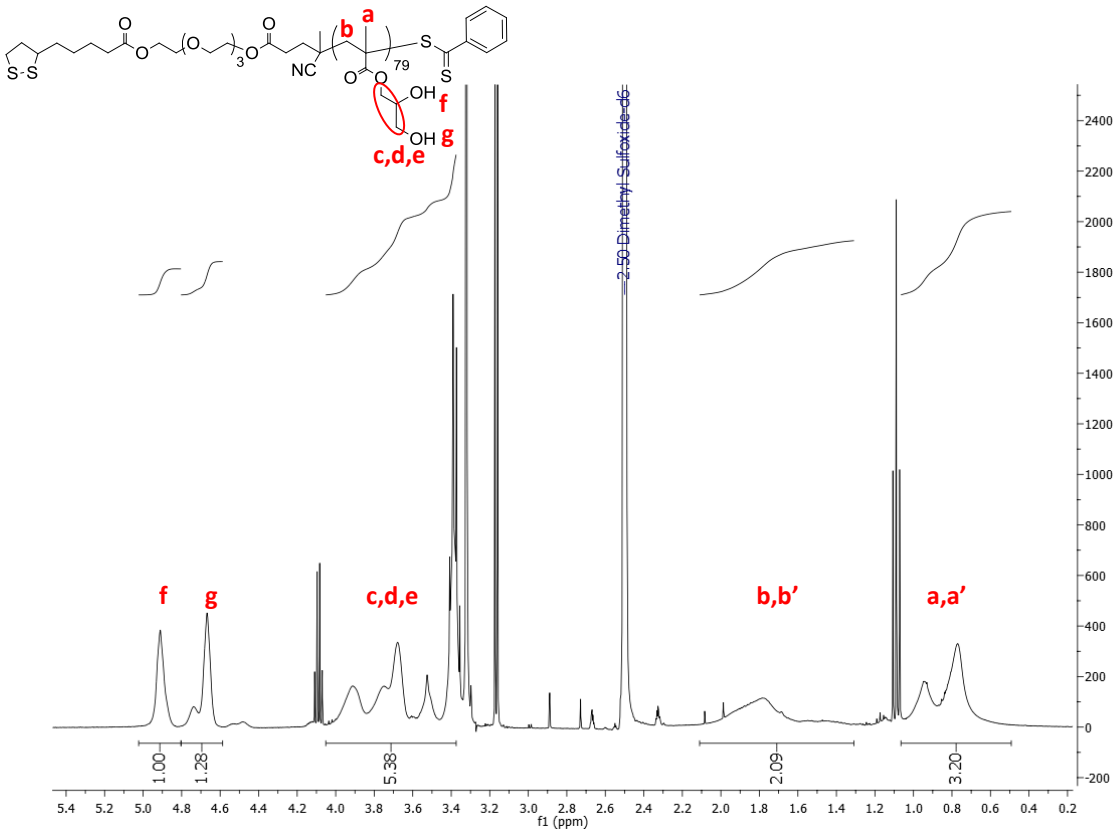

Figure 25. ^{1}H-NMR spectrum of poly(GMA) after precipitation, performed in DMSO-d_6 with peak assignment.

The GPC analysis revealed that the di-block copolymer possesses a PDI of 1.16, which confirm the very low molecular weight polydispersity and that the synthetic procedure ensure for a very controlled and homogenous polymer chain growth.

6.1.6. Removal of Thiocarbonylthio Group

The Thiocarbonylthio Group removal from polymers synthetized by RAFT technique is an important issue to prevent problems with reactivity and degradation into

malodorous sulfur-containing compounds[125]. Moreover the eventual formation of a thiol end-group could compete with the Lipoic termination of the polymer chain for the gold surface adsorption. This will lead to the production of particles decorated with poly(MCH-co-GMA) whose hydrophilic block poly(GMA) is directly conjugated to the GNP surface and the poly(MCH) block is exposed to the solvent. The hydrophilic poly(GMA) block provide for stealth properties, henceforth the loss of this external layer can induce the particle instability. Moreover the pH responsive block (poly(MCH)) exhibits a higher steric hindrance which could hinder the polymer chain adsorption on the particle surface. For all these reasons the cleavage of thiocarbonylthio group is paramount to ensure a correct polymer docking to the particle surface through the lipoic acid and the exposure of the hydrophilic block towards the bulk assuring the system stealthness.

The RAFT end-group removal reaction involves heating the polymer with a large excess (30 molar equivalents) of AIBN. Analysis of the end-group removed polymers can be achieved using traditional techniques such as NMR, when the RAFT agent signals are still detectable, and GPC. However, a reliable method is also UV-Vis spectroscopy of the polymer since the thiocarbonylthio chromophore absorbs strongly in the Visible range at 400-500 nm and this spectroscopic feature is unique for polymers possessing a RAFT end-group. Visual comparison of the colour of the polymer solution before and after end-group removal can also be used to confirm if the end-group has successfully been removed[125].

RAFT agent cleavage reaction was performed on poly(GMA) and poly(MCH-co-GMA). At the beginning of the reaction polymer solutions were red coloured whereas at the end-group removed polymers appeared discolored. The polymer was finally isolated by precipitation in diethyl ether-petroleum ether mixture.

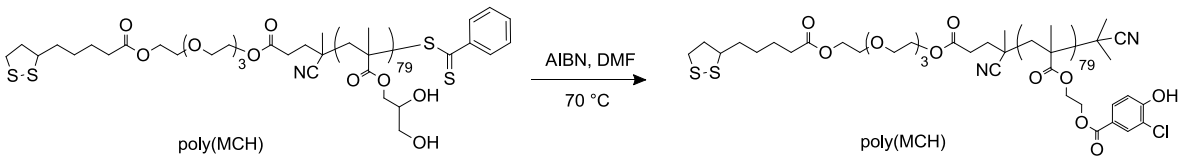

Scheme 7. RAFT agent cleavage reaction performed on poly(GMA).

6.1.7. Synthesis and characterization of targeting agent Folate-PEG-SH.

A targeting agent was synthesized for the delivery of particles to Folate receptor overexpressing cancer cells. In order to ensure proper exposure of the targeting moiety on the particle surface, folic acid was conjugated to a flexible and hydrophilic thiol terminating PEG linker. Two derivatives were synthesized provided of two different PEG lengths, 2 and 3.5 kDa, which have been combined on the surface of *Folate targeted pH responsive GNPs* and *Folate targeted GNPs* formulations respectively. Folate-PEG-SH synthesis was performed by adapting procedures reported in literature[126] (Figure 26.).

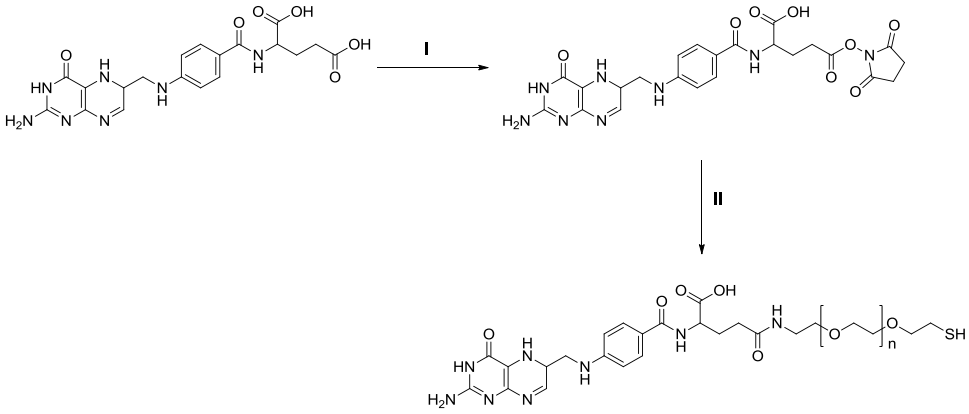

Figure 26. Synthesis of Folate-PEG conjugate – I. Activation of γ-COOH group of folic acid by NHS and DCC in anhydrous DMSO. II. Conjugation of NHS-Folate ester to NH_2-PEG-SH in anhydrous DMSO in presence of TEA as catalyst. n=45 kDa for FA-PEG_{2kDa}-SH synthesis, n= 79 for FA-$PEG_{3.5kDa}$-SH synthesis.

The conjugation efficiency of the purified product was determined by spectrophotometric methods. FA–PEG-SH was dissolved in milliQ water basified at pH 9 by addiction of ammonia and then diluted to 0.5 mg/mL in phosphate buffer, NaCl 150 mM, at pH 7.4. The UV absorption at 363 nm of the solution was measured to assess the Folate content considering the molar extinction coefficient of folic acid reported in literature (6197 mol^{-1} cm^{-1} in PBS buffer pH 7.4)[127]. The Iodine test performed on the FA–PEG-SH diluted solution in milli-Q water provided the PEG quantification based on a previously prepared calibration curve.

The conjugation efficiency was then calculated as follows:

% conjugation efficiency = (Abs. at 363 nm/6197 M^{-1} cm^{-1})/[PEG (mg/mL)]/(PEG MW (g/mol)) x 100

The conjugation yield of Folate to NH_2-PEG-SH was of 98% mol/mol underling that the conditions used for the synthesis allowed for the almost complete conjugation of the free amino groups of PEG with the carboxylic acid of folic acid. Notably, folic acid possesses two carboxylic groups: the one in α position is required for the biological activity. In order to limit the conjugation to the gamma carboxylic group, the reaction was performed with a low excess of NHS-activated Folate. In this condition it is reasonable that the reaction of the less hindered carboxylic group with NH_2-PEG-SH is favored. The literature reports that about 70% of the gamma carboxylic groups reacts with free amino groups thus most of the alpha carboxylic groups of the Folate are available for the binding to the Folate receptors[77,128].

The Ellman's test carried out on the pure product after the reduction with TCEP showed a percentage of free thiol groups of 96% mol/mol with respect to the theoretical percentage. The MALDI TOF mass spectrometry confirmed the chemical identity and provided a bell shaped profile centered at 2369 m/z (expected [M+H]= 2424 Da) for FA-PEG_{2kDa}-SH (Figure 27 - A) and 4137 m/z (expected [M+H]= 3924 Da) for FA-$PEG_{3.5kDa}$-SH (Figure 27 - B).

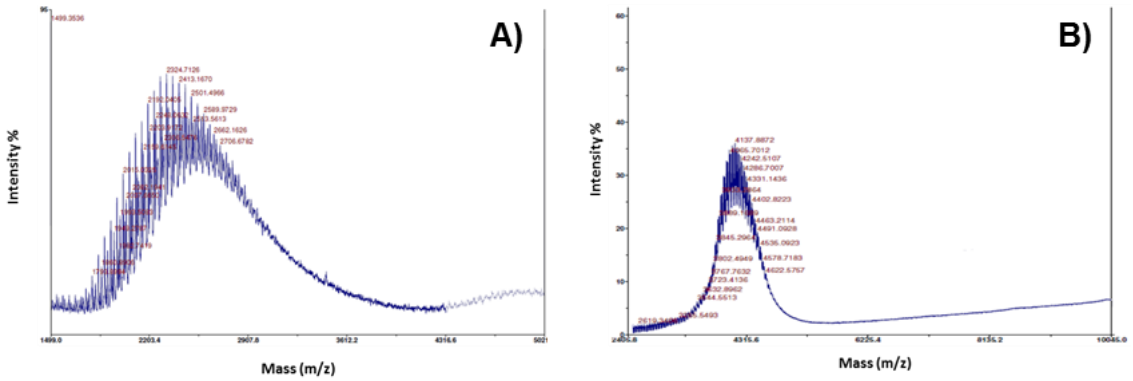

Figure 27. MALDI TOF analysis of (A) FA-PEG_{2kDa}-SH and (B) FA-$PEG_{3.5kDa}$-SH conjugate.

The reverse phase high-performance liquid chromatography analysis performed on both the Folate-PEG-SH conjugates showed no traces of free Folate, confirming the high degree of purity of the products.

6.1.8. Synthesis and characterization of Bodipy-PEG$_{2kDa}$-SH

Bodipy FL is a neutral dye with a good photostability, outstanding brightness, sharp emission peak and high quantum yield. It is insensitive to variations in pH thus it is a good candidate for the labelling of *Folate targeted pH responsive gold nanoparticles*.

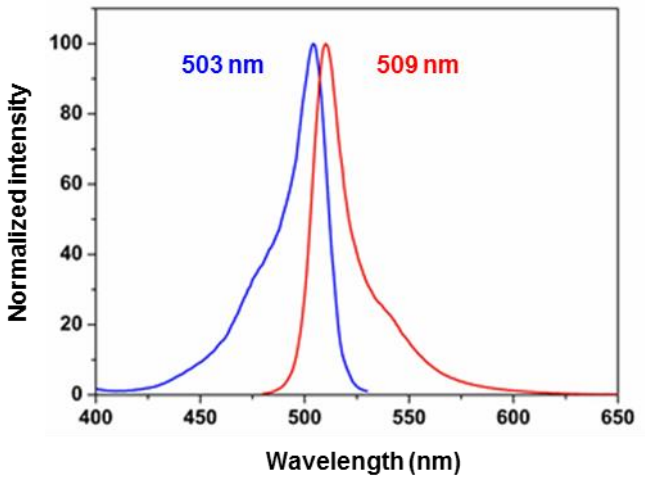

Figure 28. Normalized fluorescence excitation (—) and emission (—) spectra of Bodipy FL-NHS.

Bodipy FL was grafted to the particle surface through a PEG spacer of 2 kDa. The conjugation reaction was performed using N-hydroxysuccinimidyl-ester-activated Bodipy FL (1.2 equivalents) with respect to NH_2-PEG$_{2kDa}$-SH to promote a high derivatization of the PEG primary amino group (Scheme 8.).

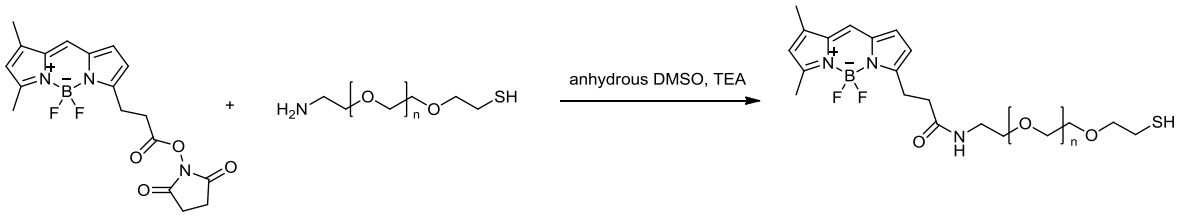

Scheme 8. Reaction scheme of Bodipy-NHS conjugation to NH_2-PEG$_{2kDa}$-SH .

The purification of the crude product was performed by size exclusion chromatography eluted in organic solvent. The column fractions were analyzed spectrophotometrically at 503 nm and 535 nm (Iodine test) for the Bodipy and PEG assessment, respectively. The gel filtration chromatogram, reported in Figure x, highlight the very good separation of the product and the unreacted Bodipy-NHS excess.

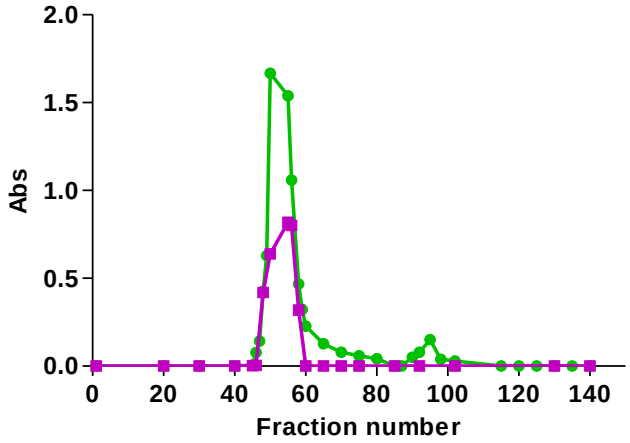

Figure 29. Gel filtration chromatographic profile of the conjugate Bodipy-PEG_{2kDa}-SH on Sephadex LH20 column, eluted with Ethanol. Fractions were analized by UV-Vis spectroscopy at 503 nm and Iodine assay (535 nm) for the Bodipy (●) and the PEG (■) determination respectively.

The purified product was lyophilized and analyzed by MALDI TOF mass spectrometry showing a bell shaped profile centered at 2227.6 m/z, expected [M+H] at 2276.12 Da (Figure 30 – B). The presence of oxidized product traces was highlighted by the mass analysis, justified by the dimerization of the starting material (Figure 30 – A). UV-Vis spectroscopic analysis performed on the purified Bodipy-PEG solution revealed a conjugation yield of 94% mol/mol, calculated as the molar ratio between the Bodipy and the PEG content.

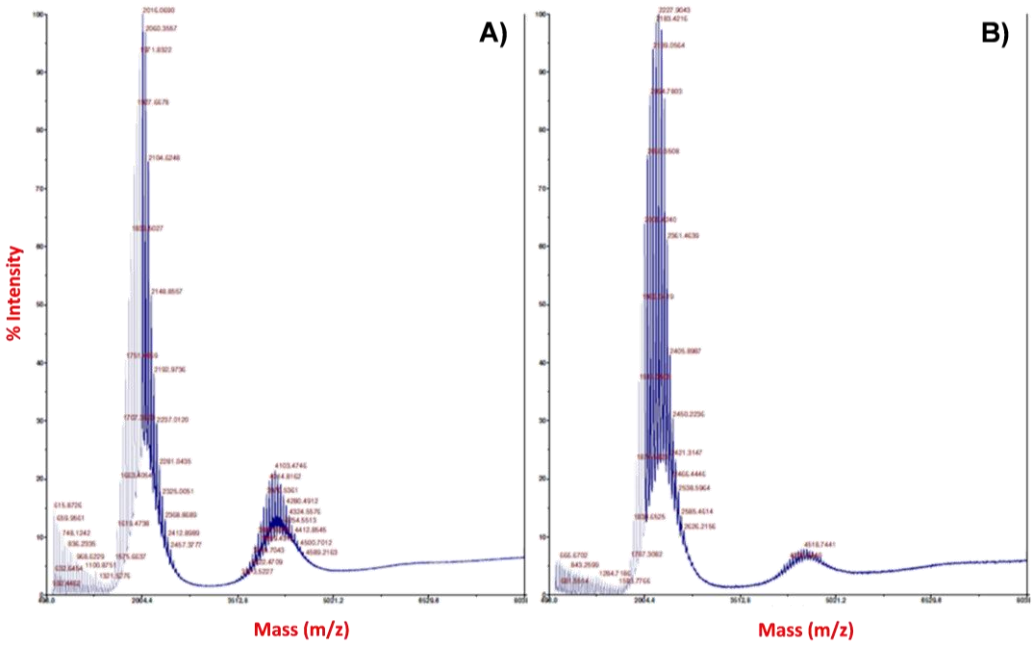

Figure 30. MALDI TOF analysis of $mPEG_{2kDa}$-SH starting material (A) and of the Bodipy-PEG_{2kDa}-SH conjugate (B).

6.1.9. Synthesis and characterization of Rho-PEG$_{2kDa}$-SH

Rho-PEG$_{2kDa}$-SH was synthetized as labelling agent to track the cell uptake of *Folate targeted Rhodamine labelled gold nanoparticles*. Rhodamine-NHS was conjugated to NH_2-PEG$_{2kDa}$-SH via amide bond (Scheme 9.).

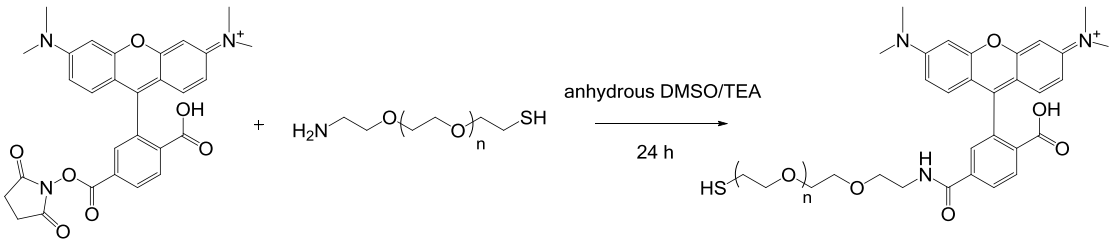

Scheme 9. Reaction scheme of Rhodamine-NHS conjugation to NH_2-PEG$_{2kDa}$-SH .

The crude product Rho-PEG$_{2kDa}$-SH, recovered from the reaction mixture by precipitation in diethyl ether and was purified by size exclusion chromatography to remove excess of unreacted Rhodamine-NHS.

The Rho-PEG$_{2kDa}$-SH was dissolved in water and analyzed by UV-Vis spectroscopy at 552 nm, to assess the Rhodamine concentration based on a previously prepared calibration curve, and by the Iodine test to derive the PEG concentration. The conjugation efficiency, obtained as the ratio between the Rhodamine and the PEG concentration, was 96% mol/mol.

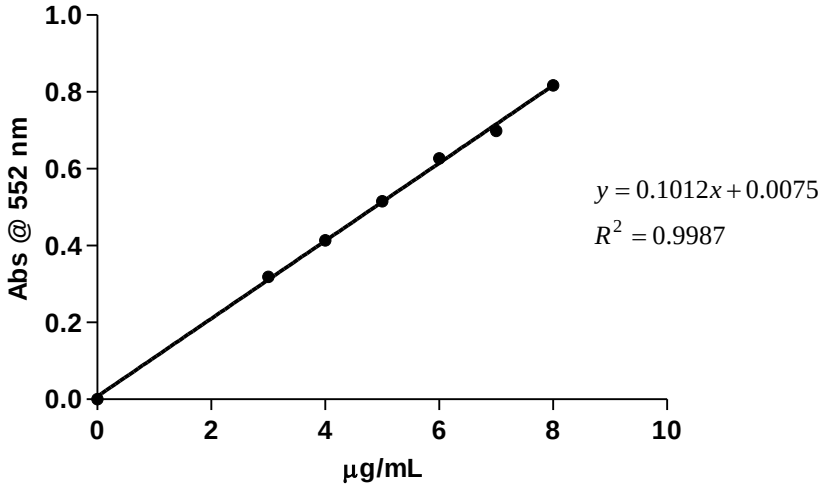

Figure 31. Calibration curve of Rhodamine-NHS in milliQ water at 552 nm.

The derivative was further characterized by ^{1}H NMR spectroscopy and MALDI TOF mass spectrometry. The MALDI TOF analysis of the Rho-PEG_{2kDa}-SH conjugated (Figure 32.) showed a bell shaped profile centered at 2662.4 m/z (expected 2429 u.m.a.), while no trace of unreacted mPEG-SH (MALDI TOF mass signal at 2016.2 m/z) was found.

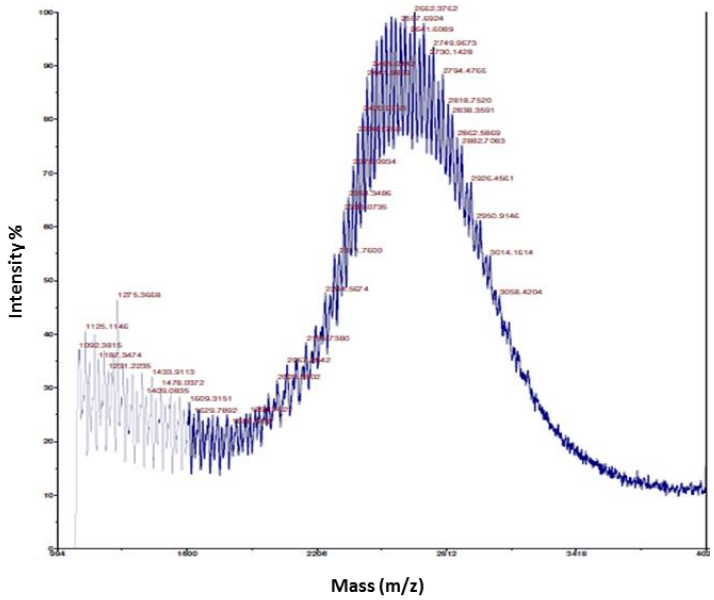

Figure 32. MALDI TOF analysis of Rho-PEG_{2kDa}-SH conjugate.

6.1.10. Synthesis and characterization of Folate-Cadaverine-Rhodamine (FA-C_5-Rho).

Several studies reported in literature highlight that the introduction of multiple targeting ligands onto nanoparticle surface can increase binding avidity, rate of internalization and so improve the therapeutic efficacy. In light of this will be suitable to determine whether an optimal ligand density exists.

In the present work we developed *Folate targeted gold nanoparticle* at differing ligand densities. Particles were fluorescently labelled with Rhodamine-PEG_{2kDa}-SH (500 chains per particle). Moreover in order to investigate the potential effect that multivalency could have on the internalization pathway, monovalent Folate ligand was synthetized and labelled with Rhodamine using Cadaverine as spacer.

The Folate-Cadaverine-Rhodamine synthesis was performed according to a twostep procedure. First, Folic acid was activated to N-Hydroxysuccinimidyl-ester (Scheme 10 – I) and then conjugated to Cadaverine (Scheme 10 – II).

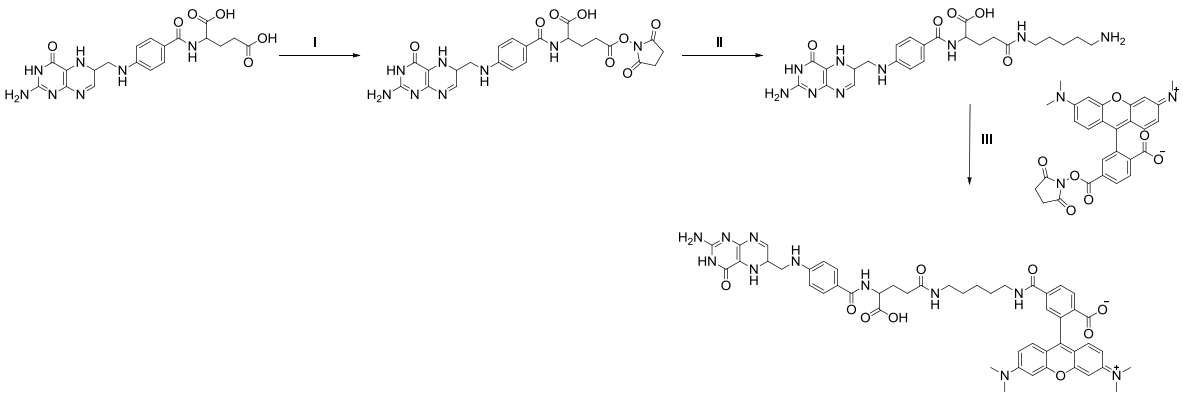

Scheme 10. Reaction scheme of FA-C_5-Rho. - I. Folic acid activation to N-Hydroxysuccinimidyl-ester. – II. Folate-NHS conjugation to Cadaverine. – III. Conjugation of Rhodamine-NHS to Folate-Cadaverine.

The Folate-Cadaverine was isolated by precipitation in diethyl ether in order to eliminate the excess of Cadaverine that, on the contrary of Folic acid, is soluble in ether. The dried product was then characterized by ESI-TOF mass spectrometry, confirming the chemical identity of the product: expected a signal at 527.26 u.m.a for [M+H], found [M+H]=527.25 u.m.a. and $[M+2H]^{2+}$=218.15 u.m.a. (Figure 33.).

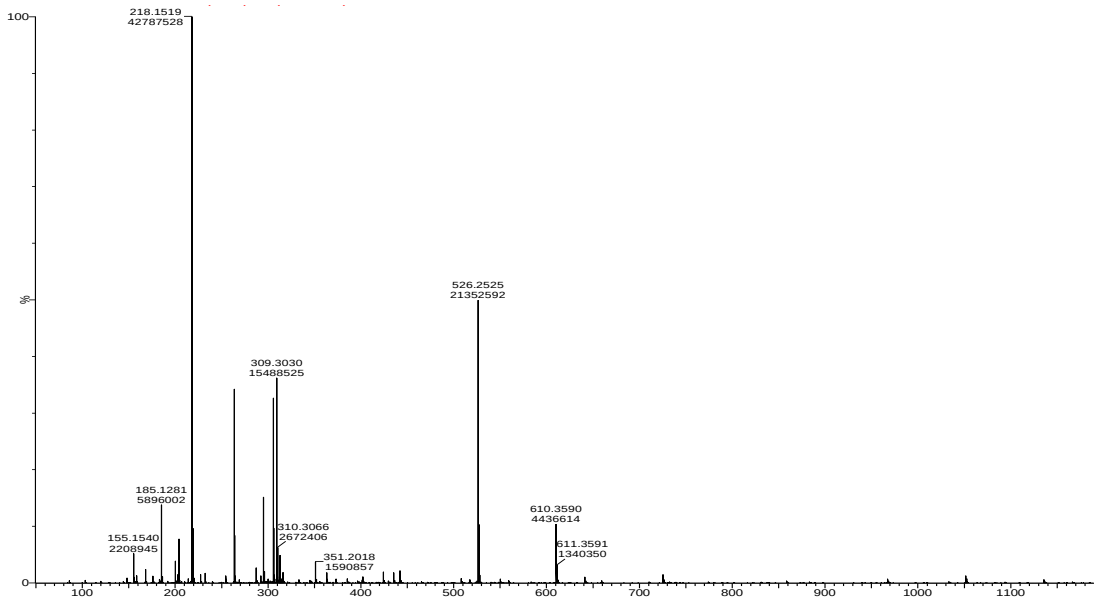

Figure 33. ESI TOF spectrum of Folate-Cadaverine.

In the second step, Rhodamine-NHS was conjugated to the amino end-group of Folate-Cadaverine through the formation of an amide bond using a molar excess of Rhodamine-NHS of 1.2 equivalents with respect to Folate-Cadaverine in order to

promote the conjugation reaction. The crude product was purified by the unreacted Rhodamine by size exclusion chromatography. The chemical identity of the final product FA-C_5-Rho was confirmed by ESI-TOF mass spectrometry (expected 940.41 u.m.a for [M+H], found 464.21 for $[M-2H]^{2-}$.

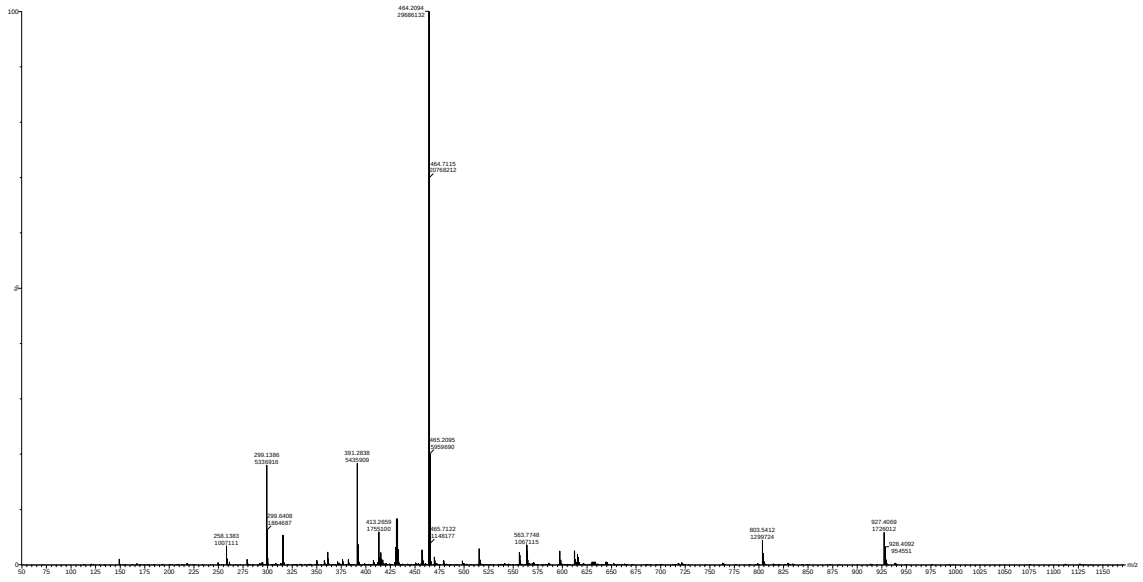

Figure 34. ESI TOF spectrum of Folate-Cadaverine-Rhodamine.

6.2. GOLD NANOPATICLE PRODUCTION AND CHARACTERIZATION

Nanoparticles were generated by reduction of Tetrachloroauric(III) acid ($HAuCl_4$) with sodium citrate according to the Turkevich's method introduced in 1951 that consists in the reduction of $HAuCl_4$ by citrate. Citrate was used as reducing agent and stabilizing agent since it remains adsorbed on particle surface providing negative repulsive charges[94]. The presence of citrate prevents aggregation of the formed gold (Au) solution which would take place as a consequence of attractive Van der Waals and depletion forces[13]. The $HAuCl_4$ solution was brought to 75 °C and trisodium citrate dihydrate was quickly added under vigorous stirring. Before the addition of the reducing agent, gold is in solution in the cationic Au(III) oxidation state. The average diameter of the colloidal gold resulting from reduction can be tuned in the range of 10-100 nm by varying the citrate/Au ratio. A low amount of sodium citrate allows to achieve the formation of a low number of nucleation seeds and provides limited citrate ions available for the stabilization of the particles. This will lead to the aggregation of small particles into bigger ones until the total surface area of all

particles will be coated by the available citrate ions. When the reducing agent is added, metallic gold atoms are generated in the solution, and their concentration rises rapidly until the solution exceeds saturation. This process was visible by the rapid color change from pale-yellow to grey, which corresponds to the gold "nuclei" formation. After few minutes, a wine-red colloidal gold suspension was obtained. GNPs were characterized by DLS (Figure 35 – A) showing a size of 14.5±1.6 nm, based on the size distribution expressed by Number, and a polydispersity index (PDI) of 0.20±0.08. TEM analysis confirmed that the method for the GNP preparation results in homogenous populations of spherical particles (Figure 35 – C). TEM images (n=200), analyzed by ImageJ open source image processing program showed a size of 14.6±2.3 nm (Figure 35 – C') which was in perfect agreement with the data provided by the DLS analysis.

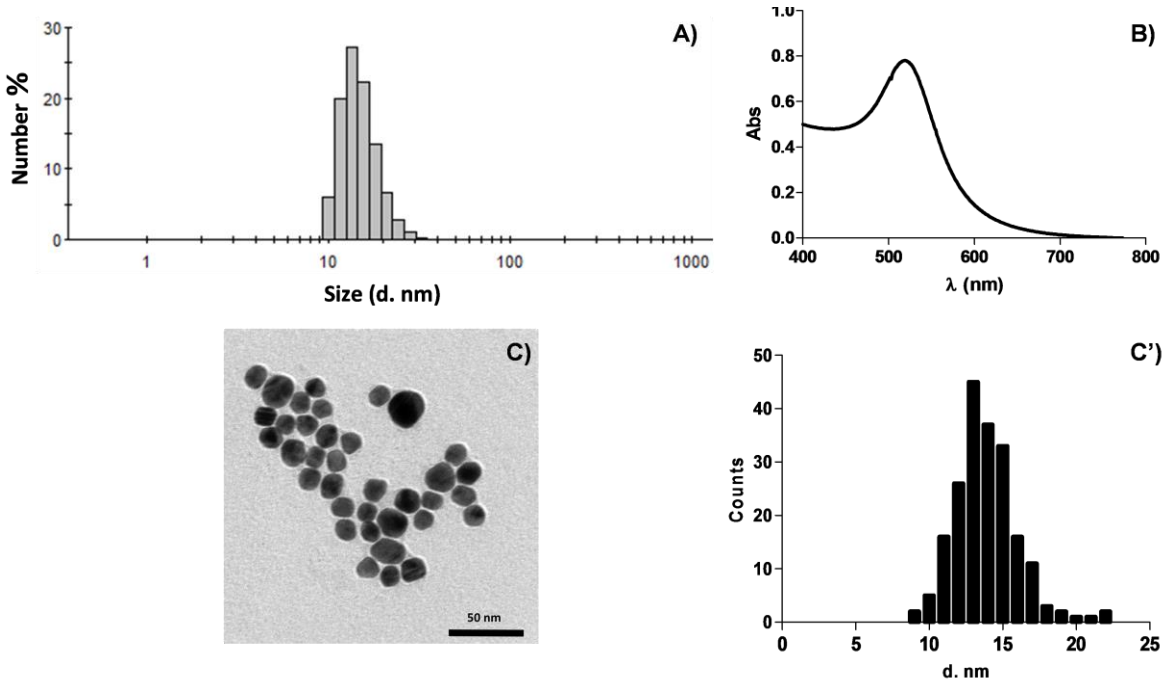

Figure 35. (A) Dynamic Light Scattering, (B) UV-Vis spectrum and (C) TEM analysis of citrate stabilized gold nanoparticles freshly prepared by Turkevich's method. (C') Size distribution profile of particles obtained by the elaboration of TEM images by ImageJ image processing program.

A revision of the Mie theory and the study reported by El-Sayed and co-workers was published by Liu et Co. in 2006[118]. In their work they underlined a linear correlation of the double logarithm of the extinction coefficient of gold nanoparticle aqueous suspensions versus the particle diameter. This concept is mathematically expressed

by equation (2), where ε_{506} is the molar extinction coefficient (M^{-1} cm^{-1}) referred to the absorbance at 506 nm, D is the core diameter of the nanoparticles, k and a are two constants whose values are 3.32111 and 10.80505 respectively.

$$(2) \quad \ln \varepsilon = k \ln D + a$$

In order to assess the concentration of particle samples prepared in this thesis work, the extinction coefficient of each formulation was derived by Eq. (2) in agreement with what has been reported by El-Sayed and Mie[119,120]. The gold nanoparticles concentration (M) was determined using the Lambert–Beer law, equation (3), where A_{506} is the absorbance at 506 nm and b is the path length.

$$(3) \quad Conc.\,(\mathrm{M}) = A_{506} / \varepsilon_{506} b$$

The final concentration of the citrate stabilized GNP suspension was of about 3 nM for the different formulation batches.

Spherical gold nanoparticles synthesized through the Turkevich's method show an overall negative surface charge which is ascribed to the presence of the surface adsorbed citrate layer. Citrate anions, act both as reducing and stabilizing agent that allow for facile, efficient and high-density ligand exchange. Notably gold and citrate interact with a bond strength comparable to the hydrogen bond and it can thus be easily displaced by ligands providing for stronger bonds such as thiols or disulphides. The Gold-Sulfur bond (Au–S) is fairly strong (45 kcal/mol) and results from the soft atom characteristics of both Au and S[13]. Gold nanoparticles were decorated with stabilizing polymers (namely PEG), responsive polymers for environmental sensing and biomolecules to provide for biorecognition and targeting. To this aim, functional polymers were selected with a thiol ending group to allow a straightforward decoration of the gold nanoparticle surface.

6.3. FOLATE TARGETED GOLD NANOPARTICLES AS ULTRASOUND SENSITIZERS FOR ANTICANCER TREATMENT

In recent decades Sonodynamic therapy (SDT) has received great attention by the researchers because of its excellent application prospects in the treatment of cancer. It is a non-invasive approach based on acoustic cavitation generated by ultrasound which lead to cytotoxic effects on tumor cells by producing reactive oxygen species (ROS), able to generate irreversible damage of the tissues[17]. Ultrasound can be precisely applied in a limited focal zone and the penetration depth can be selected by tuning the frequency. As described by Tuziuti *et al.*, the presence of particles in a liquid creates nucleation sites that participate in the formation of cavities to reduce the threshold intensity needed for the cavitation process[129]. This leads to a great enhancement of the sonodynamic treatment efficacy.

The most used sonosensitizers are porphyrins and their derivatives. Even if very efficient, many of these agents suffer of physico-chemical problems, such as low solubility, instability after intravenous injection, uncontrolled biodistribution, which limit their clinical application. In this scenario, gold nanoparticles have emerged as promising nanosensitizers in sonodynamic therapy. In virtue of their intriguing physical properties, gold nanoparticles were found to accelerate the cavitation phenomena under acoustic tension resulting in enhancement of both mechanical bio-effects and the amplitude of acoustic emissions. Moreover, gold nanoparticles are biocompatible carriers which, thanks to the high surface-to-volume ratio, can be additionally decorated with cancer-specific biomarkers allowing for a site-specific accumulation. Notably, the nanoparticle dimensions are suitable for the exploitation of the EPR effect that yields enhanced accumulation in the tumor tissue thus minimizing potential off-site effects.

6.3.1. Aim of the study

The aim of the colloidal gold formulation discussed in this chapter was to investigate in depth the therapeutic potentials of ultrasound irradiation on cancer cells pre-incubated with targeted gold nanoparticles. To this aim, gold nanoparticle surface was decorated with Folate-$PEG_{3.5kDa}$-SH, selected as targeting agent for the biorecognition of Folate receptor overexpressing cancer cells. The effect of targeting

ligand surface density on the particle uptake efficiency was thoroughly studied together with the cell killing effect of pulsed or continuous ultrasounds. This study intends to provide a proof-of-concept for the exploitation of targeted gold nanoparticles as site-selective sensitizers for ultrasound-triggered cancer cell killing (Figure 36.). Unlike previous literature reports, we aim here to induce cancer cell killing by the sole combination of gold nanoparticles and ultrasound irradiation without the aid of sonosensitizers such as porphyrin derivatives[130] or the use of intense pulsed light[129].

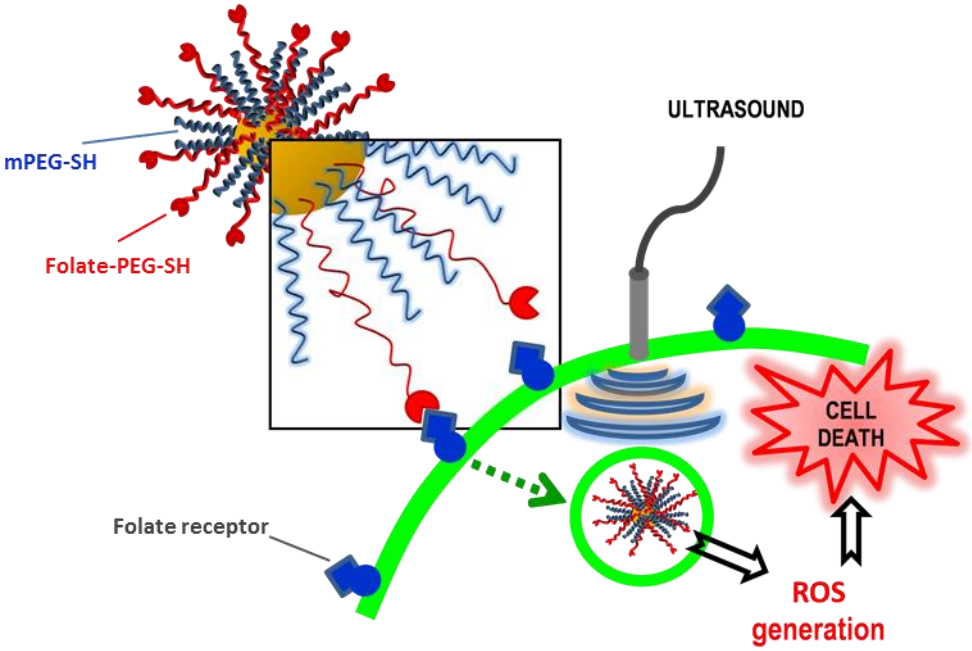

Figure 36. Schematic representation of selective uptake of Folate targeted gold nanoparticles mediated by the Folate receptor biorecognition. The active targeting mediated GNP accumulation enhances the efficacy of the sonodynamic therapy

6.3.2. Assessment of GNP surface decoration efficiency

GNPs were modified with increasing molar excesses (1:500, 1:1000, 1:2000, 1:3000 and 1:6000 GNP/polymer molar ratio) of $mPEG_{2kDa}$-SH and FA-$PEG_{3.5kDa}$-SH in order evaluate the decoration efficiency of each of the two polymeric components. Reference samples containing equimolar polymer concentrations without colloidal gold were prepared by replacing the particle volume with milliQ water.

After incubation, gold nanoparticles were isolated by centrifugation. The conjugated polymer on the GNP surface was derived by difference between the concentration of

unbound polymer in the supernatant and that of the corresponding reference sample. This allowed to assess the conjugation efficiency for each incremental polymer excess incubated with the particle samples. Based on the particle surface area, estimated to be 707 nm^2 for 15 nm GNPs, the density of polymer chains per nm^2 was also calculated (Figure 37.).

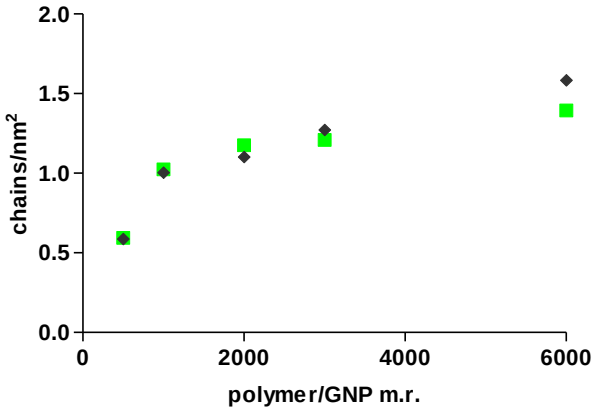

Figure 37. $mPEG_{2kDa}$-SH (■) and FA-$PEG_{3.5kDa}$-SH (■) density on particle surface at increasing polymer feed.

The functionalization profile of GNPs with both polymers tested showed to plateauing at a polymer/GNP molar ratio above 3000:1. The two polymers associate to the particle surface with an overlapping profile. The gyration radius and the distance of the anchorage site are crucial parameters which dictate the chains conformation. At the maximum density achieved, the distance among chains is minimized and the polymer is forced to assume a "brush-like" conformation. In contrast, at low polymer density, chains are organized in "mushroom-like" structures. Studies reported in literature demonstrated that the optimal surface coverage is the particular condition between the "mushroom" and "brush" configurations: polymer chains are in a slightly confined configuration which guarantee no uncoated areas on the particle surface and sufficient flexibility of the chains to generate a soft and protein repelling layer that minimize the opsonization process[131].

Table I. reports in details the conjugation yield percentages that were assessed for each sample. The functionalization yield, as expected, decreases with the increase of the polymer molar excess. In fact, at low molar excess the competition between polymer chains for the gold surface adsorption is negligible: the whole particle surface is available for the polymer attachment through the thiol group. As the polymer density increases on the particle surface, the adsorbed chains rearrange from flat "mushroom-like" to "brush-like". The surface saturation is set by the polymer features, in particular the gyration radius of the polymer chain and its hydrodynamic size. Under the fully brush-like conformation, the polymer molecules are so tightly packed that the sliding of additional polymer chains is prohibited. Henceforth the conjugation yield falls significantly.

Table I. Conjugation yield of $mPEG_{2kDa}$-SH and FA-$PEG_{3.5kDa}$-SH to GNP surface at increasing polymer feed ratios.

GNP/polymer molar ratio in feed	**Conjugation yield of $mPEG_{2kDa}$-SH (%)**	**Conjugation yield of FA-$PEG_{3.5kDa}$-SH (%)**
1:500	83	84
1:1000	71	72
1:2000	39	42
1:3000	30	28
1:6000	19	16

The functionalization profile of GNPs with Folate-$PEG_{3.5kDa}$-SH or $mPEG_{2kDa}$-SH yielded a very similar maximum polymer chain density of 1.39 and 1.58 chains/nm^2, respectively. This result can be ascribed to the comparable hydrodynamic size of Folate-$PEG_{3.5kDa}$-SH and $mPEG_{2kDa}$-SH.

Overall we concluded that, under the conditions and the particle concentration used, a PEG-SH/GNP molar ratio below 500:1 allows both thiolated PEGs to quantitatively conjugate on the particle surface.

6.3.3. Folate targeted gold nanoparticle preparation and characterization

Folate targeted GNPs were obtained by a dual step method. In the first step gold nanoparticles were decorated with Folate-$PEG_{3.5kDa}$-SH by incubating particles with different molar excess of Folate-PEG-SH (0 to 100-fold excesses) with respect to GNP in order to generate particles at different targeting agent density. The amount of conjugated Folate-$PEG_{3.5kDa}$-SH was estimated by UV-Vis spectrophotometric analysis and Iodine test of the medium after particle isolation, which confirmed the high efficiency of the conjugation procedure (above 98 % conjugation efficiency for all the formulations prepared). This was expected based on preliminary tests reported in Chapter 6.3.2 based on the information included in Table I. The particle surface was then saturated with a 4000 $mPEG_{2kDa}$-SH molar excess to endow stealth properties while ensuring exposure of the targeting agent. *Folate targeted GNPs* were then recovered by centrifugation and characterized. The $mPEG_{2kDa}$-SH feed ratio used allowed to generate particle decorated with an average polymer density of 0.99 chains/nm^2 (700 chains/GNP) The presence of Folate-$PEG_{3.5kDa}$-SH on the particle surface slightly decresed the $mPEG_{2kDa}$-SH adsorption efficiency.
By using this formulation strategy, we prepared *Folate targeted gold nanoparticles* at 4 different Folate-$PEG_{3.5kDa}$-SH density in order to select the formulation with higher targeting capacity toward FR overexpressing cancer cells. The polymeric composition of each GNP formulation is reported in Table II.

Table II. Coating composition of Folate targeted GNP formulations.

GNPs formulation	N° of FA-$PEG_{3.5kDa}$-SH chains/GNP	N° of $mPEG_{2Da}$ -SH chains/GNP
PEG-GNPs	0	700
10x FA-PEG-GNPs	10	690
25x FA-PEG-GNPs	25	675
50x FA-PEG-GNPs	50	650
100x FA-PEG-GNPs	100	600

The particle distribution profiles obtained by Dynamic light scattering analysis showed a significant increase of the hydrodynamic size of surface decorated particles with respect of naked ones (Figure 38 – A). In particular *Folate targeted particles*,

regardless of the density of Folate-$PEG_{3.5kDa}$-SH, displayed a size of about 28 nm (28.1±5.2 nm for the GNPs coated with 50 chains of Folate-$PEG_{3.5kDa}$-SH and 650 chains of $mPEG_{2kDa}$-SH) and a narrow PDI of 0.297. The sample size homogeneity was confirmed by TEM analysis which highlighted also a good particle stability reflected in the absence of particles aggregates (Figure38 – B). The analysis of the TEM images by ImageJ software allowed to derive the mean diameter of 34.4±2.7nm of the different formulations.

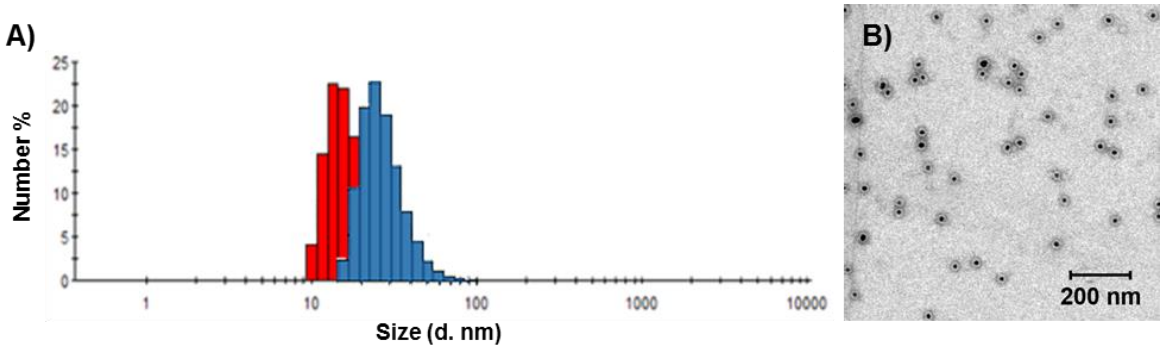

Figure 38. (A) Dynamic Light Scattering profile of naked GNPs (■) and Folate targeted GNPs (■) in milliQ water. (B) Representative TEM image of 50x FA-PEG-GNPs dispersed in milliQ water.

Furthermore, the TEM images clearly show that the particle core (black dots on Figure 38 – B) possesses a grey less dense corona confirming the homogeneous polymer decoration of the colloidal gold.

Finally the particle concentration of each formulation was derived by combining the UV-Vis spectroscopic (Figure 39.) and DLS analysis. While the freshly prepared naked particles possess a concentration of about 3 nM, decorated particles isolated by centrifugation showed a concentration of about 35 nM, 15-fold higher compared to the naked ones.

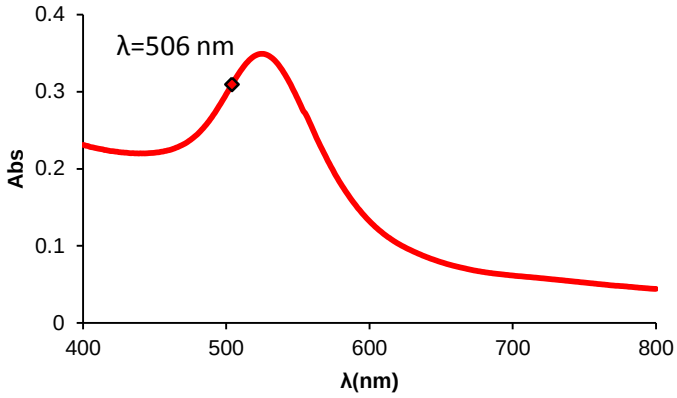

Figure 39. UV-Vis spectrum of Folate targeted GNPs in milliQ water.

6.3.4. CELL UPTAKE QUANTIFICATION BY ATOMIC ABSORPTION SPECTROSCOPY.

Cell uptake study was performed on KB cells, that overexpress the Folate receptor, and control MCF-7 cell line that does not express the Folate receptor on the cell membrane[132]. The particle uptake by KB and MCF-7 cells was quantified by Atomic adsorption spectroscopy (Figure 40.) on the basis of the average particle volume by assuming a sphere shape of the particles (calculated to be 1767.1 nm^3), the atomic gold cell volume and the number of cells in each sample (derived by BCA assay).

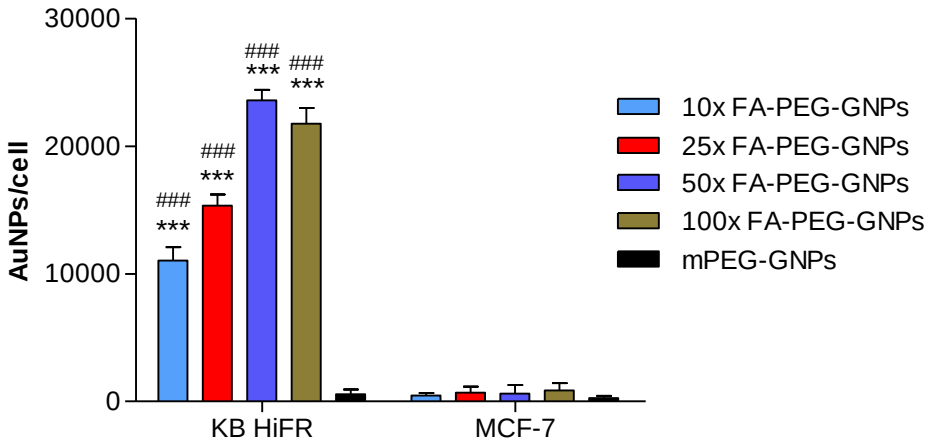

Figure 40. Cell uptake profile of gold nanoparticles decorated with different Folate-$PEG_{3.5kDa}$-SH densities (10x, 25x, 50x and 100x FA-PEG-GNPs) and non-targeted particles (mPEG-GNPs) obtained by Atomic adsorption analysis. Cell internalization study was performed on KB and MCF-7 cell lines. Statistical significance was calculated either versus non targeted particles (*** $p<0.001$) or FR non expressing MCF-7 cell line (### $p<0.001$).

The increase of the ligand density on the nanoparticle surface resulted in increased internalization efficiency of *Folate targeted GNPs* by the KB cells, up to saturation which was achieved with the formulation with 50 chains of FA-PEG-SH per particle. In fact, even increasing the FA-PEG-SH amount up to 100 chains/GNP, no significant increase in the particle uptake was noticed. The observed plateau in cell internalisation at higher ligand density than 50 unit/GNP may arise from the saturation of Folate receptors at the cell surface. Beyond this Folate density, the maximum number of receptor interactions occurs and the rate of particle internalisation approaches the maximum rate allowed by the uptake cellular process[133].

Notably, while only 570 non-targeted particles were found per cells, the presence of the targeting agent on the particles surface induced an uptake increase up 40 times compared to the uptake of mPEG-GNPs.

The unspecific particle association with cells was evaluated by testing the uptake of *Folate targeted GNPs* with MCF-7 cells that were used as control. A negligible uptake was shown by all the *Folate targeted GNP* formulations. A very limited internalization was also observed for non-targeted particles (mPEG-GNPs) by both KB and MCF-7 cell lines confirming the selectivity of the uptake that is mediated by the Folate receptor.

To further confirm the high selectivity of the particle internalization, a cell competition assay was performed with KB cells. The presence of free Folate in the cell incubation medium containing the *Folate targeted GNP* significantly inhibited the *Folate targeted GNP* internalization (7-fold decrease) showing that the competition with the targeted GNPs occurs for the binding to the cellular Folate receptor (Figure 41.).

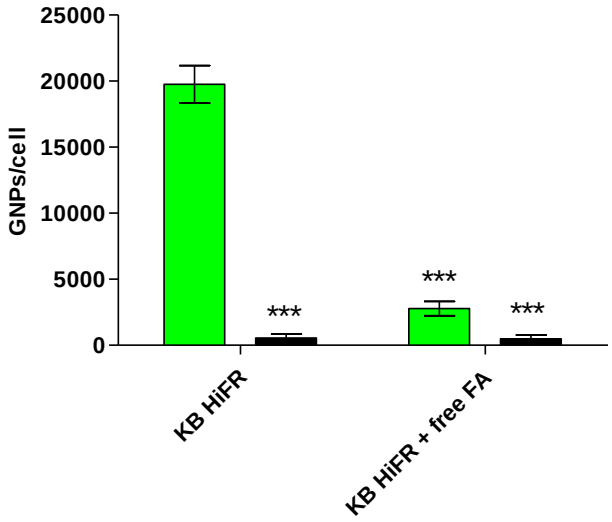

Figure 41. Competition assay profile: 50x FA-PEG-GNPs (■) and mPEG-GNPs (■) were incubated with KB cells in the presence (KB HiFR + free FA) or not (KB HiFR) of free Folate. Statistical significance was calculated versus 50x FA-PEG-GNPs incubated with KB HiFR: *** $p<0.001$.

6.3.5. TRANSMISSION ELECTRON MICROSCOPY ON KB CELLS

TEM images of slices of KB cells incubated with *Folate targeted GNPs* showed that the endocytosed particles are associated to intracellular vesicles that originate from the plasma membrane (Figure 42 – A, A'). Notably, particles are not aggregated even in the subcellular compartments showing that their colloidal stability is preserved throughout the endocytosis process without clustering and no single particle was significantly detectable in the cytosol. The latter event can be ascribed to negligible diffusion of particles across cell membrane. Control non-targeted particles (mPEG-GNPs) incubated with KB cells were not detectable in the cytosols confirming that these particles were not taken up as shown in Figure 42- B, B'.

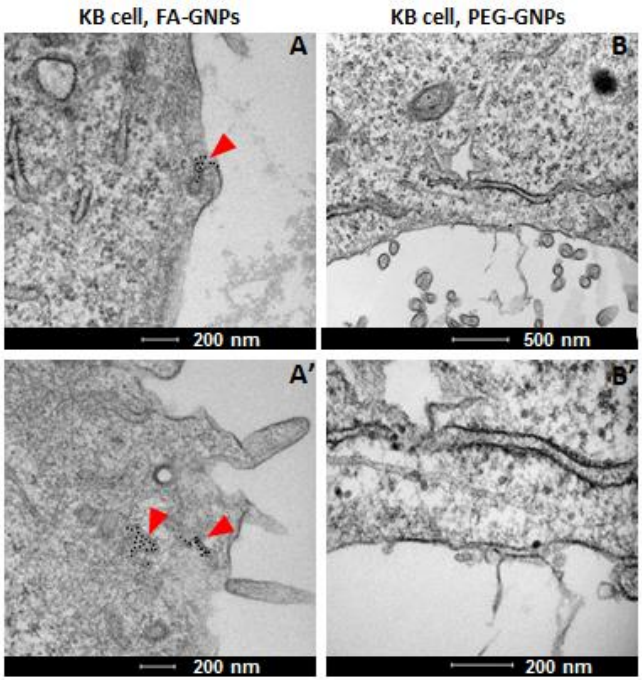

Figure 42. Representative TEM images of KB cells incubated with 50x FA-PEG-GNPs (A, A') and non-targeted particles (B, B'). 50x FA-PEG-GNPs are entrapped into vesicles (red arrows), while no mPEG-GNPs were found inside of the cells.

The cell uptake study of Folate targeted gold nanoparticles modified with increasing Folate-PEG-SH molar ratio highlighted that 50 chains of Folate-PEG-SH per particle ensure the maximum particle internalization by KB cells. For this reason, 50x FA-PEG-GNPs were selected as ideal formulation for further studies to evaluate if targeted gold nanoparticles can improve the efficacy of the sonodynamic treatment.

6.3.6. Sonodynamic treatment

KB and MCF-7 cells were incubated for 2 hours with *Folate targeted GNPs* coated with 50 Folate-PEG-SH chains to allow the particle uptake, and then irradiated with 1.8 MHz continuous ultrasound (US) at an energy density of 0.008 mJ/cm^2 for 5 minutes. The viability of KB and MCF-7 cells was assessed. As shown in Figure 43 – A, the sonodynamic treatment on KB cells after incubation with FA-PEG-GNPs (FA-PEG-GNPs + US) significantly decreased the KB cell growth rate at 24 (* $p<0.05$), 48 (*** $p<0.001$) and 72 hours (*** $p<0.001$). On the contrary, neither ultrasound (US) nor FA-PEG-GNPs (GNPs) nor mPEG-GNPs alone affect cell growth compared to untreated cells (Ctrl). Noteworthy, ultrasound treatment associated to the pre-contact with non-

targeted particles showed no effect on cell grown, further confirming that the increased ultrasound effect results from the particle uptake mediated by the Folate receptor. The sonodynamic treatment of MCF-7 cells (Figure 43 – B), which do not express the Folate receptor, with either FA-PEG-GNPs (FA-PEG-GNPs + US) or mPEG-GNPs (mPEG-GNPs + US) did not affect cell growth. Similar growth rate was observed when cells were treated with ultrasound, FA-PEG-GNPs or mPEG-GNPs alone.

These results emphasize the safety of US treatment alone and the biocompatibility of the GNP samples. The KB cell growth rate decrease was observed only for the combination of US and *Folate targeted GNPs*, confirming that gold nanoparticles act as nano-sonosensitizers and are selectively taken up by Folate receptor expressing cells. In contrast, no effect was shown by non-targeted particles, even in association to US treatment, confirming the selective particle internalization. To further confirm that the KB cell growth rate decrease upon sonodynamic treatment was due to sensitizing effect of the endocytosed targeted gold nanoparticles, cell uptake competition assay was performed under the same conditions generating the results reported in Figure 43 – A'). Notably, ultrasound exposure of KB cells after co-incubation with free Folate (US + FA) and FA-PEG-GNPs (FA-PEG-GNPs + US + FA) did not induced a significant decrease of cell growth.

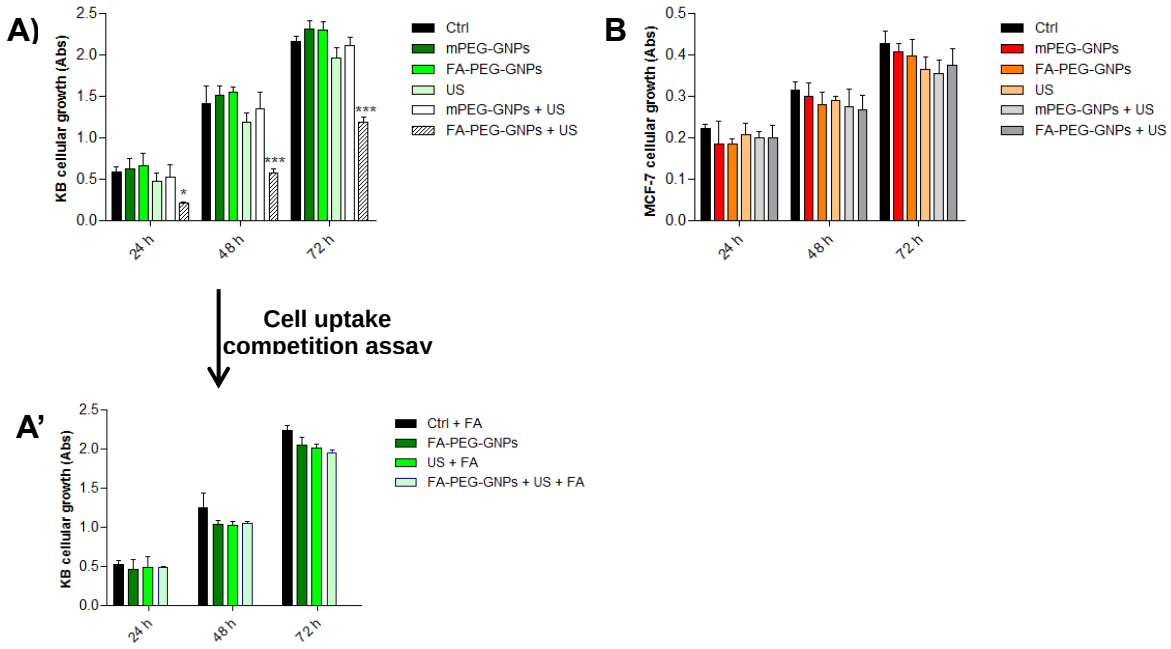

Figure 43. Effect of different treatment conditions on KB (A) and MCF-7 (B) cell proliferation as a function of time. Cells were treated with ultrasound, Folate-PEG-GNPs, non-targeted GNPs alone or the combination of US and the different GNP formulations. (A') Effect on KB cell growth of sonodynamic treatment upon incubation with FA-PEG-GNPs (GNPs + US) in presence of free Folate (FA) as competitive agent. Statistically significant difference versus untreated cells: * $p<0.05$; *** $p < 0.001$.

Moreover, flow cytometric analysis showed a significant increase of late apoptotic/necrotic cells when KB cells were treated sequentially with FA-PEG-GNPs and US. A different pattern of ROS production was also observed with respect to untreated cells and cells receiving either of the two treatments (Figure 44.). Notably, the cell population in the late apoptosis was almost 5 times higher with respect to controls.

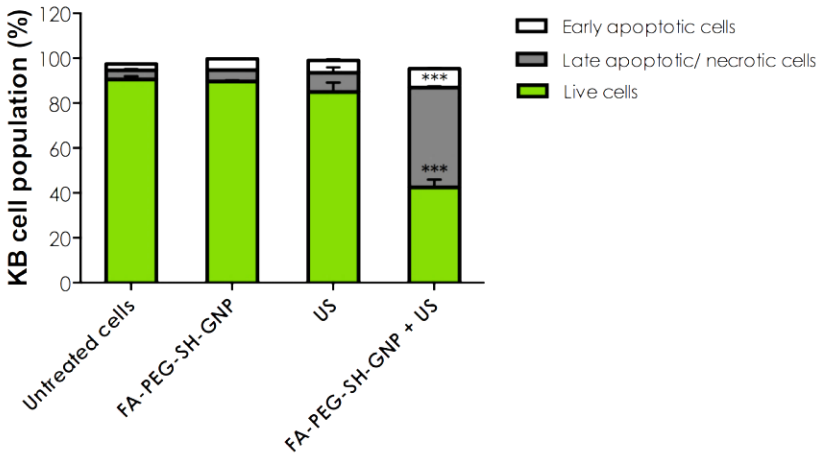

Figure 44. KB Cell death analysis after treatment with US or Folate targeted GNPs or in combination. Cell samples were analyzed by flow cytometry.

Overall, the evidences showed that the simultaneous exploitation of the targeting capacity of the gold nanoparticles and their sensitizing effect upon external physical stimuli (ultrasound) allow to achieve a site-specific physical treatment of cancer cells. Gold nanoparticles were shown to be a potent tool for cancer cell killing. The use of a dormant colloidal system that can be precisely and effectively targeted to cancer cells and then remotely activated to trigger apoptosis presents unquestionable potential as alternative to classical anticancer chemotherapy.

6.4. FOLATE DENSITY EFFECT ON CELL INTERNALIZATION PATHWAY OF TARGETED GOLD NANOPARTICLES

A vast number of in *vitro* studies have shown that the presence of multiple copies of folate on the surface of targeted drug carriers increases the therapeutic effect of the treatment as consequence of the enhancement of the folate receptor binding avidity and the internalization rate of the carrier[85]. Although this may be true , little work has been done to determine whether an optimal ligand density exists.

Cell uptake and trafficking of nanoparticles is affected by sever parameters including size, shape, material composition, charge, surface decoration. In general, it has been found that nanoparticles can be internalized via multiple pathways, which are currently poorly understood. Furthermore, it is not known in detail if and how the density of folate on nanocarrier surface can hijack colloids toward one specific uptake pathway or can dictate the rate of migration across the pathway. The answers to all these questions can be of great value for therapeutic applications of targeted systems.

6.4.1. Aim of the study

In the presented section, detailed and extensive intracellular trafficking studies were performed in order to evaluate the folate density effect on the particle uptake efficiency using alternative analytical tests and on the internalization pathway. Gold nanoparticle surface was decorated with increasing densities of Folate-$PEG_{3.5kDa}$-SH, which was selected as targeting agent. In this section, to investigate GNP uptake and trafficking, gold nanoparticles were fluorescently labelled with Rhodamine. The fluorophore was bound to the particles through a thiol-PEG linker of 2 kDa. The Rhodamine-PEG-SH was used to saturate the GNP surface, thus it served both as labelling and stabilizing agent. Notably, 2 kDa PEG was selected as spacer for the Rhodamine conjugation to provide for suitable exposure of the targeting moiety Folate-$PEG_{3.5kDa}$-SH and alleviate potential steric hindrances for folate receptor binding.

6.4.2. Determination of GNP surface decoration efficiency

The conjugation efficiency of each polymer used for the generation of *Rhodamine labelled Folate targeted gold nanoparticles*, was assessed by modifying GNPs with increasing molar excesses of the polymers and then by quantification of unreacted polymer. Particles samples were reacted with 1:25, 1:50, 1:100, 1:200, 1:500, 1:1000 and 1:2000 GNP/Rho-PEG_{2kDa}-SH molar ratios. Reference polymer samples, containing the same Rho-PEG_{2kDa}-SH concentration used to decorate the particles, were prepared for each GNP/polymer feed ratio by replacing the particle volume with milliQ water.

After incubation, gold nanoparticles were isolated by centrifugation. Spectrofluorometric analysis of the supernatant for the quantification of the Rho-PEG_{2kDa}-SH bound on the particle surface provided the conjugation efficiency for each GNPs/polymer feed ratio (Table III.).

Table III. Conjugation yield of Rho-PEG_{2kDa}-SH to GNP surface at increasing polymer/GNPs feed ratios.

GNP/polymer feed molar ratio	Rho-PEG-SH conjugation yield (%)
1:25	98
1:50	98
1:100	95
1:200	87
1:500	67
1:1000	56
1:2000	27

At low coverages, PEG chains collapse on the particle surface and dispose in a "mushroom-like" conformation; however, as the density increases, they undergo a transition to a more extended conformation (i.e., the "brush-like" structure) toward the bulk[123]. Taking into account the GNP surface area (calculated to be 707 nm^2 for 15 nm gold nanoparticles simplified to spheres) and the results from the coating efficiency study, 1:1000 GNP/Rho-PEG-SH feed molar ratio ensures the particle surface saturation with 560 polymer chains/GNP, corresponding 0.79 chains/nm^2.

Notably, the incubation of gold nanoparticles with a higher excess of Rho-PEG$_{2kDa}$-SH (1: 2000 GNP/Rho-PEG-SH m.r.) do not increase the polymer density on the particle surface as shown in the functionalization profile reported in Figure 45.

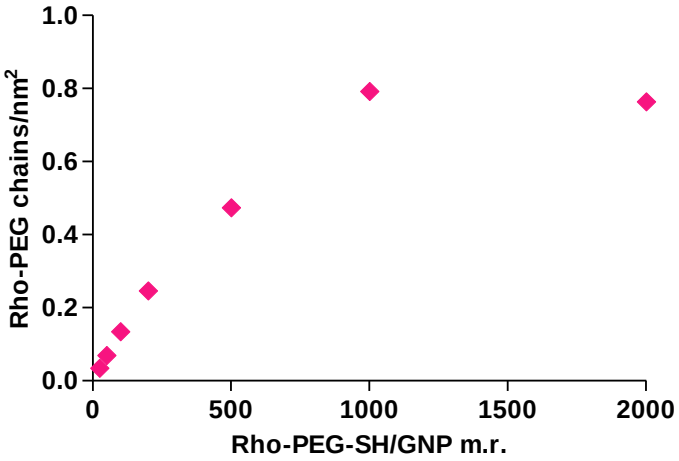

Figure 45. Functionalization profile of GNPs at increasing molar excesses of Rho-PEG$_{2kDa}$-SH.

The maximum density of Rho-PEG$_{2kDa}$-SH on the particle surface is in agreement with the previous results obtained with mPEG$_{2kDa}$ -SH. The slightly lower density of the polymer may be dictated by the Rhodamine hindrance on the surface of the GNPs, which reduces the sliding of the Rhodamine-PEG-SH chains during the coating equilibrium.

The GNP surface decoration efficiency with Folate-PEG$_{3.5kDa}$-SH was previously described in Chapter 6.3.2.

6.4.3. Rhodamine labelled folate targeted gold nanoparticle preparation and characterization

Rhodamine labelled Folate targeted gold nanoparticles were produced by decoration of gold nanoparticles with different ratios of Folate-PEG$_{3.5kDa}$-SH and then the surface was saturated with Rhodamine-PEG$_{2kDa}$-SH.

Gold nanoparticles were decorated with Folate-PEG$_{3.5kDa}$-SH by incubating particles with increasing Folate-PEG-SH/GNP feed molar ratios (from 10:1 to 100:1). Then, Folate decorated particles were added of a 1000 Rhodamine-PEG$_{2kDa}$-SH molar excess with respect to GNPs. As shown by the surface decoration study in the previous Chapter (Chapter 6.4.2.), 1000:1 Rho-PEG-SH/GNP feed molar ratio ensure the

particle surface saturation. *Rhodamine labelled Folate targeted GNPs* were finally isolated by centrifugation. The conjugation yield of Rhodamine-PEG_{2kDa}-SH was derived by UV-Vis analysis by difference between the non conjugated polymer quantified in the supernatant and the fed polymer. About 500 Rhodamine-PEG_{2kDa}-SH chains/GNP (0.70 chains/nm^2) were detected: the presence of Folate-$PEG_{3.5kDa}$-SH slightly decreased the Rho-PEG-SH conjugation efficiency with respect to the result obtained when naked particles were modified with only Rhodamine-PEG-SH (see Table III) without affecting the total chain number on the particle surface.

Rhodamine labelled Folate targeted GNPs were characterized by DLS, TEM and UV-Vis spectroscopy. The dynamic light scattering analysis revealed a particle size of about 30 nm (29.3±6.5 nm for the Rhodamine labelled 50x Folate targeted GNPs) and a low PDI (0.312 for the same formulation). The DLS correlogram confirmed the narrow size distribution of the particle formulation (Figure 46 – B). In fact, the time of analysis on the correlogram at which the correlation coefficient starts to significantly decay indicates the mean size of the sample. The steeper the profile, the more monodisperse the sample is.

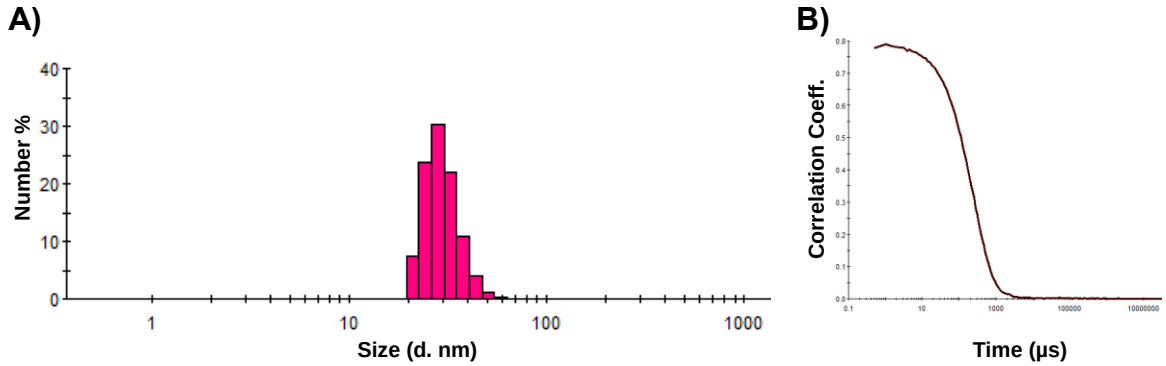

Figure 46. Dynamic Light Scattering profile of Rhodamine labelled 50x Folate targeted GNPs in milliQ water (A) and the corresponding correlogram (B).

The particle morphology was shown by TEM imaging (Figure 47.) which confirmed the particle homogeneous size distribution, the absence of aggregates and an average particle size of 29.9±3.2 nm, in excellent agreement with the DLS analysis.

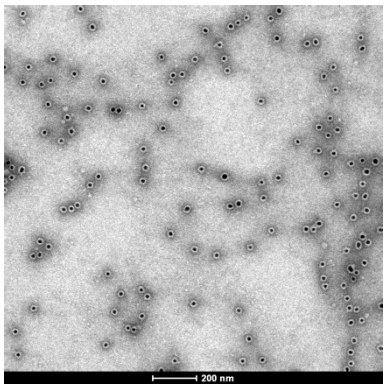

Figure 47. TEM image of Rhodamine labelled 50x Folate targeted GNPs dispersed in milliQ water.

Furthermore, the grey corona surrounding the particle core (black dots) confirms the presence of the polymeric material and results from the low electron density of the organic material with respect to the metallic core of the particles.

6.4.4. Rhodamine labelled folate targeted gold nanoparticle preparation and cellular studies

We investigated here the effect of surface ligand density on the internalization of nanoparticles by KB cells (which up-regulate the expression of FR) and MCF-7 control cell line by using cytofluorimetric analysis that was expected to confirm the quantitative data obtained by atomic absorption spectroscopy on non-fluorescent GNP platform discussed in the previous chapter. In addition, fluorescently labelled targeted particles were exploited for cell tracking and intracellular trafficking study. GNPs were surface modified by adsorption of Folate-$PEG_{3.5kDa}$-SH at different molar ratios, ranging from 10 to 100 molecules of Folate per particle (Table IV). Control non-targeted particles were produced by replacing the Folate-$PEG_{3.5kDa}$-SH with $mPEG_{3.5kDa}$-SH. The particle surface was then saturated with the fluorescent label Rhodamine-PEG_{2kDa}-SH which acts was used also to provide for particle colloidal stabilization, to reduce aggregation and to yield a “stealth” nanosystem with low protein opsonization.

Table IV. Composition of Rhodamine labelled Folate targeted GNP formulations decorated with different Folate-PEG-SH density.

Sample	FA-PEG-SH chains/GNP	Rho-PEG-SH chains/GNP
PEG-GNPs	0	500
10x FA-GNPs	10	500
25x FA-GNPs	25	500
50x FA-GNPs	50	500
100x FA-GNPs	100	500

The particle uptake efficiency was evaluated by Atomic absorption spectroscopy on the KB cell lysates. Data in Figure 48. clearly demonstrate that KB cell uptake of *Rhodamine labelled Folate targeted gold nanoparticles* is remarkably affected by the number of Folate molecule per particle, whereby the uptake increases with an increase in folate density on the particle surface and achieves a plateau for particles coated with 50 chains of the Folate-$PEG_{3.5kDa}$-SH/GNP. The profile trend in Figure 48. is in good agreement with the previous uptake study carried out with *Folate targeted gold nanoparticles* (Chapter 6.3.4), showing a maximum particle uptake of 19387 GNPs/cell. This result indicated that the fluorescently labelled targeted particles behave similarly to the non-fluorescently labelled particles in term of cell association and that the Rhodamine at the terminus of the 2 kDa PEG-SH does not affect the extent of particles uptake by KB cells. Control non-targeted particles showed a negligible KB cell uptake confirming that the endocytotic process is mediated by the Folate receptor.

The range of *Rhodamine labelled Folate targeted gold nanoparticles* with different Folate density was also tested on MCF-7 cell line that does not express FR, revealing a very limited association, further confirmation of the uptake selectivity.

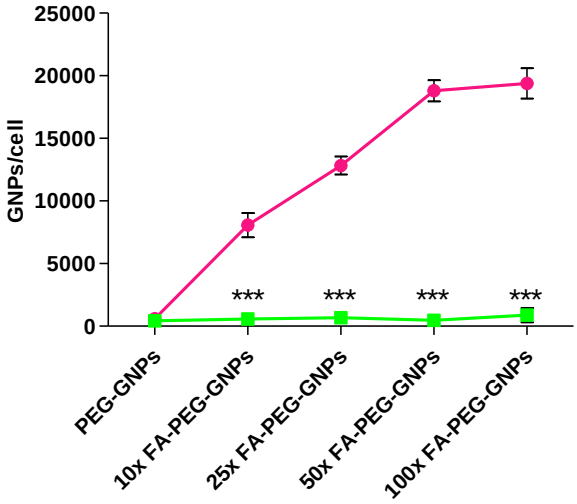

Figure 48. Cell uptake profile of Rhodamine labelled Folate targeted gold nanoparticles (FA-PEG-GNPs) at different FA density and non-targeted gold nanoparticles (PEG-GNPs) by KB HiFR (●) and MCF-7 (■) cell lines by Atomic absorption analysis. Statistical significance was calculated either versus non targeted particles or MCF-7 FR non expressing cell line: *** $p<0.001$.

The particle uptake profile obtained by the Atomic absorption analysis was by the cytofluorimetric study. As reported in Figure 49., GNPs modified with 25 chains of FA-PEG-SH per particle (25x FA-PEG-GNPs) are taken up significantly more respect to non-targeted GNPs. On the contrary non statistically significant higher uptake was shown by 10x FA-PEG-GNPs respect to PEG-GNPs. A linearly higher cell uptake was observed by increasing the Folate density from 25 to 100 chains per particle.

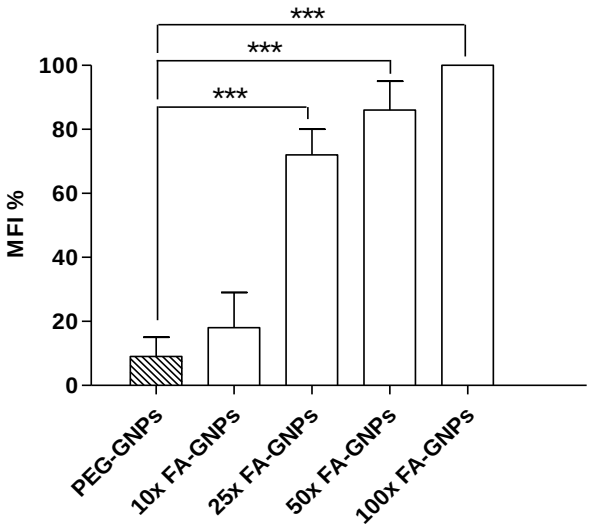

Figure 49. Mean Fluorescence intensity percentage of KB HiFR cells incubated with Rhodamine labelled Folate targeted gold nanoparticles (FA-PEG-GNPs) with different FA-PEG-SH density on the particle surface (10x, 25x, 50x and 100x) and non-targeted gold nanoparticles (PEG-GNPs) gold nanoparticles by KB HiFR cell line. The MFI were normalized to the MFI of cells incubated with 100x FA-PEG-GNPs. Statistical significance was calculated either versus non targeted particles (PEG-GNPs): *** $p<0.001$.

Confocal microscopy studies were performed on KB cells incubated with *Rhodamine labelled Folate targeted GNPs* modified with different density of folate and non-targeted GNPs in FFDMEM medium at pH 7.4 and 6.5 to mimic the physiological and tumor conditions, respectively. Representative images for this experiment are shown in Figure 50. (A, B, C, D, E) which highlight the increased particle internalization as the FA-PEG-SH density on the GNP surface increase.

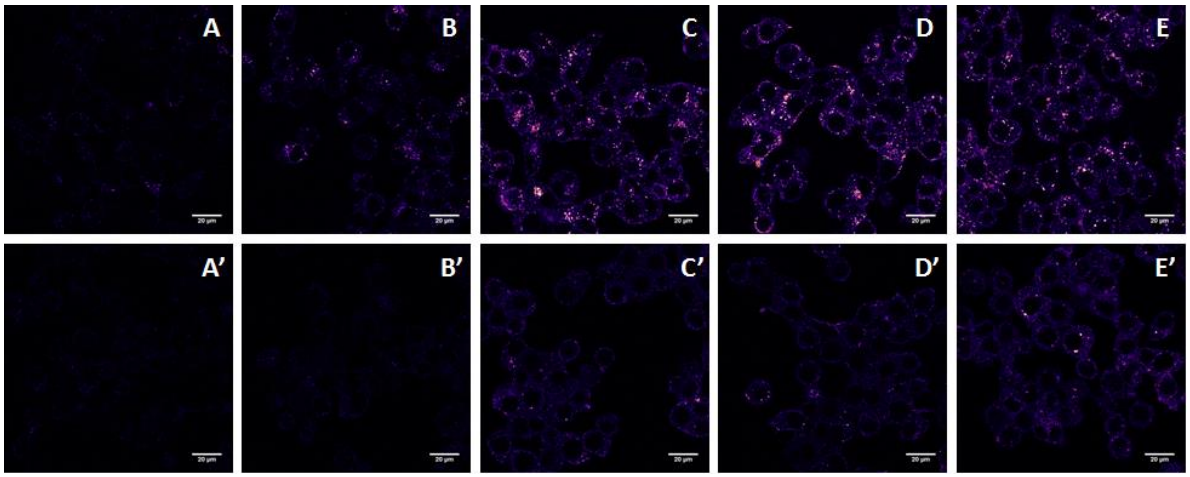

Figure 50. Confocal microscopy images of KB cells incubated with Rhodamine labelled gold nanoparticles decorated with increasing number of FA-PEG-SH units (0, 10, 25, 50 and 100 units per particle) at pH 7.4 (A, B, C, D, E) and pH 6.5 (A', B', C', D', E'). Scale bars of 20 μm.

Quantitative analyses of the confocal images (Figure 51.) showed a very limited association of PEG-GNPs at both pHs endorsing the Folate receptor mediated uptake. The increase of FA-PEG-SH density from 10 to 25 chains per particle results in a dramatic rise of the cell uptake which levels out from 25 up to 100 chains of FA-PEG-SH per particle.

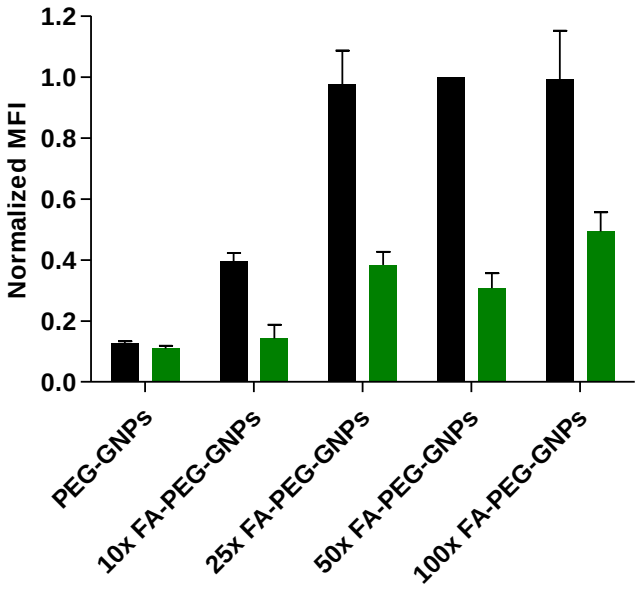

Figure 51. Normalized Mean Fluorescence Intensity of confocal images of KB cells incubated with different Rhodamine labelled Folate targeted GNP formulations (10, 25, 50 and 100 chains of FA-PEG-SH per particle) and control non-targeted GNPs (PEG-GNPs) at pH 7.4 (■) and 6.5 (■). The data were normalized to the Mean Fluorescence Intensity value of 50x FA-PEG-GNPs sample at pH 7.4. Error bars represent SD between mean normalized values of three independent experiments.

Competitive studies were performed to assess the cell uptake selectivity of Folate targeted particles. Figure 52. shows that the uptake inhibition of *Rhodamine labelled folate targeted GNPs* caused by the presence of free Folate is significant and is ascribed to the competition of free folate for the Folate receptor binding. In particular, 50x FA-PEG-GNP uptake decreased of about 3.5 times upon the addition of 200 μM Folate to the incubation media.

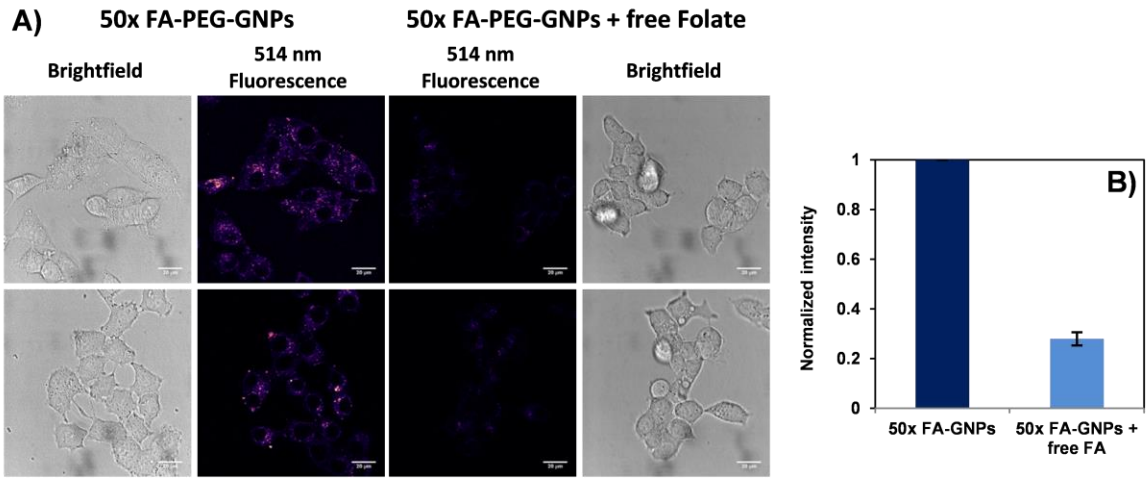

Figure 52. (A) Representative confocal microscopic images of KB cells incubated with 50x FA-PEG-GNPs in the presence or not of free Folate as competitive agent. Scale bars of 20 μm. (B) Normalized Mean Fluorescence Intensity of confocal microscopic images of KB cells incubated with fluorescent Folate targeted GNPs (50x FA-PEG-GNPs) in the presence (■) or not (■) of free Folate. The data were normalized to the Mean Fluorescence Intensity value of cells incubated with particles. Error bars represent SD between mean normalized values of three independent experiments.

In order to better underline the effect of the pH on the particle internalization, in Figure 53. we have referred the uptake of each particle formulation at pH 6.5 to that of the same formulation at pH 7.4. The acidic pH causes a significant decrease (at least 50-60%) of the GNP KB cell uptake for all the *Rhodamine labelled Folate targeted GNP* formulations. Consistently with the literature, Folate receptor exhibits a lower affinity to its ligand at acidic pH because of the structural rearrangement between an ‘‘open’’ accessible conformation, accessible to the ligand at neutral pH, and a ‘‘closed’’ state at slightly acidic pH as consequence of a partial unfolding of a key α-helical motif[134]. Notably, the uptake decrease percentage at acid pH mimicking the tumor environment is quite similar for all formulations, which reasonably reflects the loss of affinity of the folate cellular receptor at pH 6.5.

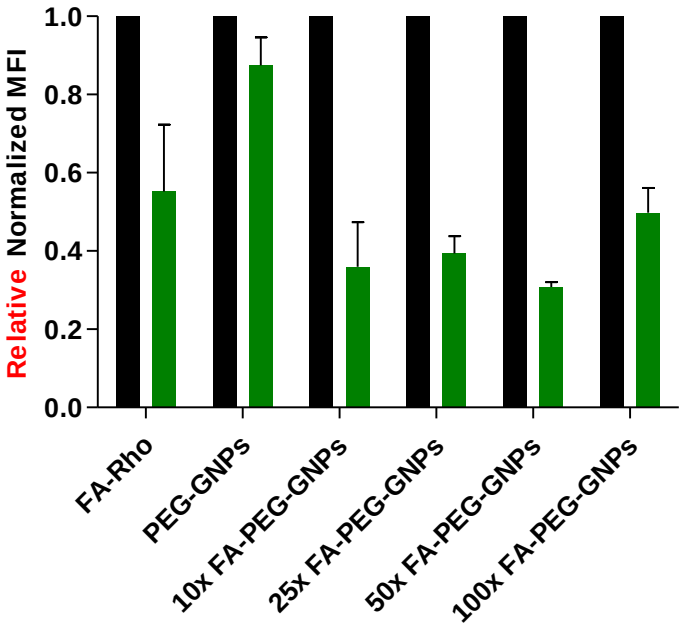

Figure 53. Normalized Mean Fluorescence Intensity of confocal microscopy images of KB cells incubated with different Rhodamine labelled Folate targeted GNP formulations (0, 10, 25, 50 and 100 chains of FA-PEG-SH per particle) and the monovalent ligand FA-C_5-Rho at pH 7.4 (■) and 6.5 (■). The data were normalized to the MFI value of each sample at pH 7.4. Error bars represent SD between mean normalized values of three independent experiments.

Aiming at understanding whether the internalization efficiency was affected by the pH also for a monovalent ligand, Folate-Cadaverine-Rhodamine (FA-C_5-Rho) was tested with KB cells in FFDMEM at pH 7.4 and 6.5 (Figure 54.). The image quantification showed even for the small mono-targeted molecule the negative effect of the acidic pH on the internalization process (Figure 53.) confirming that it should be ascribed to the receptor binding affinity rather than to the structural feature of the carrier. Moreover, the incubation of FA-C_5-Rho in the presence of free folic acid revealed a significant decrease of the fluorescent labelled ligand uptake, confirming the endocytosis mediated by the Folate receptor (Figure 54.).

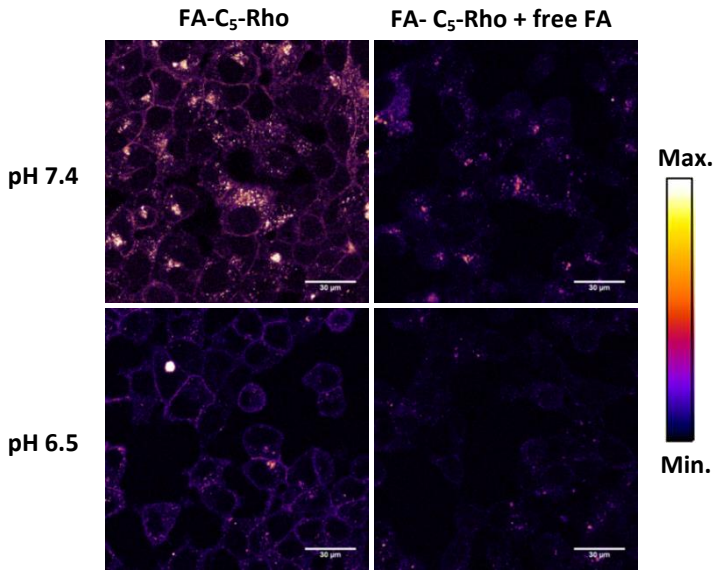

Figure 54. Confocal microscopy images of KB cells incubated with FA-C_5-Rho at pH 7.4 and 6.5, in the presence or not of free folate as competitive agent for the binding to the Folate receptor. Scale bars of 30 μm.

6.4.5. INTRACELLULAR TRAFFICKING STUDIES

6.4.5.1. Lysosomal delivery

Historically, the lysosomal compartment has been considered the endpoint of the active endocytic process. Lysosomal delivery of targeted drug nanocarriers allows the release of therapeutic molecules from the prodrugs and the simultaneous degradation of cell membrane receptors bound to the delivery systems. An enhanced trafficking toward the lysosomal compartments was observed for many receptors when they were induced to cluster on the cell membrane. This was observed for ErbB receptors[135], epidermal growth factor receptor, rabies G protein[136] and Transferrin receptor (TfR), while this was not clearly proved for the Folate receptor[89,137]. In order to evaluate the effect of the surface folate density on the lysosomal delivery of *Rhodamine labelled Folate targeted gold nanoparticles*, we selected two representative multivalent particles modified with different degrees of Folate-PEG-SH (50x FA-PEG-GNPs and 10x FA-PEG-GNPs) and a monovalent ligand (FA-C_5-Rho) as control. Cells were pulse-chased with the fluid-phase endocytosis probe Dex-647 to specifically label lysosomes[138]. Cells were imaged by confocal microscopy at scheduled times and the average intensity per pixel in the fluorescent vesicle regions

was calculated using a threshold and background subtraction method as described in the Methods section.

Representative images of the KB samples (Figure 55.) demonstrated the increased colocalization of both the GNP formulations tested with Dex-647 labeled lysosomes over time. Quantitative analysis of these fluorescence images (Figure 56.) shows an increase in mean fluorescence intensity (MFI) between 0 and 2 hours after the initial incubation of 30 minutes. The MFI values tend to plateauing between 2 and 4 hours. Notably, the 50x FA-PEG-GNP formulation displayed a 30% higher colocalization in the lysosomal compartments with respect to either 10x FA-PEG-GNPs or FA-C_5-Rho.

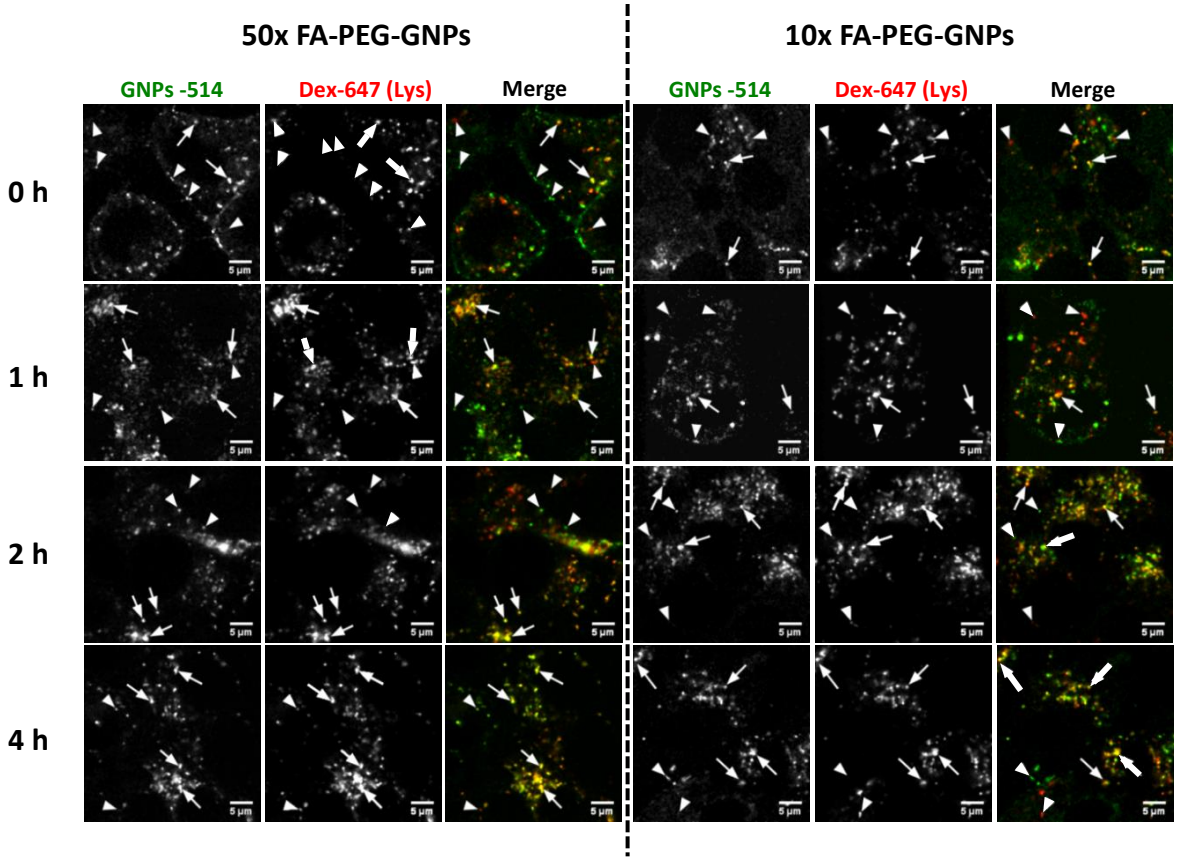

Figure 55. Representative confocal microscopy images of KB cells pulse-chased with Dex-647 to label lysosomes, and then incubated with gold nanoparticles decorated with different densities of targeting agent FA-PEG-SH (50x FA-PEG-GNPs and 10x FA-PEG-GNPs) for 30 minutes at 37 °C in 5% CO_2 atmosphere. Live cells were imaged at 0, 1, 2 and 4 hours. Arrowheads denote vesicles containing lysosomes and FA-PEG-GNPs only, while arrows point the colocalization of FA-PEG-GNPs within the lysosomes. Scale bars of 5 μm.

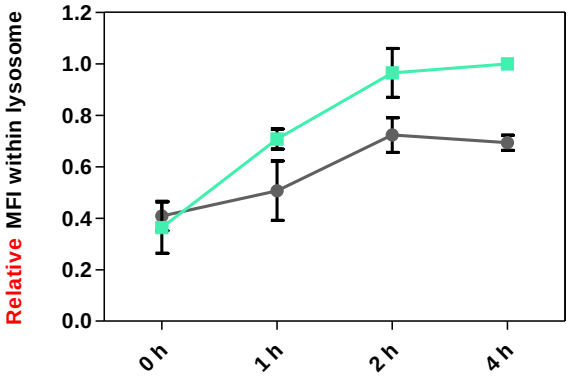

Figure 56. Relative Mean Fluorescence intensity of 10x FA-PEG-GNPs (●) and 50x FA-PEG-GNPs (■) within lysosomal compartments of KB cells over time (0, 1, 2 and 4 hours) after 30 minutes incubation. The data were normalized to the Mean Fluorescence intensity value of 50x FA-PEG-GNPs after 4 hours. Error bars represent SD between mean normalized values of three independent experiments.

The evidences showed that the accumulation of particles in the lysosomes is significantly affected by the density of the folate on their surface.

The images of KB cells incubated with FA-C_5-Rho are shown in Figure 57. At time 0 the FA-C_5-Rho is mostly adsorbed on the cell membrane. This in accordance with diffusively distribution at the cell surface of Folate receptor described in literature, without any local concentration of FRs in the lumen of the caveolae.

Between 1 and 2 hours there is a dramatic increase of the fluorescence intensity associated to lysosomes which stabilizes between the 2 and 4 hours. A slight dip of the FA-C_5-Rho disposing in the lysosomes was registered at the 4^{th} hour probably due to the destabilization of the lysosome or the recycling out from the cell which induce the release of FA-C_5-Rho in the bulk.

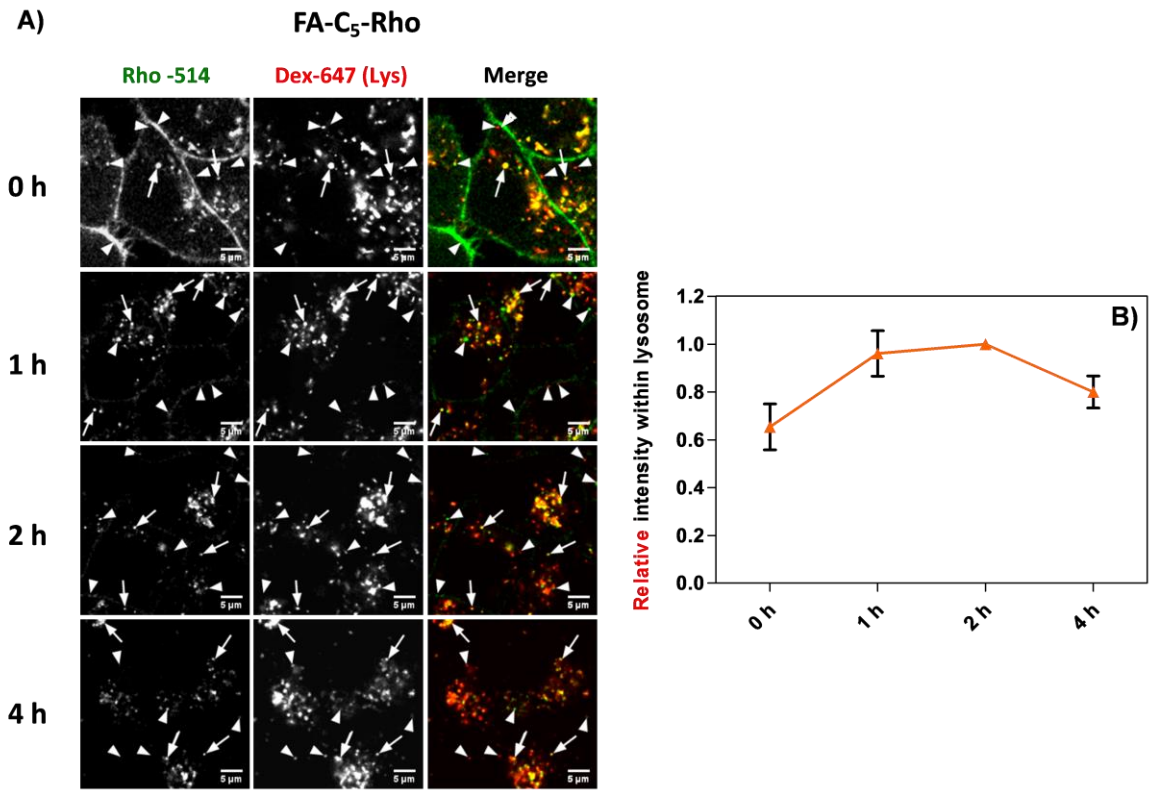

Figure 57. (A) Representative images of KB cells pulse-chased with Dex-647 to label lysosomes, and then incubated with the conjugate Folate-Cadaverine-Rhodamine (FA-C_5-Rho) for 30 minutes. After incubation, live cells were imaged at 0, 1, 2 and 4 hours. Arrowheads denote vesicles containing lysosomes and FA-C_5-Rho only, while arrows point the colocalization of FA-C_5-Rho within the lysosomes. Scale bars of 5 µm. (B) Relative Mean Fluorescence intensity of FA-C_5-Rho (▲) within lysosomal compartments of KB cells over time (0, 1, 2 and 4 hours) after incubation of 30 minutes. The data were normalized to the MFI value of FA-C_5-Rho after 2 hours. Error bars represent SD between mean normalized values of three independent experiments

Furthermore the colocalization within lysosomes was evaluated by Pearson's coefficient (PC), which is calculated as the r value for the correlation of pixel intensities between corresponding pixels of two images (Figure 58.). PC allows to compare different treatment regardless the concentration and the sample relative fluorescence intensity. Cells incubated with 50x FA-PEG-GNP sample showed a linear increase of the PC between the 0 and 2 hours achieving a PC value of 0.75 which corresponds to a strong colocalization with the lysosomal compartments. No PC increase was observed even after 4 hours. On the contrary GNPs decorated with the lower density of FA-PEG-SH (10x FA-PEG-GNPs) exhibited a maximum PC value of 0.57 after 4 hours, which corresponds to a 20% lower colocalization than the 50x FA-

PEG-GNPs. The profile of 10x FA-PEG-GNPs almost overlaps the profile shown by FA-C_5-Rho. The maximum PC value of 10x FA-PEG-GNP and FA-C_5-Rho samples was achieved by the 50x FA-PEG-GNP formulation after 1.3 hours instead of 4 hours.

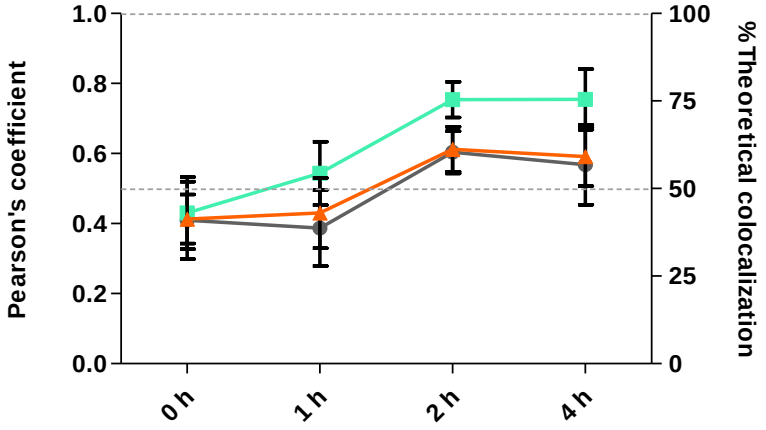

Figure 58. Pearson's Coefficient of Folate targeted GNPs (10x FA-PEG-GNPs (●), 50x FA-PEG-GNPs (■)) and the conjugate FA-C_5-Rho (▲) within the lysosomes of KB cells.

Overall, the results and the Pearson's coefficient deconvolution indicate that the higher the density of folate on the particle surface the faster is the migration of particles to the lysosomes. One hypothesis to explain the faster kinetic to lysosomes of the 50x FA-PEG-GNP formulation compared to the monovalent ligand FA-C_5-Rho and 10x FA-PEG-GNP sample can be ascribed to a different internalization pathway of these systems. The binding of targeted nanocarriers to membrane associated Folate receptors can induce, depending on folate density, a different clustering of the receptors on the membrane, which triggers a signal to highjack the colloidal system to different intracellular routes. It is fascinating to see how cells can sense folate density on particle surface and respond accordingly by addressing targeted nanocarriers either to lysosomes or other organelles.

Furthermore, the results are supported by in *vitro* studies reported in the literature showing that membrane associated receptors traffic to lysosomes when crosslinked[137]. In fact, a multivalent targeting agent network may increase the GNP avidity for the membrane associated FRs, which, may mimic a crosslinking event of the receptor inducing the observed intracellular trafficking.

6.4.5.2. Pathway inhibition assay

The pathway by which the "Folate receptor-ligand" complex is internalized into a cancer cell has been a matter of debate. In the present study, we focused on elucidating the pathways and mechanisms of endocytic sorting of the cell membrane Folate receptor (FR). There are many hypotheses about the FR internalization pathways and reasonably a single mechanism is not sufficient to describe the intracytosolic Folate receptor fate. As reported by Parton *et al.*[79], Skretting *et al.*[80] and further confirmed by Fivaz *et al.*[81], endocytosis of FR occurs via clathrin-independent pathway. In light of this, KB cells were incubated in the presence or not of Dynasore which is a non-competitive inhibitor of dynamin, an essential molecule for the clathrin-dependent coated vesicle formation. Then cells were treated with FA-C_5-Rho, 50x FA-PEG-GNPs and AlexaFluor488 labelled Transferrin with (Tf-488). Tf-488 was selected as positive control to test the effective endocytosis inhibition by Dynasore, since transferrin is conventionally used as marker of the clathrin route[139].

By looking at the images of KB cells incubated with Tf-488, the Dynasore treatment caused a significant reduction of Tf-488 uptake compared to what observed in KB cells incubated with the FA-C_5-Rho and 50x FA-PEG-GNPs, which were equally taken up by KB cells in the presence or absence of Dynasore (Figure 59.). These results indicate that the cell uptake of *Rhodamine labelled Folate targeted nanoparticles* and the labelled ligand FA-C_5-Rho is independent on the clathrin-mediated pathway.

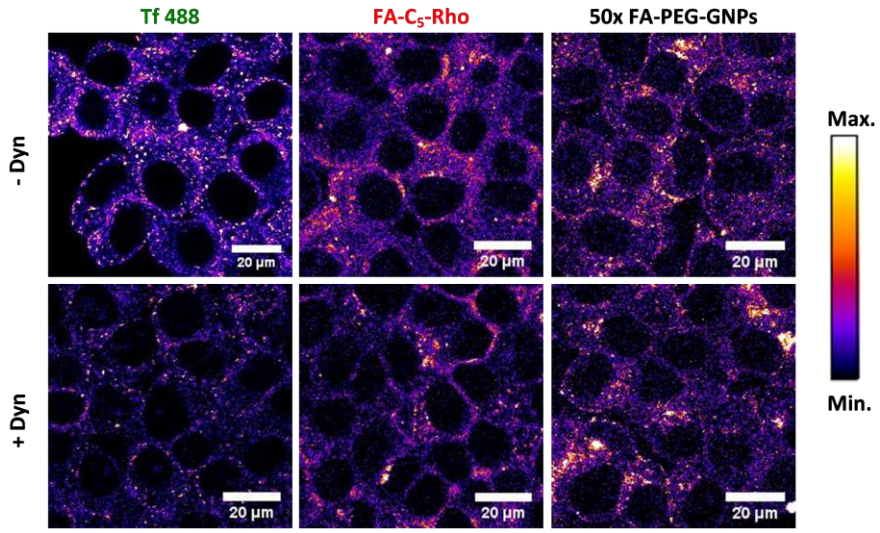

Figure 59. Representative confocal microscopy images of KB cells incubated with Transferrin-488 (Tf-488), FA-C_5-Rho and Rhodamine labelled Folate targeted GNPs (50x FA-PEG-GNPs) in the presence (+ Dyn) or not (-Dyn) of Dynasore. Scale bars of 20 µm.

6.4.5.3. Trasmission electron microscopy on KB cells

As established by the pathway inhibition assay, *Rhodamine labelled Folate targeted GNPs* are taken up by a clathrin-independent mechanism. Among the different non-clathrin dependent pathways, potocytosis represents the major route from the cell surface to endosomes. According to the potocytosis model, small molecules or macromolecules or the bulk liquid are transported into the cytosol by caveolae[140], small flask shaped plasma membrane invaginations with a dimension of about 50-60 nm[68]. Quantitative analyses of the FR distribution on the cell membrane have shown that FRs are diffusively distributed at the cell surface and there is no significant concentration of Folate receptors in caveolae. However, the administration of multivalent particles induces a substantial enrichment of the FR clusters in caveolae[75]. In particular, a significant colocalization of the Folate receptor clusters with caveolin, a fundamental component of the caveolae membrane coat, was measured[78]. In contrast to the findings described above, other research has pointed to internalization of FR by clathrin-coated pits. Clathrin mediated endocytosis occurs with the formation of vesicles with a final size of about 120 nm[68]. After the membrane invagination, the final vesicle fuses with an endosome and, later on, the endosome fuses with a lysosome in which the internalized particle can be degraded.

To better understand the process of Folate receptor mediated endocytosis of the *Rhodamine labelled Folate targeted GNPs*, we have analyzed KB cell slices by TEM imaging. Looking at the TEM images in Figure 60., the size and the shape of the endocytic vesicles support for the "caveolae-hypothesis" of folate receptor endocytosis pathway. This evidence is in agreement with the results discussed in the previous chapter that showed no involvement of the clathrin mediated uptake of these targeted particles.

Notably, the particles localize in the vesicles without aggregation, which show that the hydrophilic and flexible coating of the GNPs inhibits their aggregation also in contact with the biological environment. It is still to be elucidated if and how the localization of folate targeted particles on the cell membrane can cooperate to trigger caveolae invagination.

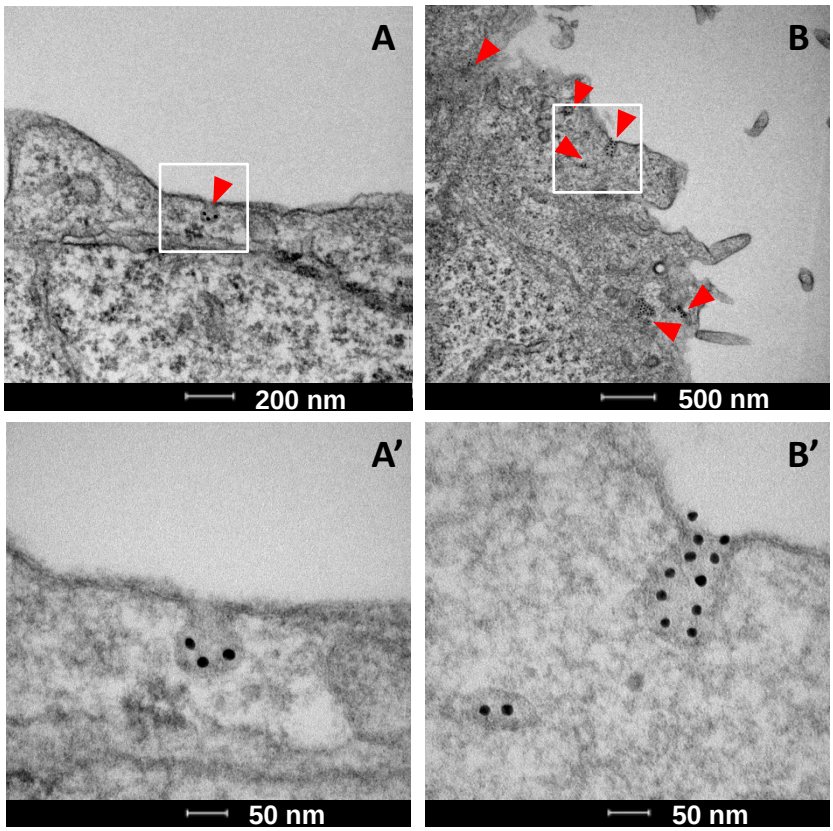

Figure 60. (A, B) TEM images of KB cells incubated with Rhodamine labelled Folate targeted GNPs (50x FA-PEG-GNPs) incubated with KB cells. Red arrows point to GNPs. Panel A' and B' are magnifications of panel A and B, respectively.

6.5. SMART pH SENSITIVE GOLD NANOPARTICLES FOR ENHANCED SITE-SELECTIVE ANTICANCER THERAPY

6.5.1. Aim of the study

In this study we propose the design for a nanoparticle carrier that combines different tumor targeting motifs into a single construct: 15 nm gold nanoparticles were decorated with a targeting agent, namely Folate-PEG_{2kDa}-SH, and stabilized by a pH sensitive polymer shell, made with poly(MCH-co-GMA) conjugated to the particles surface through the poly(MCH) block.

The physico-chemical and biological features of the individual components equip the construct of several enticing properties, among them: (i) Folate-PEG_{2kDa}-SH is a tumour-specific ligand that allows a biorecognition of malignant cells by the nanocarrier and trigger the intracellular disposition of the drug vehicle; (ii) the hydrophilic external block of poly(MCH-co-GMA), namely poly(GMA), stabilizes the particles against a variety of external stresses; (iii) the pH responsiveness of poly(MCH) block of poly(MCH-co-GMA) ensures the masking of the targeting moiety (namely the folate) at physiological pH while exposing only once the nanosystem has achieved the acid tumour compartment; (iv) nanocarrier size was properly selected to take advantage of the EPR effect aiming at combining an active and a passive targeting. The combined cancer cell biorecognition endowed by the folate ligand and the locally activated de-shielding of the latter by the pH responsive polymer is expected to result in a cooperative effect to enhance the system site-selectivity (Figure 61.).

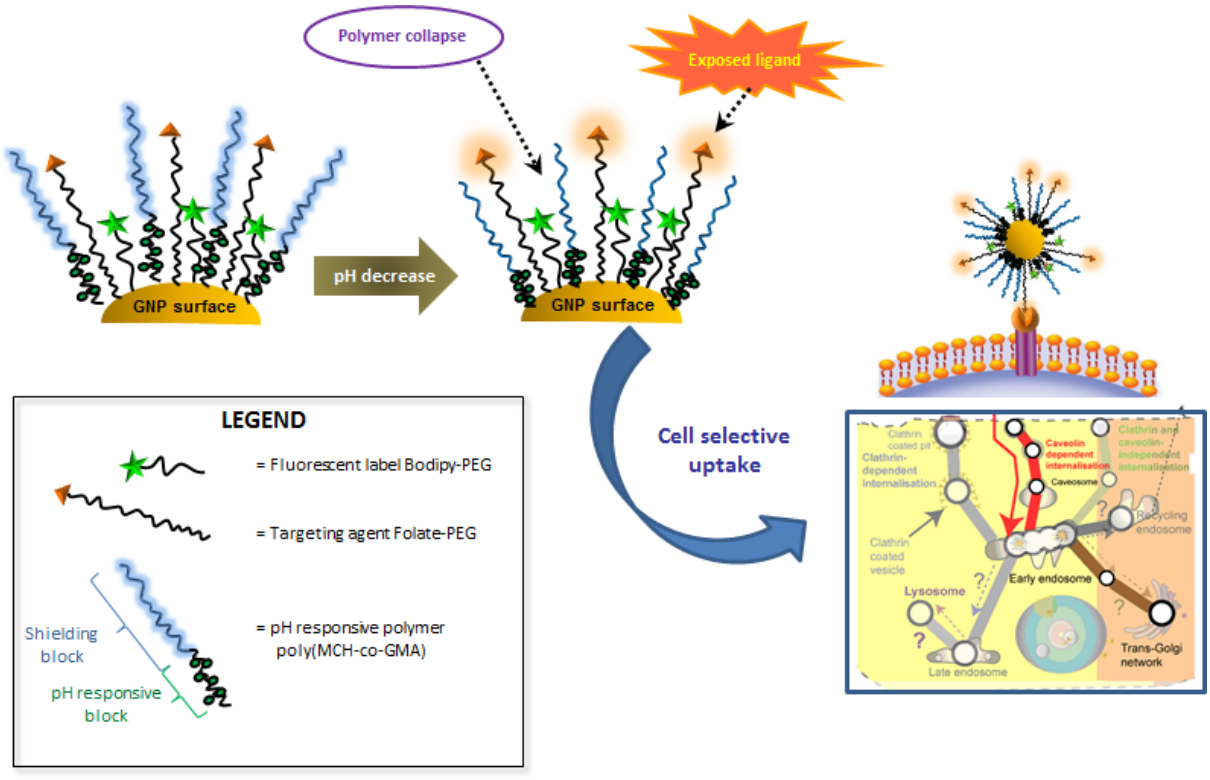

Figure 61. Graphical representation of the Folate targeted pH responsive gold nanoparticle system composition and function: the gold nanoparticle decoration is aimed at improving site-selectivity and local accumulation in the tumour compartment where the mild acidic conditions activate the nanoparticle biorecognition of the Folate receptor overexpressing cancer cells

The length and the grafting density of each component on the particle surface were accurately adjusted to guarantee an effective and site-selective accumulation in the tumour.

Folate was tethered to the particle surface via a PEG spacer of 2 kDa, which is the most representative material used to produce stealth nanocarriers. According to their hydrophilic and flexible nature, PEG chains can acquire an extended conformation on particle surface allowing the docking of Folate with the cellular Folate receptor. Considering the Folate-PEG_{2kDa}-SH length (calculated to be of about 20 nm on the basis of bond distances), poly(MCH-co-GMA) was synthetized with a proper length to guarantee the targeting agent shielding and exposition according to local pH alterations. As described before, poly(MCH-co-GMA) is a di-block copolymer whose composition (MCH/GMA molar ratio) and molecular weight were carefully designed to confer the desired pH responsiveness to the system. The predicted length of poly(MCH-co-GMA) is 27 nm resulting from the 12 nm of the pH responsive

poly(MCH) block and 16 nm of the hydrophilic poly(GMA) block. The polymer length is adequate to shield the Folate-PEG-SH when in the charged hydrated conformation, while shrinking is expected when the anionic poly(MCH) is protonated and become hydrophobic converting to a globule conformation.

Moreover, previously reported cell uptake studies (Chapter 6.3.4 and 6.4.4.) well established that 50-fold ratio of Folate-PEG-SH on the particle surface ensure the optimum condition for the particle internalization.

We will argue that by combining design principles that have individually proven successful in other nanoscale drug carriers, the system proposed in this thesis work not only inherits beneficial properties from its components but acquires novel features useful to its function.

6.5.2. Determination of GNP surface decoration efficiency

Aiming to assess the conjugation efficiency to the particle surface of each polymer used for the production of *Folate targeted pH responsive gold nanoparticles*, GNPs were surface modified with increasing molar excesses (1:500, 1:1000, 1:2000, 1:3000 and 1:6000 GNP/polymer molar ratio) of FA-PEG_{2kDa}-SH and poly(MCH-co-GMA) in order evaluate the decoration efficiency of each polymeric component. A reference sample for each polymer excess was prepared according to the same procedure, replacing the gold nanoparticle volume with milliQ.

After incubation, gold nanoparticles were isolated by centrifugation. The surface functionalization was estimated by UV-Vis spectrophotometric determination at 300 nm and 535 nm (Iodine assay) for the determination of the unbound poly(MCH-co-GMA) and FA-PEG_{2kDa}-SH, respectively. The corresponding reference sample was analyzed in the same way to assess accurately the polymer added to the particle suspension. The difference between the polymer added in feed (derived from the reference sample) and the non-unbound (in the supernatant) corresponds to the polymer attached to the particle surface.

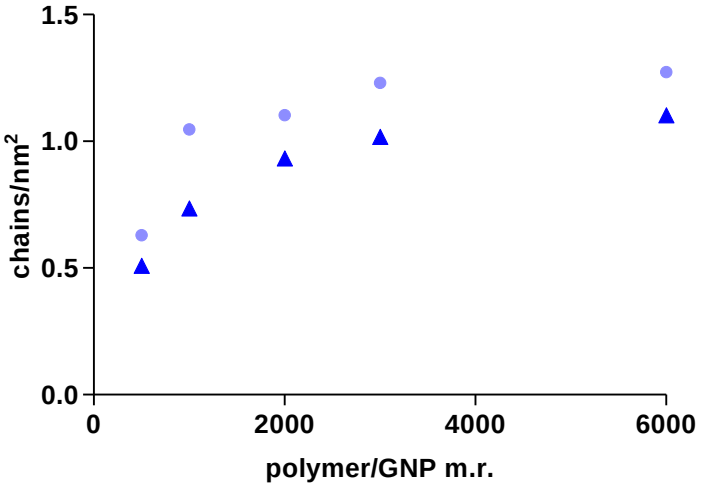

Figure 62. Functionalization profile of GNPs at increasing molar excesses of FA-PEG$_{2kDa}$-SH (●) and poly(MCH-co-GMA) (▲).

Increasing overall molar ratios of FA-PEG$_{2kDa}$-SH and poly(MCH-co-GMA) resulted in increased ligand density on the particle surface, up to a saturation level reached with a polymer excess between 3000 and 6000 with respect to GNPs. As well described in Chapter 6.3.2, at low polymer molar excess most of the surface is accessible to the polymer adsorption resulting in high decoration efficiency. In this condition polymer chains assume a "mushroom-like" conformation in order to homogenously cover the particle surface. As the polymer concentration increases, the binding of new polymer chains is retarded by the presence of the adsorbed ones. Nevertheless the binding to the surface is still possible due to transient excursions of polymer chains: polymers in solution are highly dynamic due to thermal fluctuations. At this point the adsorption of other chains enforces the polymer to rearrange from flat "mushroom-like" to "brush-like". In Table V are summarized the conjugation yield percentages of FA-PEG$_{2kDa}$-SH and poly(MCH-co-GMA).

Table V. Conjugation yields of FA-PEG_{2kDa}-SH and poly(MCH-co-GMA) to GNP surface at increasing feed ratios.

GNP/polymer m.r.	Conj. yield % FA-PEG_{2kDa}-SH	Conj. yield % poly(MCH-co-GMA)
1:500	89	72
1:1000	74	52
1:2000	39	33
1:3000	29	24
1:6000	15	13

Particle decoration with Folate-PEG_{2kDa}-SH revealed a maximum chain density of 1.27 chains/GNP in agreement with the decoration value reported in literature[141,142]. The amount of conjugated poly(MCH-co-GMA) per unit surface area showed a maximum ligand density of 1.10 chains/nm^2, a decreased conjugation yield with respect to linear polyethylene glycol, as the pH sensitive polymer side chains increase the hydrodynamic hindrance.

Moreover poly(MCH-co-GMA) is chemically adsorbed on particles via a Lipoic end-group linker which is provided of a dithiol ring that is more hindered as respect to the thiol group of Folate-PEG_{2kDa}-SH. This could be a reasonable hypothesis for the slight lower decoration efficiency showed by poly(MCH-co-GMA) with respect to Folate-PEG_{2kDa}-SH. To trace particles uptake and trafficking, *Folate targeted pH responsive gold nanoparticles* were labelled with Bodipy FL which was grafted to the particle surface through a PEG spacer of 2 kDa. As for the conjugation of Folic acid, 2 kDa PEG was selected in order to ensure the exposure of the targeting agent and allow the pH sensitive polymer to perform the shielding/deshielding pH mediated activity. Bodipy FL retains an high quantum yield once conjugated to macromolecules. thus a limited number of molecules could afford a good particle tracking without hindering the "globule" conversion of the pH responsive polymer on the particle surface at acid pH. Notably, 2 kDa PEG was already shown to provide for suitable distance between the a fluorescent tag and gold particle core to minimize the fluorescence quenching effect of the particles[143,144]. A 100:1 Bodipy-PEG_{2kDa}-SH/GNP feed molar ratio provided particles labelled with 95 units of Bodipy-PEG_{2kDa}-SH, highlighting the high conjugation yield of the decoration method (95% conjugation efficiency).

6.5.3. Folate targeted pH responsive gold nanoparticle production and characterization

In this project, we formulated and Pharacterized *Folate targeted pH responsive gold nanoparticles*. Decorated GNPs were obtained by a three-step procedure. In the first stage gold nanoparticles were surface modified by contact with 50 chains of Folate-PEG_{2kDa}-SH. Afterwards particles were labelled with Bodipy-PEG_{2kDa}-SH and then the surface was saturated with the pH responsive polymer poly(MCH-co-GMA).

The particle decoration degree was established at each step by spectrophotometric analysis of the supernatant at 535 nm (Iodine assay) and 300 nm to assess the adsorption of Folate-PEG_{2kDa}-SH and poly(MCH-co-GMA) respectively. The particle labelling with Bodipy-PEG_{2kDa}-SH was assessed by fluorometric analysis of the supernatant (λ_{ex} 503 nm, λ_{em} 509 nm). *Folate targeted pH responsive gold nanoparticles* decorated with 50 chains of Folate-PEG_{2kDa}-SH, 400 chains of poly(MCH-co-GMA) and labelled with 100 chains of Bodipy- PEG_{2kDa}-SH were produced and characterized by and UV-Vis spectroscopy, TEM and DLS.

The decoration of particles with the three polymeric components induced a red shift of the particle absorption band from 520 nm to 523 nm (Figure 63 - A.) which highlights that the GNP dielectric environment changed due to the exchange of the polymers to the citrate[145,146]. DLS analysis of functionalized particles showed a hydrodynamic volume of 34.2±3.1 nm, a significant increase compare to the size of naked GNPs (14.5±1.6). *Folate targeted pH responsive gold nanoparticles* showed a homogeneous size distribution as confirmed by both the narrow PDI value of 0.34, assessed by DLS, and the TEM images (Figure 63 – C). Furthermore, TEM images showed very nicely the presence of a grey corona surrounding the particle core proving the presence of an organic layer coating the particles. Figure 63 – C' reports the size distribution profile obtained by the elaboration of TEM images by ImageJ image processing program (n=200).

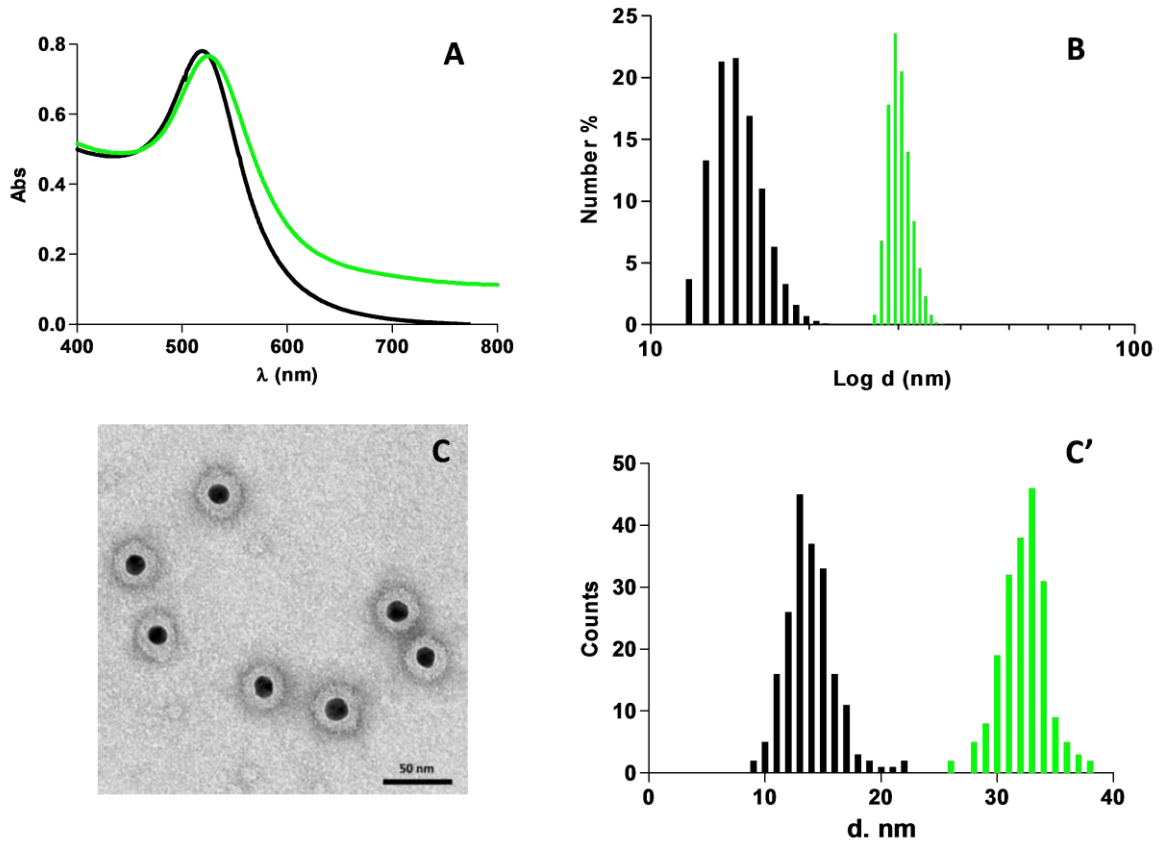

Figure 63. (A) UV-Vis spectra and (B) Dynamic Light Scattering profiles of naked GNPs (■) and Folate targeted pH responsive gold nanoparticles (■) in deionized water. (C) TEM analysis of Folate targeted pH responsive GNPs and (C') TEM size distribution profile of naked GNPs (■) and Folate targeted pH responsive GNPs (■) obtained by the elaboration of TEM images using ImageJ image processing program.

6.5.4. Stability study of folate targeted pH responsive gold nanoparticles

Stability of *Folate targeted pH responsive gold nanoparticles* was investigated in milliQ and FFDMEM medium at pH 7.4 and pH 6.5 by Dynamic Light Scattering analysis at 25°C. Control citrate-capped GNPs and $mPEG_{2kDa}$-GNPs were also tested.

Folate targeted pH responsive gold nanoparticles (FA pH resp.-GNPs) were prepared according to the procedure reported in the previous chapter. FA pH resp.-GNPs dispersed in milliQ water revealed a good stability for up 2 hours and no aggregation was observed.

In order to evaluate particle behavior at different pH, FA pH resp.-GNPs were suspended in FFDMEM at pH 7.4 and the pH was decreased by adding 0.1 N HCl. The acidification of the medium caused a slight destabilization of the particles with a mean size increase from 38 nm up to 141 nm which can be attributed to particle mild

aggregation. This event caused the sudden color change from red to violet since the particle Surface Plasmon is affected by size and aggregation. Then the gold suspension was brought again to pH 7.4 by adding 0.5 N NaOH resulting in immediate particle redispersion (size = 56 nm).

These results underline that the external block of the coating layer, namely the poly(GMA), guarantees for a good colloidal stability both at pH 7.4 and 6.5. At pH 7.4 the poly(MCH-co-GMA) polymer is extended and the coating layer is fully hydrated. On the contrary at a pH lower than its cloud point, the pH sensitive block poly(MCH) loses its charge and converts into the hydrophobic globular conformation which induces the partial particle instability, as shown by DLS data.

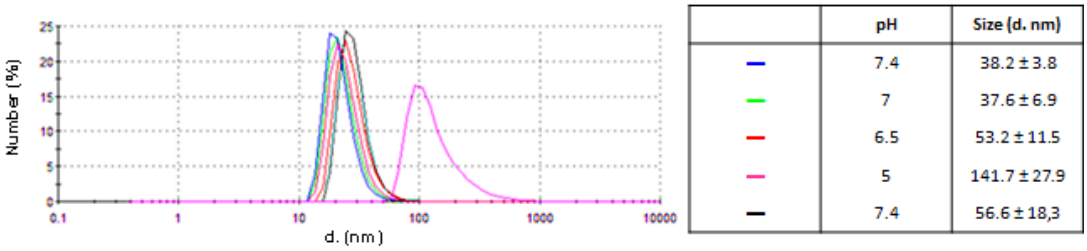

	pH	Size (d. nm)
—	7.4	38.2 ± 3.8
—	7	37.6 ± 6.9
—	6.5	53.2 ± 11.5
—	5	141.7 ± 27.9
—	7.4	56.6 ± 18,3

Figure 64. DLS profile of FA pH resp.-GNPs in FFDMEM in the pH range 7.4 - 5. The analysis was performed by decreasing the pH of the colloidal suspension from 7.4. After pH 5 was achieved (pink line), particle suspension was brought to pH 7.4 (black line).

The pH responsive stability was compared to that of naked (negative control) and PEG coated particles (positive control).

Colloidal dispersions of citrate-capped GNPs in milliQ water revealed a high stability over time without any variation of the mean diameter after 2 hours (Figure 65. – A). This is due to the electrostatic stabilization and charge repulsion provided by the citrate. Once diluted in FFDMEM, citrate-capped GNPs showed a massive aggregation (>1 µm) at both pH 7.4 and 6.5. After the first of incubation, the particle size grew significantly and the aggregate size achieved its maximum at the 2nd hour. This behavior may be induced by the charge/charge interaction of the cations of the buffer salts with the particle external citrate anions, leading to the neutralization of the surface charge, minimization of the repulsive forces thus destabilizing the colloidal system (Figure 65 - B).

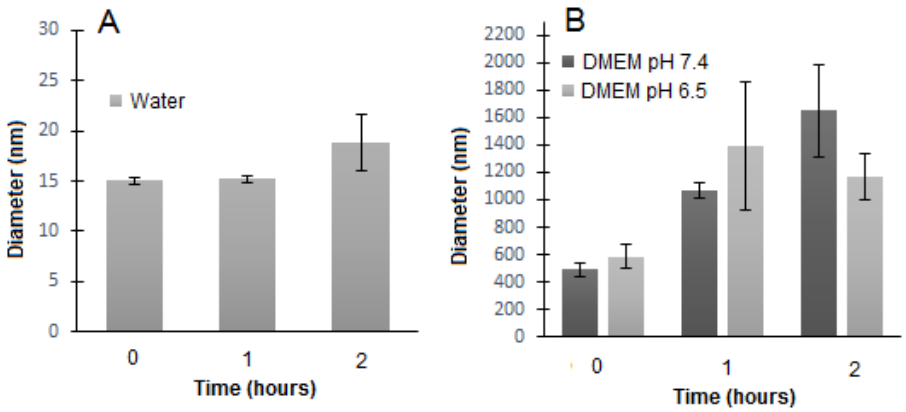

Figure 65. Stability profile of citrate capped GNPs in milliQ water (A) and FFDMEM at pH 7.4 and 6.5 (B).

The stability test performed on PEGylated particles (PEG-GNPs) highlighted the remarkable colloidal stabilization provided by the PEG coating which generates a steric hindrance to particle aggregation and helps lowering free energy on the surface of colloidal particles. The repulsive forces generated by a flexible PEG layer counterbalance the attractive van der Waals forces that involve approaching particles (Figure 66). The increased particle size respect to the citrate stabilized particles is due to the presence of the polymer corona.

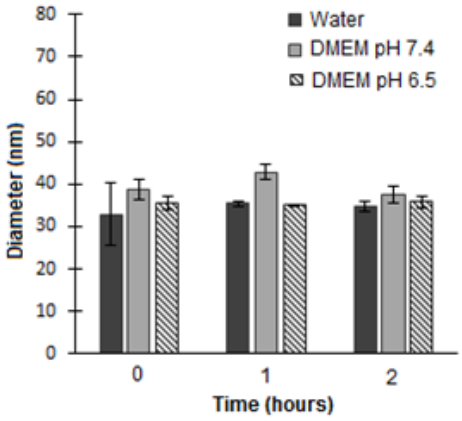

Figure 66. (A) Stability profile of PEG-GNPs in milliQ water and FFDMEM, at pH 7.4 and at pH 6.5.

6.5.5. Biocompatibility study

The *Folate targeted pH responsive gold nanoparticle* biocompatibility was explored by MTT (3-(4,5-dimethylthiazol-2-yl)-2,5-diphenyltetrazolium bromide) cell viability assay. Tetrazolium dye reduction into formazan salt depends on the mitochondrial activity associated to NAD(P)H flux. The quantity of formazan produced by

dehydrogenase activity is directly proportional to the number of living cells and it is quantified upon dissolution at 570 nm.

Folate targeted pH responsive GNPs cytotoxicity was tested in FFDMEM at pH 7.4 and 6.5 to assess if the pH condition was affecting the toxicity of the carrier. The biocompatibility test performed on MCF-7 breast cancer and KB human cervical carcinoma cell lines showed that *Folate targeted pH responsive particles* are non-toxic in the concentration range 0.2 – 2 nM at both pHs. A slight viability decrease was recorded for GNPs tested on KB cells at a concentration higher than 0.8 nM. However, cell viability was found to be higher than 85 % at all conditions and particle concentration proving the non-toxicity of the multicomponent system.

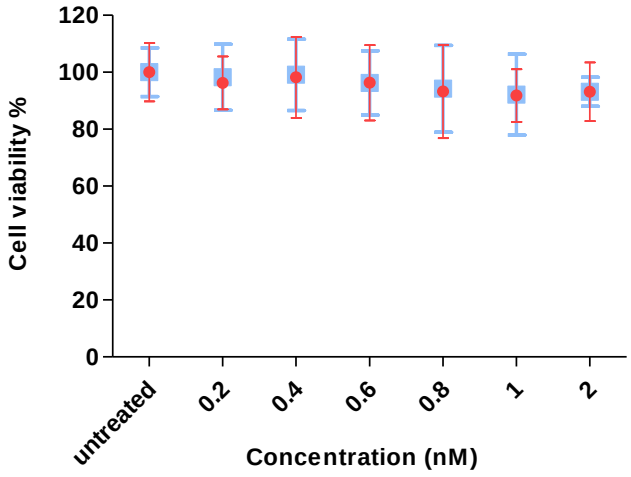

Figure 67. MTT cell availability profile of MCF-7 cells at increasing concentration of Folate targeted pH responsive GNPs at pH 7.4 (■) and 6.5 (●).

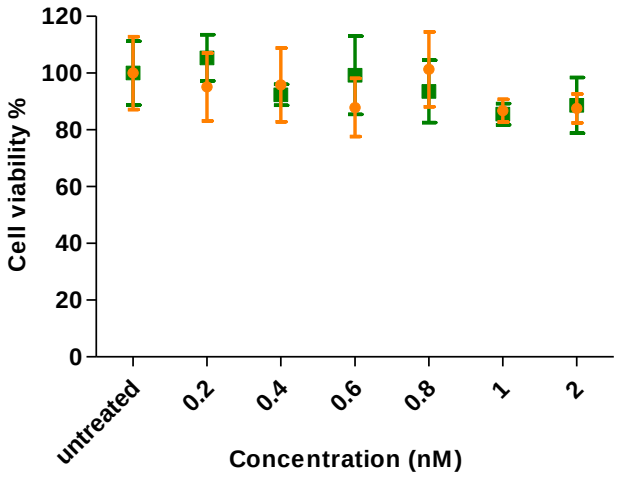

Figure 68. MTT cell availability profile on KB cells at increasing concentration of Folate targeted pH responsive GNPs at pH 7.4 (■) and 6.5 (●).

6.5.6. Folate targeted pH responsive gold nanoparticle cell uptake study

Folate targeted pH responsive gold nanoparticles were tested on high Folate receptor expressing KB cells (HiFR KB cells) and MCF-7 cells, which do not exhibit the FR on the cell membrane. Control non targeted particles were produced by replacing the Folate-PEG_{2kDa}-SH amount with $mPEG_{2kDa}$-SH. Particles decorated with Folate-PEG_{2kDa}-SH and the non-pH responsive polymer (poly(GMA)) were synthetized as additional controls to prove that the particle uptake is selectively mediated by the bioregnition of folate under the sensing effect of the pH change which triggers the polymer shrinking. poly(GMA) was generated to have the same monomer number and thus the same length of poly(MCH-co-GMA) but is not pH responsive: it maintains the extended conformation at all pH values, mask the targeting agent and prevent the interaction with the Folate receptor which mediates the endocytosis.

6.5.6.1. Atomic absorption analysis on cell lysate

KB and MCF-7 cells were incubated with Folate targeted pH responsive GNPs and control formulations for 2 hours in FFDMEM at pH 7.4 and 6.5. Cells were then detached and lysated upon Triton treatment. Cell lysates were mineralized by aqua regia and analyzed by Atomic absorption spectrometry for the gold quantification.

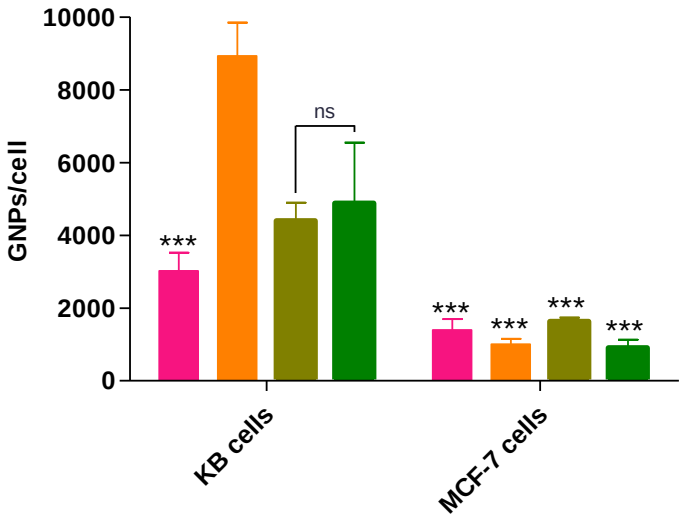

Figure 69. Cell uptake profile of Folate targeted pH responsive GNPs at pH 7.4 (■) and pH 6.5 (■) and non-targeted pH responsive GNPs at pH 7.4 (■) and 6.5 (■) by Atomic absorption spectrometry. Statistical significance was calculated versus Folate targeted pH responsive GNPs at pH 6.5: ns $p>0.05$; *** $p<0.001$.

Folate targeted pH responsive particles showed a 3-fold higher uptake at pH 6.5 with respect to pH 7.4 highlighting that the FR biorecognition is driven by the particle sensing capacity of the changed microenviromental pH. At physiological pH (7.4) poly(MCH-co-GMA) shows a hydrophilic coil conformation which confers the desired stealth properties to the nanosystem and hide the Folate ligand. When the protonation of the phenolic hydroxyl group occurs, the collapse of the pH responsive block of poly(MCH-coGMA) and the exposition of the targeting agent occurs. The specificity of the uptake was proved by the failed internalization of control non-targeted particles at both pHs.

In addition, uptake study performed on MCF-7 cell line showed a negligible internalization for each formulation further confirming the selective Folate mediated particle uptake.

6.5.6.2. Flow cytometry analysis

KB cells were incubated with the following particle formulations suspended in FFDMEM at pH 7.4 and 6.5:

- *Folate targeted pH responsive gold nanoparticles (FA pH resp.-GNPs).*
- *Non Folate targeted pH responsive gold nanoparticles (Non FA pH resp.-GNPs).*
- *Folate targeted non pH responsive gold nanoparticles (FA non pH resp.-GNPs).*

All formulations were labelled with Bodipy-PEG-SH as discussed in Chapter 6.5.3.

After 2 hours of incubation, cells were detached, fixed with PFA and analyzed by FACS (Bodipy FL: λ_{ex} 488 nm, λ_{em} 525 nm).

Cell uptake profile obtained by cytofluorimetric analysis confirmed the pH responsiveness of poly(MCH-co-GMA) which is able to finely control the Folate exposure. A very limited association was shown by either the non-targeted pH responsive particles or the Folate targeted non-pH responsive particles.

The data were in excellent agreement with the particle cell association performed with atomic absorption spectroscopy. This also validates the alternative use of the two analytical methods.

These results strongly support the selectivity of *Folate targeted pH responsive GNP* internalization which arises from the cooperative effect of the targeting agent and the pH sensitive component.

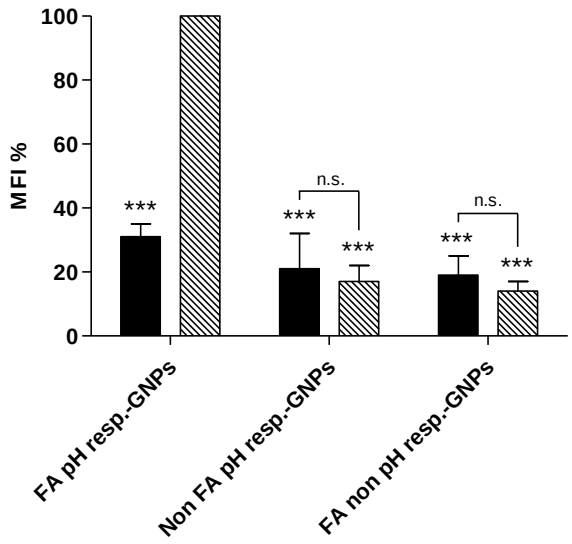

Figure 70. Cell uptake profile of Folate targeted pH responsive (FA pH resp.-GNPs), non-targeted pH responsive (Non FA pH resp.-GNPs) and Folate targeted non pH responsive (FA non pH resp.-GNPs) gold nanoparticles at pH 7.4 (■) and 6.5 (□) by Flow cytometry. The MFI % values were normalized to MFI of cells treated with Folate targeted pH responsive GNPs at pH 6.5. Statistical significance was calculated versus Folate targeted pH responsive GNPs at pH 6.5: *** $p<0.0014$

6.5.6.3. Confocal microscopy

Confocal microscopy analysis was carried out on live KB cells previously incubated for 2 hours with the following particle formulations suspended in FFDMEM at pH 7.4 and 6.5:

- *Folate targeted pH responsive gold nanoparticles (FA pH responsive GNPs).*
- *Non Folate targeted pH responsive gold nanoparticles (NON FA pH responsive GNPs).*
- *Folate targeted non pH responsive gold nanoparticles (FA NON pH responsive GNPs).*

As shown in Figure 71. and previously quantified by FACS and Atomic Adsorption Spectroscopy, *Folate targeted pH responsive gold nanoparticles* were selectively and very efficiently taken up by KB cells at pH 6.5 while at pH 7.4 very few fluorescent spots associated to the cells were detectable. *Non Folate targeted pH responsive gold nanoparticles* underwent a very limited internalization confirming the Folate receptor mediated uptake. *Folate targeted non pH responsive gold nanoparticles* likewise

showed a negligible internalization at both pHs since the non-responsiveness of poly(GMA) do not allow the Folate ligand to be exposed and bind the biological folate receptor.

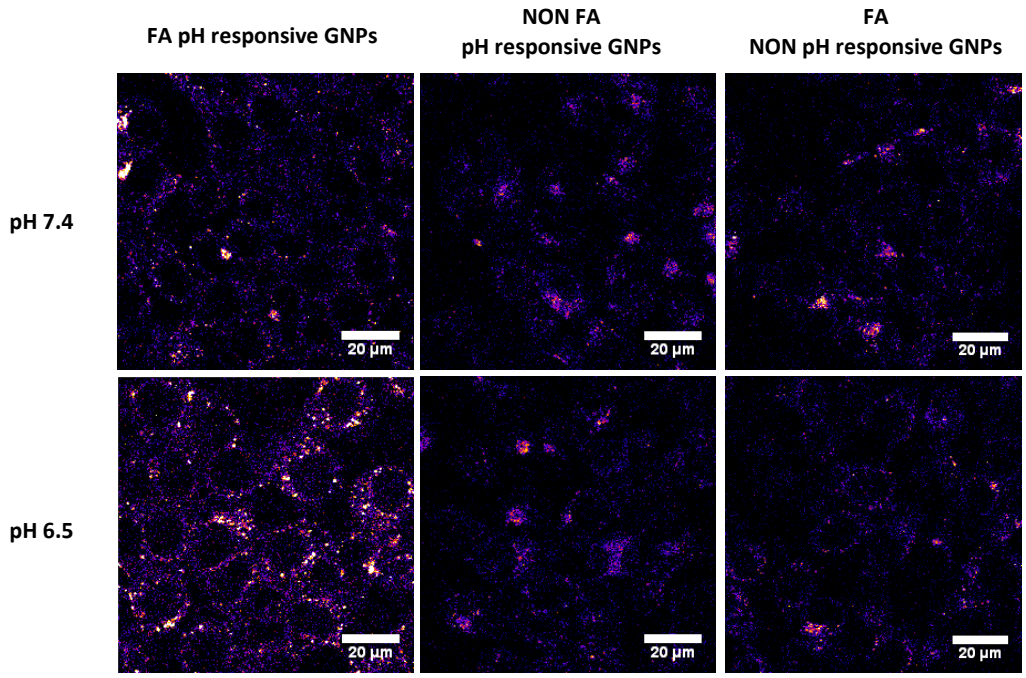

Figure 71. Representative images obtained by confocal microscopy of KB cells incubated Folate targeted pH responsive (FA pH responsive GNPs), NON targeted pH responsive (NON FA pH responsive GNPs) and Folate targeted NON pH responsive (FA NON pH responsive GNPs) gold nanoparticles at pH 7.4 and 6.5. Scale bars of 20 µm.

Competitive assay was performed by incubating the particle samples in the presence of free Folate as competitor for the Folate receptor binding. Representative images in Figure 72. highlight the particle uptake inhibition due to the receptor saturation by the free vitamin, endorsing the hypothesis of the Folate receptor mediated internalization mechanism. The cells incubated with *Folate targeted pH responsive GNPs* in the presence of free folate at pH 6.5 showed a low fluorescence that was comparable to the cells incubated without free folate at pH 7.4. This confirms that the particle uptake is significantly dictated by the mechanism involving the folate receptor biorecognition.

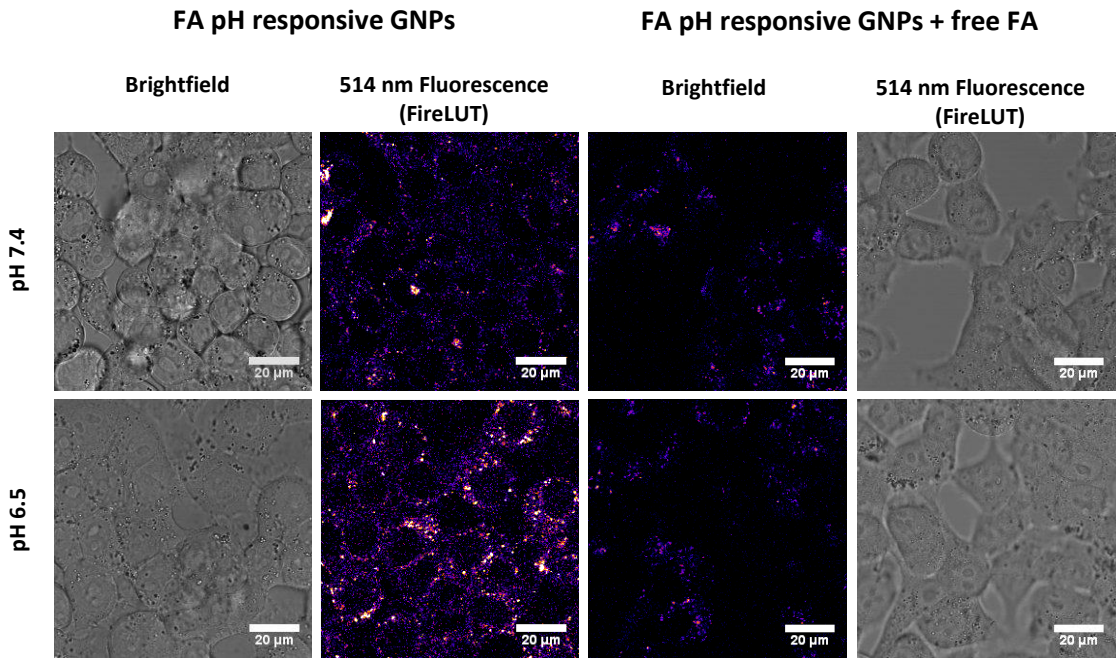

Figure 72. Representative images obtained by confocal microscopy of KB cells incubated with Folate targeted pH responsive GNPs in the presence or not of free Folate as competitive agent. Scale bars of 20 µm.

6.5.6.4. Transmission electron microscopy on KB cells

TEM analysis of KB cells incubated with *Folate targeted pH responsive GNP* suspensions in FFDMEM at pH 7.4 and 6.5 were performed to investigate the intracellular GNP distribution.

At pH 6.5 *Folate targeted pH responsive GNPs* are largely taken up by KB cells as shown in Figure 73. GNPs are present in the cytoplasm and are associated to tubular vesicles whose morphology is compatible with the GPI-anchored protein enriched early endosomal compartments (GEECs). Most of the particles observe intracellularly were entrapped in these subcellular compartments. As described in paragraph 6.4.5, *Folate targeted pH responsive GNPs* may be internalized by a clathrin-independent pathway. More in detail, GEEC is a clathrin- and caveolae-independent endocytosis with ~90 nm vesicles[147], in agreement with the vesicles in Figure 73. On the contrary particles incubated at pH 7.4 showed a negligible internalization and most of the detected particles were found adsorbed on the external cell membrane (Figure 74.). This unspecific adsorption, at least in part, may account for the particles quantified by Atomic adsorption and Flow cytometry analysis at pH 7.4.

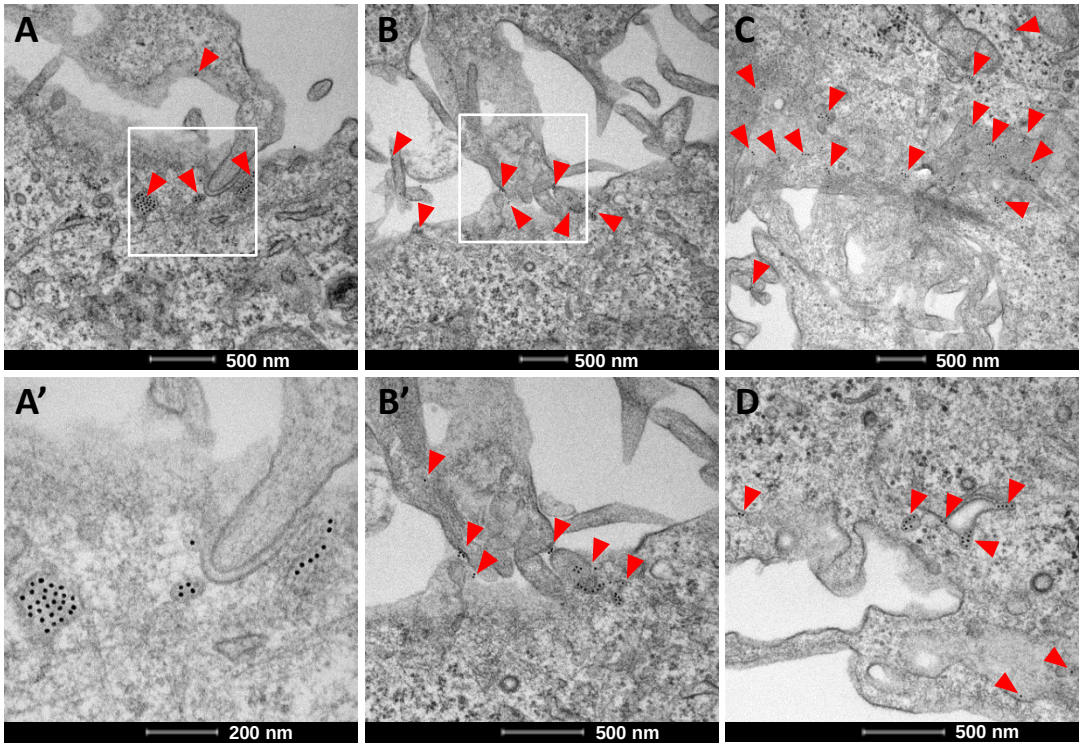

Figure 73. (A, B, C, D) TEM images of Folate targeted pH responsive GNPs incubated with KB cells in FFDMEM at pH 6.5. Red arrows denote the presence of GNPs. Panel A' and B' are magnifications of panel A and B respectively.

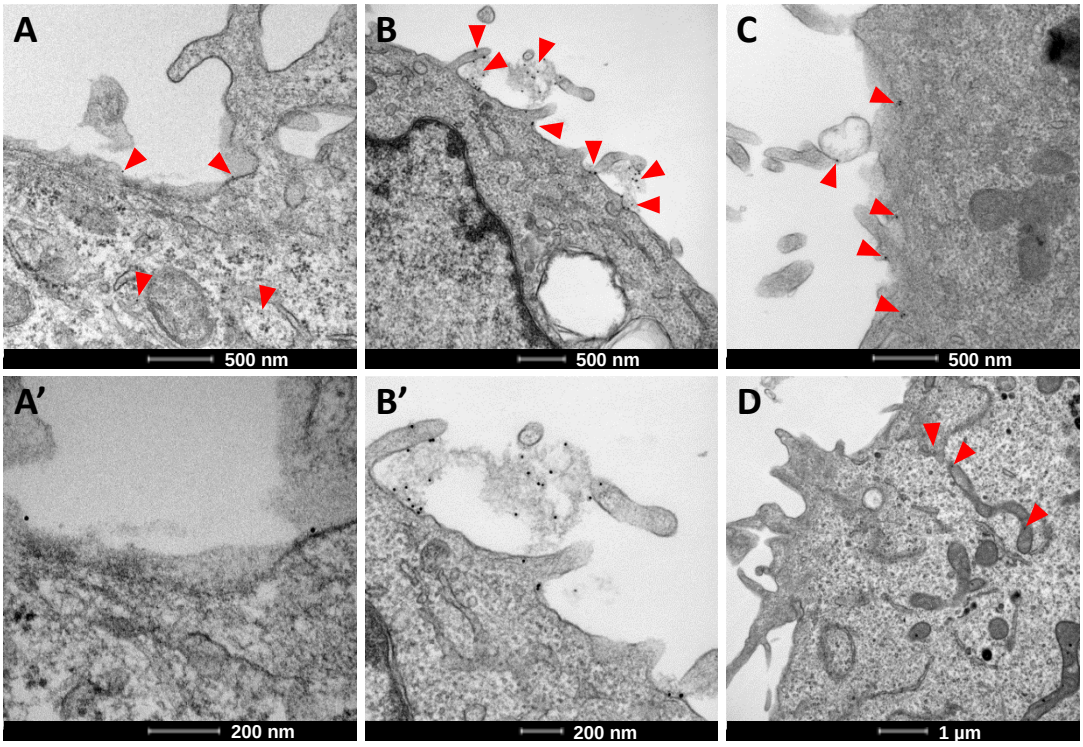

Figure 74. (A, B, C, D) TEM images of Folate targeted pH responsive GNPs incubated with KB cells in FFDMEM at pH 7.4. Red arrows denote the presence of GNPs. Panel A' and B' are magnifications of panel A and B respectively.

7. CONCLUSIONS

Current anticancer drugs suffer from several limitations such as poor solubility, short half-life and uncontrolled distribution throughout the body. This inability to discriminate between malignant and healthy cells limits the accumulation within the target tissue whereby high doses are required to reach a biologically effective concentration, further increasing the severe side effects. In 1906, Paul Ehrlich described the need of a drug able to specifically accumulate in the targeted site postulating the creation of "magic bullets" for use in the fight against human diseases.
In this scenario, gold nanoparticles have emerged because of their tremendous opportunities for the design of next-generation, multimodal anticancer treatment strategies involving photothermal and sonodynamic therapy, drug delivery and gene therapy. Spherical gold nanoparticle can be easily synthetized by Turkevich method: it is a gold chloride citrate-mediated reduction in which citrate also acts as a labile, anionic capping agent which stabilizes the colloid by electrostatic repulsion. The obtained citrated-capped gold nanoparticles possess a narrow polydispersity index and long stability. After synthesis, stabilizing agents can be displaced by other molecules in ligand exchange reactions. Thanks to the high affinity of thiol/disulphide groups for gold surface, most frequently thiol modified ligands are used for the particle decoration involving the formation of Au-S stable bond. Due to their large surface area-to-volume ratio and functional versatility, these particle conjugates can exhibit increased targeting selectivity, augmented binding affinity, long circulatory half-life, high biocompatibility and size-enhanced tumour uptake. The optical and electronic properties of gold nanoparticles can further provide high contrast in photothermal therapeutic treatments, X-ray CT imaging and other non-invasive diagnostic imaging techniques. The intrinsic biomolecular interactions of gold nanoparticles can additionally provide cancer-selective cytotoxic activity. Notably, recent studies highlighted the use of gold nanoparticles as novel nanosensitizers in sonodynamic therapy able to kill cancer cells through the generation of highly reactive products, such as reactive oxygen species (ROS), through apoptotic and/or necrotic mechanism. Efficient and specific delivery of particles to tumour tissue can be accomplished either by passive accumulation through leaky tumour vessels, or by

biological molecule that possesses the appropriate cell-receptor binding functionality. Thus particle surface can be widely decorated with several ligands such as radioactive agents, fluorescent labels and tumour targeting molecules (like antibodies, peptides, nucleic acids etc.).

In the present thesis work a novel gold/organic hybrid nanocarrier with enhanced site-selectivity for anticancer drug delivery was developed. Nanocarrier size was tuned to combine the EPR accumulation of 15 nm gold nanoparticles with an active targeting moiety to selectively deliver and treat solid tumours. Due to its possibility of conjugation, non-immunogenic properties, and requirement for cancer cell growth, Folate was selected as targeting agent for malignant tumours which overexpress the Folate receptor (e.g. osteosarcoma, non-Hodgkin lymphoma, ovarian cancer). Folate was conjugated to the particle surface via a thiol-PEG spacer of proper length to promote the interaction with the specific receptor. Several studies reported in literature celebrate the enhanced internalization efficacy deriving from multi-targeted systems; however, little work has been done to determine whether an optimal ligand density exists. This study widely investigates the effect of surface ligand density on the internalization efficiency of gold nanoparticles and their intracellular trafficking through multiple analysis instrumentations (Atomic adsorption spectroscopy, Flow cytometry and Confocal microscopy). Consistent results obtained by different techniques showed a linear correlation between the number of targeting ligands and the internalization efficiency up to a saturation level reached with 50 chains of Folate-PEG-SH. Thereby 50-fold ratio of Folate-PEG-SH assures the optimum condition for the particle internalization by high Folate receptor expressing KB cells. The specificity of the uptake was proved by several controls: (i) non targeted particles revealed a negligible association with KB cells; (ii) Folate targeted GNPs were not taken up by MCF-7 cells, which is not provided of the Folate receptor on the cell membrane; (iii) cell competition assay showed that the incubation of Folate targeted particles in the presence of free Folate induce the inhibition of GNP uptake. We can conclude that a multivalent network may increase the GNP avidity for FRs.

Moreover detailed trafficking studies of multi-Folate targeted particles with different ligand density and a monovalent ligand were performed. Confocal analysis suggests

that ligand density not only affects the level of cell internalization of targeted nanoparticles, but also influences the pathway of nanoparticle uptake by the cells. Notably a higher Folate density corresponds to a faster and more efficient lysosomal delivery. This can be ascribed to a different internalization route or a different ability to induce the Folate receptor clustering and subsequent delivery to lysosomes. Studies reported in literature revealed that monovalent folate-drug conjugate recycle through endosomes with median pH of 6.8. In contrast, multivalent folate conjugates were found to traffic to lysosomes[148], line with the numerous studies of membrane receptors that traffic to lysosomes when crosslinked[137]. Once established the best Folate density which enables an efficient accumulation at disease sites, other targeting strategies have been examined.

Recently the discoveries concerning the physio-pathology of tumour formation are inspiring the design of tailor-made nanocarriers with features that suit the local environment of this tissue, which may include specific enzyme overexpression, low pH and elevated glucose metabolism. These particular conditions can be exploited either to realize a selective internalization of the carrier modulating its surface properties or to trigger the drug release by degradation of the carrier. The stimulus nature could also be external such as light, temperature or magnetic field. Significantly the internal stimuli operate in a biologically control manner, whereas the external stimuli provide spatio-temporal control over the release[149149149].

The carrier here developed is intended to sense environmental alterations after extravasation from the blood to the tumour and respond with morphological rearrangements that allow for the biorecognition of cancer cells and cell uptake.

In particular, the decoration of gold nanoparticles with a pH responsive polymer with a pKa in the physio-pathological range and the targeting agent Folate-PEG-SH yields a stimuli sensitive nanosystem that can be instructed to operate specific and sequential functions under temporal and spatial control. Folate targeted pH responsive GNPs have been tested in *vitro* with tumour cells overexpressing and non-expressing the Folate receptor. The cell uptake results confirmed that the hiding and reveal of targeting agents on GNPs surface modulated by sensitive polymers guarantees enhanced site-selectivity to cancer cells according to a cooperative exploitation of phenotypic and environmental features of the tumour.

Another great application of gold nanoparticles is their use as sonosensitizers in the sonodynamic therapy (SDT). SDT is a newly developed physical approach for the treatment of cancer where ultrasound triggers by cavitation phenomenon the rapid tumour cell death without damaging the surrounding tissues. In virtue of their unique physicochemical properties, gold nanoparticles can be *per se* considered as therapeutic nanodevices since they can accelerate the cavitation phenomena and so enhance the SDT efficacy. Moreover, the combination of physical approaches to pharmacological treatment can reduce the required dose and the administration frequency of the treatment, limit the side effects and produce a selective and effective cell killing. In light of this, one of the aims of this thesis was the investigation of the *Folate targeted gold nanoparticle* exploitation as enhancer of the efficacy and selectivity of the sonodynamic therapy. KB cancer overexpressing Folate receptor cells showed a significant cell growth decrease after sonodynamic treatment with *Folate targeted GNP* incubation and continuous ultrasound exposure, whereas no cytotoxic effect was induced either by ultrasound or *Folate decorated particles* alone or by the combination of non-targeted particles and ultrasounds. Two additional control experiments lend further support for the uptake of *Folate targeted GNPs* via receptor-mediated endocytosis. MCF-7 cells, which lack the Folate receptor, were incapable of internalizing significant amounts of the Folate-functionalized nanoparticles. When *Folate targeted GNPs* were incubated with KB cells in culture medium augmented with free folate, KB cells did not internalize the GNPs. This result highlighted that the particle uptake is mediated by Folate receptor and the cytotoxic effect is ascribable to the peculiar sonosensitizing effect of endocytosed GNPs as consequence of the ultrasound induced acoustic cavitation. In conclusion, the present project thesis is proposed as proof-of-concept to show that by finely controlling the surface properties of nanosystems, site-selectivity can be significantly enhanced, thus reducing the disposition of drug nanocarriers in off-target tissues. These designed features can be adapted to a variety of colloidal carriers for the development of highly multifunctional platform for the multistrategic treatment of cancer. This platform is aimed for the delivery of anticancer drugs; thus, the carrier will be further developed by including a third component, a polymer bearing doxorubicin molecules conjugated through an endosomal cleavable bond (hydrazone). In such a case the “cocktail” application strategy, as the combination of a pharmacological (doxorubicin) and a

physical treatment (ultrasound) will exponentially increase the therapeutic effect, decrease the multi-drug resistance and improve the clinical outcomes.

8. REFERENCES

1 Davis, M. E. & Shin, D. M. Nanoparticle therapeutics: an emerging treatment modality for cancer. *Nature reviews Drug discovery* **7**, 771-782 (2008).

2 Safra, T. *et al.* Pegylated liposomal doxorubicin (doxil): reduced clinical cardiotoxicity in patients reaching or exceeding cumulative doses of 500 mg/m2. *Ann. Oncol.* **11**, 1029-1033 (2000).

3 Blanco, E., Shen, H. & Ferrari, M. Principles of nanoparticle design for overcoming biological barriers to drug delivery. *Nat. Biotechnol.* **33**, 941-951 (2015).

4 Bareford, L. M. & Swaan, P. W. Endocytic mechanisms for targeted drug delivery. *Advanced drug delivery reviews* **59**, 748-758 (2007).

5 Mukherjee, S., Ghosh, R. N. & Maxfield, F. R. Endocytosis. *Physiol. Rev.* **77**, 759-803 (1997).

6 Carrstensen, H., Mueller, R. H. & Müller, B. Particle size, surface hydrophobicity and interaction with serum of parenteral fat emulsions and model drug carriers as parameters related to RES uptake. *Clin. Nutr.* **11**, 289-297 (1992).

7 Norman, M., Williams, P. & Illum, L. Human serum albumin as a probe for surface conditioning (opsonization) of block copolymer-coated microspheres. *Biomaterials* **13**, 841-849 (1992).

8 Salvati, A. *et al.* Transferrin-functionalized nanoparticles lose their targeting capabilities when a biomolecule corona adsorbs on the surface. *Nature nanotechnology* **8**, 137-143 (2013).

9 Salmaso, S. & Caliceti, P. Stealth Properties to Improve Therapeutic Efficacy of Drug Nanocarriers. *Journal of Drug Delivery* **2013**, 19, doi:10.1155/2013/374252 (2013).

10 Kim, D., Jeong, Y. Y. & Jon, S. A Drug-Loaded Aptamer−Gold Nanoparticle Bioconjugate for Combined CT Imaging and Therapy of Prostate Cancer. *ACS nano* **4**, 3689-3696, doi:10.1021/nn901877h (2010).

11 Zavaleta, C. L. *et al.* Multiplexed imaging of surface enhanced Raman scattering nanotags in living mice using noninvasive Raman spectroscopy. *Proceedings of the National Academy of Sciences* **106**, 13511-13516, doi:10.1073/pnas.0813327106 (2009).

12 Jokerst, J. V. & Gambhir, S. S. Molecular imaging with theranostic nanoparticles. *Accounts of chemical research* **44**, 1050-1060, doi:10.1021/ar200106e (2011).

13 Dreaden, E. C., Austin, L. A., Mackey, M. A. & El-Sayed, M. A. Size matters: gold nanoparticles in targeted cancer drug delivery. *Therapeutic delivery* **3**, 457-478 (2012).

14 Jung, Y., Reif, R., Zeng, Y. & Wang, R. K. Three-Dimensional High-Resolution Imaging of Gold Nanorods Uptake in Sentinel Lymph Nodes. *Nano Letters* **11**, 2938-2943, doi:10.1021/nl2014394 (2011).

15 Huang, X., Jain, P., El-Sayed, I. & El-Sayed, M. Plasmonic photothermal therapy (PPTT) using gold nanoparticles. *Lasers Med Sci* **23**, 217-228, doi:10.1007/s10103-007-0470-x (2008).

16 Rahman, W. N. *et al.* Enhancement of radiation effects by gold nanoparticles for superficial radiation therapy. *Nanomedicine: Nanotechnology, Biology and Medicine* **5**, 136-142 (2009).

17 Tachibana, K., Uchida, T., Ogawa, K., Yamashita, N. & Tamura, K. Induction of cell-membrane porosity by ultrasound. *The Lancet* **353**, 1409, doi:http://dx.doi.org/10.1016/S0140-6736(99)01244-1 (1999).
18 Froimowicz, P., Munoz-Espi, R., Landfester, K., Musyanovych, A. & Crespy, D. Surface-functionalized particles: From their design and synthesis to materials science and bio-applications. *Current Organic Chemistry* **17**, 900-912 (2013).
19 Ferlay, J. *et al.* GLOBOCAN 2008, Cancer incidence and mortality worldwide: IARC CancerBase No. 10. *Lyon, France: International Agency for Research on Cancer* **2010**, 29 (2010).
20 Nigg, E. A. Cyclin-dependent protein kinases: key regulators of the eukaryotic cell cycle. *Bioessays* **17**, 471-480 (1995).
21 Hoeijmakers, J. H. Genome maintenance mechanisms for preventing cancer. *nature* **411**, 366-374 (2001).
22 Hanahan, D. & Weinberg, R. A. Hallmarks of cancer: the next generation. *Cell* **144**, 646-674 (2011).
23 Chidambaram, M., Manavalan, R. & Kathiresan, K. Nanotherapeutics to overcome conventional cancer chemotherapy limitations. *Journal of Pharmacy & Pharmaceutical Sciences* **14**, 67-77 (2011).
24 Riddick, D. S. *et al.* Cancer chemotherapy and drug metabolism. *Drug Metabolism and Disposition* **33**, 1083-1096 (2005).
25 Berardi, R. *et al.* State of the art for cardiotoxicity due to chemotherapy and to targeted therapies: a literature review. *Crit. Rev. Oncol. Hematol.* **88**, 75-86 (2013).
26 Institute, N. C. in *NCI website* (December 4, 2014).
27 Costley, D. *et al.* Treating cancer with sonodynamic therapy: A review. *Int. J. Hyperthermia* **31**, 107-117 (2015).
28 Wang, H. *et al.* Microbubbles Enhance the Antitumor Effects of Sinoporphyrin Sodium Mediated Sonodynamic Therapy both In Vitro and In Vivo. *International journal of biological sciences* **11**, 1401 (2015).
29 Serpe, L., Foglietta, F. & Canaparo, R. Nanosonotechnology: the next challenge in cancer sonodynamic therapy. *Nanotechnology Reviews* **1**, doi:citeulike-article-id:11688800
doi: 10.1515/ntrev-2011-0009 (2012).
30 Tsai, M.-J., Chang, W.-A., Huang, M.-S. & Kuo, P.-L. Tumor Microenvironment: A New Treatment Target for Cancer. *ISRN Biochemistry* **2014**, 8, doi:10.1155/2014/351959 (2014).
31 Paget, S. The distribution of secondary growths in cancer of the breast. *The Lancet* **133**, 571-573 (1889).
32 Vaupel, P., Kallinowski, F. & Okunieff, P. Blood flow, oxygen and nutrient supply, and metabolic microenvironment of human tumors: a review. *Cancer Res.* **49**, 6449-6465 (1989).
33 Brown, N. S. & Bicknell, R. Hypoxia and oxidative stress in breast cancer. Oxidative stress: its effects on the growth, metastatic potential and response to therapy of breast cancer. *Breast cancer research : BCR* **3**, 323-327 (2001).
34 Gray, L. H., Conger, A. D., Ebert, M., Hornsey, S. & Scott, O. The concentration of oxygen dissolved in tissues at the time of irradiation as a factor in radiotherapy. *The British journal of radiology* **26**, 638-648 (1953).
35 Warburg, O. The metabolism of tumors (English translation by F. Dickens). *Constable, London* (1930).
36 Kato, Y. *et al.* Acidic extracellular microenvironment and cancer. *Cancer Cell International* **13**, 89-89, doi:10.1186/1475-2867-13-89 (2013).

37 Yabu, M. *et al.* IL-23-dependent and -independent enhancement pathways of IL-17A production by lactic acid. *Int. Immunol.* **23**, 29-41, doi:10.1093/intimm/dxq455 (2011).

38 Vogelstein, B. & Kinzler, K. W. Cancer genes and the pathways they control. *Nat. Med.* **10**, 789-799 (2004).

39 van Sluis, R. *et al.* In vivo imaging of extracellular pH using 1 H MRSI. *Magn. Reson. Med.* **41**, 743-750 (1999).

40 Griffiths, J. Are cancer cells acidic? *Br. J. Cancer* **64**, 425 (1991).

41 Bergers, G. & Benjamin, L. E. Tumorigenesis and the angiogenic switch. *Nature reviews cancer* **3**, 401-410 (2003).

42 Gazit, Y. *et al.* Fractal characteristics of tumor vascular architecture during tumor growth and regression. *Microcirculation* **4**, 395-402 (1997).

43 Dameron, K. M., Volpert, O. V., Tainsky, M. A. & Bouck, N. Control of angiogenesis in fibroblasts by p53 regulation of thrombospondin-1. *SCIENCE-NEW YORK THEN WASHINGTON-*, 1582-1582 (1994).

44 Nishida, N., Yano, H., Nishida, T., Kamura, T. & Kojiro, M. Angiogenesis in cancer. *Vascular health and risk management* **2**, 213 (2006).

45 Allen, T. M. & Cullis, P. R. Drug delivery systems: entering the mainstream. *Science* **303**, 1818-1822 (2004).

46 Jain, R. K. Normalization of tumor vasculature: an emerging concept in antiangiogenic therapy. *Science* **307**, 58-62 (2005).

47 Matsumura, Y. & Maeda, H. A New Concept for Macromolecular Therapeutics in Cancer Chemotherapy: Mechanism of Tumoritropic Accumulation of Proteins and the Antitumor Agent Smancs. *Cancer Res.* **46**, 6387-6392 (1986).

48 Toporkiewicz, M., Meissner, J., Matusewicz, L., Czogalla, A. & Sikorski, A. F. Toward a magic or imaginary bullet? Ligands for drug targeting to cancer cells: principles, hopes, and challenges. *International journal of nanomedicine* **10**, 1399 (2015).

49 Sundaresan, M. *et al.* Regulation of reactive-oxygen-species generation in fibroblasts by Rac1. *Biochem. j* **318**, 379-382 (1996).

50 Khandrika, L., Kumar, B., Koul, S., Maroni, P. & Koul, H. K. Oxidative stress in prostate cancer. *Cancer Lett.* **282**, 125-136 (2009).

51 Kola, I. & Landis, J. Can the pharmaceutical industry reduce attrition rates? *Nature reviews Drug discovery* **3**, 711-716 (2004).

52 Desai, N. Challenges in Development of Nanoparticle-Based Therapeutics. *The AAPS Journal* **14**, 282-295, doi:10.1208/s12248-012-9339-4 (2012).

53 Brinkhuis, R. P., Rutjes, F. P. & van Hest, J. C. Polymeric vesicles in biomedical applications. *Polymer Chemistry* **2**, 1449-1462 (2011).

54 Hauert, S. & Bhatia, S. N. Mechanisms of cooperation in cancer nanomedicine: towards systems nanotechnology. *Trends Biotechnol.* **32**, 448-455 (2014).

55 Qi, W., Ghoroghchian, P. P., Li, G., Hammer, D. A. & Therien, M. J. Aqueous self-assembly of poly (ethylene oxide)-block-poly (ε-caprolactone)(PEO-b-PCL) copolymers: disparate diblock copolymer compositions give rise to nano-and meso-scale bilayered vesicles. *Nanoscale* **5**, 10908-10915 (2013).

56 Gentile, F. *et al.* The effect of shape on the margination dynamics of non-neutrally buoyant particles in two-dimensional shear flows. *J. Biomech.* **41**, 2312-2318, doi:http://dx.doi.org/10.1016/j.jbiomech.2008.03.021 (2008).

57 Christian, D. A. *et al.* Flexible filaments for in vivo imaging and delivery: persistent circulation of filomicelles opens the dosage window for sustained tumor shrinkage. *Molecular pharmaceutics* **6**, 1343-1352 (2009).

58 Nel, A. E. *et al.* Understanding biophysicochemical interactions at the nano-bio interface. *Nat Mater* **8**, 543-557 (2009).

59 Minko, T., Rodriguez-Rodriguez, L. & Pozharov, V. Nanotechnology approaches for personalized treatment of multidrug resistant cancers. *Advanced drug delivery reviews* **65**, 1880-1895 (2013).

60 Allen, T. M. Ligand-targeted therapeutics in anticancer therapy. *Nature Reviews Cancer* **2**, 750-763 (2002).

61 Bae, Y. H. & Park, K. Targeted drug delivery to tumors: myths, reality and possibility. *J. Controlled Release* **153**, 198 (2011).

62 Darrell, J. One nanoparticle, one kill. *Nature Materials* **10**, 342-343 (2011).

63 Onaca, O., Enea, R., Hughes, D. W. & Meier, W. Stimuli-Responsive Polymersomes as Nanocarriers for Drug and Gene Delivery. *Macromolecular bioscience* **9**, 129-139 (2009).

64 Pearson, R. T., Warren, N. J., Lewis, A. L., Armes, S. P. & Battaglia, G. Effect of pH and temperature on PMPC–PDPA copolymer self-assembly. *Macromolecules* **46**, 1400-1407 (2013).

65 Li, Y. *et al.* Well-defined, reversible disulfide cross-linked micelles for on-demand paclitaxel delivery. *Biomaterials* **32**, 6633-6645 (2011).

66 Haucke, V. Cell biology: On the endocytosis rollercoaster. *Nature* **517**, 446-447, doi:10.1038/nature14081 (2015).

67 Besterman, J. M. & Low, R. B. Endocytosis: a review of mechanisms and plasma membrane dynamics. *Biochem. J.* **210**, 1-13 (1983).

68 Conner, S. D. & Schmid, S. L. Regulated portals of entry into the cell. *Nature* **422**, 37-44 (2003).

69 Le Roy, C. & Wrana, J. L. Clathrin-and non-clathrin-mediated endocytic regulation of cell signalling. *Nature reviews Molecular cell biology* **6**, 112-126 (2005).

70 Xu, S., Olenyuk, B. Z., Okamoto, C. T. & Hamm-Alvarez, S. F. Targeting receptor-mediated endocytotic pathways with nanoparticles: rationale and advances. *Advanced drug delivery reviews* **65**, 121-138 (2013).

71 Schmid, E. M. & McMahon, H. T. Integrating molecular and network biology to decode endocytosis. *Nature* **448**, 883-888, doi:http://www.nature.com/nature/journal/v448/n7156/suppinfo/nature06031_S1.html (2007).

72 Hillaireau, H. & Couvreur, P. Nanocarriers' entry into the cell: relevance to drug delivery. *Cell. Mol. Life Sci.* **66**, 2873-2896 (2009).

73 Doherty, G. J. & McMahon, H. T. Mechanisms of Endocytosis. *Annu. Rev. Biochem.* **78**, 857-902, doi:doi:10.1146/annurev.biochem.78.081307.110540 (2009).

74 Chen, C. *et al.* Structural basis for molecular recognition of folic acid by folate receptors. *Nature* **500**, 486-489 (2013).

75 Sabharanjak, S. & Mayor, S. Folate receptor endocytosis and trafficking. *Advanced Drug Delivery Reviews* **56**, 1099-1109 (2004).

76 Theti, D. S. & Jackman, A. L. The role of α-folate receptor-mediated transport in the antitumor activity of antifolate drugs. *Clin. Cancer Res.* **10**, 1080-1089 (2004).

77 Gabizon, A. *et al.* Targeting folate receptor with folate linked to extremities of poly (ethylene glycol)-grafted liposomes: in vitro studies. *Bioconjug. Chem.* **10**, 289-298 (1999).

78 Mayor, S., Rothberg, K. G. & Maxfield, F. R. Sequestration of GPI-anchored proteins in caveolae triggered by cross-linking. *Science* **264**, 1948-1951 (1994).

79 Parton, R. G., Joggerst, B. & Simons, K. Regulated internalization of caveolae. *The Journal of cell biology* **127**, 1199-1215 (1994).

80 Skretting, G., Torgersen, M. L., van Deurs, B. & Sandvig, K. Endocytic mechanisms responsible for uptake of GPI-linked diphtheria toxin receptor. *J. Cell Sci.* **112**, 3899-3909 (1999).

81 Fivaz, M. *et al.* Differential sorting and fate of endocytosed GPI-anchored proteins. *The EMBO journal* **21**, 3989-4000 (2002).

82 Zhao, R. *et al.* A role for the proton-coupled folate transporter (PCFT-SLC46A1) in folate receptor-mediated endocytosis. *J. Biol. Chem.* **284**, 4267-4274 (2009).

83 Bandara, N. A., Hansen, M. J. & Low, P. S. Effect of receptor occupancy on folate receptor internalization. *Molecular pharmaceutics* **11**, 1007-1013 (2014).

84 Mansoori, G. A., Brandenburg, K. S. & Shakeri-Zadeh, A. A comparative study of two folate-conjugated gold nanoparticles for cancer nanotechnology applications. *Cancers* **2**, 1911-1928 (2010).

85 Hong, S. *et al.* The binding avidity of a nanoparticle-based multivalent targeted drug delivery platform. *Chem. Biol.* **14**, 107-115 (2007).

86 Elias, D. R., Poloukhtine, A., Popik, V. & Tsourkas, A. Effect of ligand density, receptor density, and nanoparticle size on cell targeting. *Nanomedicine: Nanotechnology, Biology and Medicine* **9**, 194-201 (2013).

87 Smart, E. J., Mineo, C. & Anderson, R. Clustered folate receptors deliver 5-methyltetrahydrofolate to cytoplasm of MA104 cells. *The Journal of cell biology* **134**, 1169-1177 (1996).

88 Cluzel, C. *et al.* The mechanisms and dynamics of αvβ3 integrin clustering in living cells. *The Journal of cell biology* **171**, 383-392 (2005).

89 Liu, A. P., Aguet, F., Danuser, G. & Schmid, S. L. Local clustering of transferrin receptors promotes clathrin-coated pit initiation. *The Journal of cell biology* **191**, 1381-1393 (2010).

90 Mura, S., Nicolas, J. & Couvreur, P. Stimuli-responsive nanocarriers for drug delivery. *Nature materials* **12**, 991-1003 (2013).

91 Daniel, M.-C. & Astruc, D. Gold nanoparticles: assembly, supramolecular chemistry, quantum-size-related properties, and applications toward biology, catalysis, and nanotechnology. *Chem. Rev.* **104**, 293-346 (2004).

92 Frens, G. Controlled nucleation for the regulation of the particle size in monodisperse gold suspensions. *Nature* **241**, 20-22 (1973).

93 Turkevich, J., Stevenson, P. C. & Hillier, J. A study of the nucleation and growth processes in the synthesis of colloidal gold. *Discuss. Faraday Soc.* **11**, 55-75, doi:10.1039/DF9511100055 (1951).

94 Turkevich, J., Stevenson, P. C. & Hillier, J. The Formation of Colloidal Gold. *The Journal of Physical Chemistry* **57**, 670-673, doi:10.1021/j150508a015 (1953).

95 Brust, M., Walker, M., Bethell, D., Schiffrin, D. J. & Whyman, R. Synthesis of thiol-derivatised gold nanoparticles in a two-phase liquid–liquid system. *J. Chem. Soc., Chem. Commun.*, 801-802 (1994).

96 Yeh, Y.-C., Creran, B. & Rotello, V. M. Gold nanoparticles: preparation, properties, and applications in bionanotechnology. *Nanoscale* **4**, 1871-1880 (2012).

97 Connor, E. E., Mwamuka, J., Gole, A., Murphy, C. J. & Wyatt, M. D. Gold nanoparticles are taken up by human cells but do not cause acute cytotoxicity. *Small (Weinheim an der Bergstrasse, Germany)* **1**, 325-327 (2005).

98 Moad, G., Chong, Y., Postma, A., Rizzardo, E. & Thang, S. H. Advances in RAFT polymerization: the synthesis of polymers with defined end-groups. *Polymer* **46**, 8458-8468 (2005).

99 Gole, A. & Murphy, C. J. Seed-mediated synthesis of gold nanorods: role of the size and nature of the seed. *Chemistry of Materials* **16**, 3633-3640 (2004).

100 Coffer, J. L., Shapley, J. R. & Drickamer, H. G. The effect of pressure on the surface plasmon absorption spectra of colloidal gold and silver particles. *J. Am. Chem. Soc.* **112**, 3736-3742 (1990).

101 Pillai, G. Nanomedicines for cancer therapy: An update of FDA approved and those under various stages development. *SOJ Pharm. Pharm. Sci* **1**, 1-13 (2014).

102 Sperling, R. A., Gil, P. R., Zhang, F., Zanella, M. & Parak, W. J. Biological applications of gold nanoparticles. *Chemical Society Reviews* **37**, 1896-1908 (2008).

103 Dorsey, J. F. *et al.* Gold nanoparticles in radiation research: potential applications for imaging and radiosensitization. *Translational Cancer Research* **2**, 280-291 (2013).

104 Perrone, B., Springhetti, S., Ramadori, F., Rastrelli, F. & Mancin, F. "NMR Chemosensing" using monolayer-protected nanoparticles as receptors. *J. Am. Chem. Soc.* **135**, 11768-11771 (2013).

105 Murphy, C. J. *et al.* Gold nanoparticles in biology: beyond toxicity to cellular imaging. *Accounts of chemical research* **41**, 1721-1730 (2008).

106 Das, M., Shim, K. H., An, S. S. A. & Yi, D. K. Review on gold nanoparticles and their applications. *Toxicology and Environmental Health Sciences* **3**, 193-205 (2011).

107 Pernodet, N. *et al.* Adverse effects of citrate/gold nanoparticles on human dermal fibroblasts. *Small (Weinheim an der Bergstrasse, Germany)* **2**, 766-773 (2006).

108 Moad, G., Rizzardo, E. & Thang, S. H. Radical addition–fragmentation chemistry in polymer synthesis. *Polymer* **49**, 1079-1131 (2008).

109 Sims, G. E. C. & Snape, T. J. A method for the estimation of polyethylene glycol in plasma protein fractions. *Anal. Biochem.* **107**, 60-63, doi:http://dx.doi.org/10.1016/0003-2697(80)90492-3 (1980).

110 Ellman, G. L. Tissue sulfhydryl groups. *Arch. Biochem. Biophys.* **82**, 70-77, doi:http://dx.doi.org/10.1016/0003-9861(59)90090-6 (1959).

111 Riddles, P. W., Blakeley, R. L. & Zerner, B. Ellman's reagent: 5,5′-dithiobis(2-nitrobenzoic acid)—a reexamination. *Anal. Biochem.* **94**, 75-81, doi:http://dx.doi.org/10.1016/0003-2697(79)90792-9 (1979).

112 Smith, P. *et al.* Measurement of protein using bicinchoninic acid. *Anal. Biochem.* **150**, 76-85 (1985).

113 Banks, J. T., Button, K. M., Gossage, R. A., Hamilton, T. D. & Kershaw, K. E. Synthesis of novel oxazoline ligands designed for attachment to gold nanoparticles. *Heterocycles* **55**, 2251 - 2256 (2001).

114 Su, Z. *et al.* A nitroenolate approach to the synthesis of 4,5-disubstituted-2-aminoimidazoles. Pilot library assembly and screening for antibiotic and antibiofilm activity. *Organic & biomolecular chemistry* **8**, 2814-2822, doi:10.1039/C001479F (2010).

115 Wagner, A. F. *et al.* Properties and derivatives of α-lipoic acid. *J. Am. Chem. Soc.* **78**, 5079-5081 (1956).

116 Mastrotto, F. *et al.* pH-responsive poly (4-hydroxybenzoyl methacrylates)–design and engineering of intelligent drug delivery nanovectors. *Polymer Chemistry* **4**, 4375-4385 (2013).

117 Perrier, S., Takolpuckdee, P. & Mars, C. A. Reversible addition-fragmentation chain transfer polymerization: End group modification for functionalized polymers and chain transfer agent recovery. *Macromolecules* **38**, 2033-2036 (2005).

118 Liu, X., Atwater, M., Wang, J. & Huo, Q. Extinction coefficient of gold nanoparticles with different sizes and different capping ligands. *Colloids and*

Surfaces B: Biointerfaces **58**, 3-7, doi:http://dx.doi.org/10.1016/j.colsurfb.2006.08.005 (2007).

119 Jain, P. K., Lee, K. S., El-Sayed, I. H. & El-Sayed, M. A. Calculated Absorption and Scattering Properties of Gold Nanoparticles of Different Size, Shape, and Composition: Applications in Biological Imaging and Biomedicine. *The Journal of Physical Chemistry B* **110**, 7238-7248, doi:10.1021/jp057170o (2006).

120 Link, S. & El-Sayed, M. A. Spectral Properties and Relaxation Dynamics of Surface Plasmon Electronic Oscillations in Gold and Silver Nanodots and Nanorods. *The Journal of Physical Chemistry B* **103**, 8410-8426, doi:10.1021/jp9917648 (1999).

121 Stiti, M., Bouzit, H., Abdaoui, M. & Winum, J. in *IOP Conference Series: Materials Science and Engineering.* 012032 (IOP Publishing).

122 Liu, X., Yang, J., Zhang, L., Liu, H. & Lu, Y. Self-assembled monolayer of lipoic acid on gold and its application to rapid determination of 2, 3, 7, 8-tetrachlorodibenzo-p-dioxin. *Transactions of Tianjin University* **19**, 248-254 (2013).

123 Dixit, V., Van den Bossche, J., Sherman, D. M., Thompson, D. H. & Andres, R. P. Synthesis and grafting of thioctic acid-PEG-folate conjugates onto Au nanoparticles for selective targeting of folate receptor-positive tumor cells. *Bioconjug. Chem.* **17**, 603-609 (2006).

124 Olszewski-Ortar, A., Gros, P. & Fort, Y. Selective ring-opening of ω-epoxyalkyl (meth) acrylates. An efficient access to bifunctional monomers. *Tetrahedron Lett.* **38**, 8699-8702 (1997).

125 Willcock, H. & O'Reilly, R. K. End group removal and modification of RAFT polymers. *Polymer Chemistry* **1**, 149-157 (2010).

126 Matini, T. *et al.* Synthesis and characterization of variable conformation pH responsive block co-polymers for nucleic acid delivery and targeted cell entry. *Polymer Chemistry* **5**, 1626-1636, doi:10.1039/C3PY00744H (2014).

127 Zhang, K. *et al.* Folate-mediated Cell Uptake of Shell-crosslinked Spheres and Cylinders. *Journal of polymer science. Part A, Polymer chemistry* **46**, 7578-7583, doi:10.1002/pola.23020 (2008).

128 Wang, S., Lee, R. J., Mathias, C. J., Green, M. A. & Low, P. S. Synthesis, purification, and tumor cell uptake of 67Ga-deferoxamine-folate, a potential radiopharmaceutical for tumor imaging. *Bioconjug. Chem.* **7**, 56-62 (1996).

129 Tuziuti, T., Yasui, K., Sivakumar, M., Iida, Y. & Miyoshi, N. Correlation between acoustic cavitation noise and yield enhancement of sonochemical reaction by particle addition. *The Journal of Physical Chemistry A* **109**, 4869-4872 (2005).

130 Shanei, A. *et al.* Sonodynamic Therapy Using Protoporphyrin IX Conjugated to Gold Nanoparticles: An In Vivo Study on a Colon Tumor Model. *Iranian Journal of Basic Medical Sciences* **15**, 759-767 (2012).

131 Salmaso, S. & Caliceti, P. Stealth properties to improve therapeutic efficacy of drug nanocarriers. *Journal of drug delivery* **2013** (2013).

132 Gallon, E. *et al.* Triblock Copolymer Nanovesicles for pH-Responsive Targeted Delivery and Controlled Release of siRNA to Cancer Cells. *Biomacromolecules* **16**, 1924-1937, doi:10.1021/acs.biomac.5b00286 (2015).

133 Moradi, E., Vllasaliu, D., Garnett, M., Falcone, F. & Stolnik, S. Ligand density and clustering effects on endocytosis of folate modified nanoparticles. *RSC Advances* **2**, 3025-3033 (2012).

134 Della-Longa, S. & Arcovito, A. Intermediate states in the binding process of folic acid to folate receptor α: insights by molecular dynamics and metadynamics. *J. Comput. Aided Mol. Des.* **29**, 23-35, doi:10.1007/s10822-014-9801-8 (2015).

135 Wang, Q., Villeneuve, G. & Wang, Z. Control of epidermal growth factor receptor endocytosis by receptor dimerization, rather than receptor kinase activation. *EMBO reports* **6**, 942-948 (2005).

136 Pierre, C. A. S., Leonard, D., Corvera, S., Kurt-Jones, E. A. & Finberg, R. W. Antibodies to cell surface proteins redirect intracellular trafficking pathways. *Exp. Mol. Pathol.* **91**, 723-732 (2011).

137 Moody, P. R. *et al.* Receptor Crosslinking: A General Method to Trigger Internalization and Lysosomal Targeting of Therapeutic Receptor: Ligand Complexes. *Molecular Therapy* (2015).

138 Humphries, W. H., Szymanski, C. J. & Payne, C. K. Endo-lysosomal vesicles positive for Rab7 and LAMP1 are terminal vesicles for the transport of dextran. *PloS one* **6**, e26626-e26626 (2011).

139 Zhai, G. *et al.* A transferrin receptor-targeted liposomal formulation for docetaxel. *Journal of nanoscience and nanotechnology* **10**, 5129-5136 (2010).

140 Anderson, R. G. Potocytosis of small molecules and ions by caveolae. *Trends Cell Biol.* **3**, 69-72 (1993).

141 Xia, X. *et al.* Quantifying the coverage density of poly (ethylene glycol) chains on the surface of gold nanostructures. *ACS nano* **6**, 512-522 (2011).

142 Hinterwirth, H. *et al.* Quantifying thiol ligand density of self-assembled monolayers on gold nanoparticles by inductively coupled plasma–mass spectrometry. *ACS nano* **7**, 1129-1136 (2013).

143 Schneider, G. *et al.* Distance-Dependent Fluorescence Quenching on Gold Nanoparticles Ensheathed with Layer-by-Layer Assembled Polyelectrolytes. *Nano Letters* **6**, 530-536, doi:10.1021/nl052441s (2006).

144 Kang, K. A., Wang, J., Jasinski, J. B. & Achilefu, S. Fluorescence manipulation by gold nanoparticles: from complete quenching to extensive enhancement. *J. Nanobiotechnol* **9**, 16 (2011).

145 Kanaras, A. G., Kamounah, F. S., Schaumburg, K., Kiely, C. J. & Brust, M. Thioalkylated tetraethylene glycol: a new ligand for water soluble monolayer protected gold clusters. *Chemical communications*, 2294-2295, doi:10.1039/B207838B (2002).

146 Chuang, M.-K., Chen, F.-C. & Hsu, C.-S. Gold Nanoparticle-Graphene Oxide Nanocomposites That Enhance the Device Performance of Polymer Solar Cells. *Journal of Nanomaterials* **2014**, 12, doi:10.1155/2014/736879 (2014).

147 Sahay, G., Alakhova, D. Y. & Kabanov, A. V. Endocytosis of Nanomedicines. *Journal of controlled release : official journal of the Controlled Release Society* **145**, 182-195, doi:10.1016/j.jconrel.2010.01.036 (2010).

148 Xia, W. & Low, P. S. Folate-targeted therapies for cancer. *J. Med. Chem.* **53**, 6811-6824 (2010).

149 Ghosh, P., Han, G., De, M., Kim, C. K. & Rotello, V. M. Gold nanoparticles in delivery applications. *Advanced drug delivery reviews* **60**, 1307-1315 (2008).